NANOBIOMEDICAL CENTRE
ADAM MICKIEWICZ UNIVERSITY
POZNAŃ

Development and application of fluorescent microsensors for new label-free detection method based on Low-Q Whispering Gallery Modes

Mateusz Olszyna

Promotor: Prof. dr hab. Stefan Jurga († 15.03.2022)
                Dr. hab. Maciej Wiesner, Prof. UAM
Co-promotor: Dr. hab. Lars Dähne

Doctoral thesis

Acknowledgment

First, I would like to thank my boss and co-promoter Dr. Lars Dähne for giving me the opportunity to work on my PhD thesis in Surflay Nanotec GmbH as well as for his help, useful advice and outstanding supervision in the experiments and stimulating discussions on our experimental results. Thank you for your patience in explaining concepts and for all the great ideas and contributions to the project.

At the same time, I sincerely thank my supervisor Prof. Stefan Jurga for giving me the possibility to carry out my doctoral thesis in the NanoBioMedical Centre, his kind support and engagement on my promotion. Rest in peace.

I would like to thank my second supervisor, Dr. hab, Maciej Wiesner, Prof. UAM for his openness and help on my promotion and defense.

I would most like to thank Dr. Michael Himmelhaus for interesting scientific discussions about Whispering Gallery Modes, all suggestions, and corrections as well as for positive attitude and enthusiasm toward science.

Many thanks to all my colleagues in Surflay GmbH for the friendly atmosphere and enjoyable working environment. Especially I would like to thank Dr. Claudia Aldenhoven, Dr. Aline Debrassi-Smaczniak, Dr. Kerstin Zimmerman and Dr. Cagri Üzüm for their help, advice, scientific and general support.

Many thanks to Dr. Gabriella Egri, Mr. Christian Funk, Mr. Götz Dähne and Mrs. Barbara Baude for always being so helpful and patient as well as for preparing many things that I needed for my experiments.

Finally, my deepest gratitude goes to my parents and wife Julia for their love, continuous support during the last years, motivation and that you always believed in me.

Table of contents

List of Abbreviations

AFM	Atomic Force Microscopy
Biotin-AB	biotin labelled antibody
Biotin-BSA	biotin labelled bovine serum albumin
Biotin-Casein	biotin labelled casein
Biotin-Fibrinogen	biotin labelled fibrinogen
Biotin-NHS	biotin N-hydroxysuccinimide ester
Biotin-PMAA	biotin labelled poly(methacrylic acid)
Biotin-PAH	biotin labelled poly(allylamine hydrochloride)
BLI	Biolayer interferometry
Boc-EDA	N-Boc-ethylenediamine
BS	borosilicate glass
BSA	bovine serum albumin
CCD	charge coupled device
CDI	1,1'-Carbonyldiimidazole
CLSM	Confocal Laser Scanning Microscopy
Coum343	coumarin 343
Coum6	coumarin 6
Coum-PAH	coumarin 343 labelled poly(allylamine hydrochloride)
Coum-PEI	coumarin 343 labelled poly(ethyleneimine)
Coum-PVA	coumarin 343 labelled poly(vinylamine)
DCC	N,N'-dicyclohexylcarbodiimide
DCM	dichloromethane
DME	1,2-dimethoxyethane
DMF	N,N-Dimethylformamid
DMSO	dimethylsulfoxid
EDAC	1-(3idimathylaminopropyl)-3-ethylcarbodiimide hydrochloride
EDTA	ethylenediamine tetraacetic acid disodium salt
FWHM	Full Width at Half Maximum
HABA	4'-hydroxyazobenzene-2-carboxylic acid
HEPES	4-(2-hydroxyethyl) piperazine-1-ethanesulphonic acid
HOMs	Higher Order Modes
LbL	Layer-by-Layer

MF	melamine formaldehyde
NHS	N-hydroxysuccinimide ester
PAH	poly(allylamine hydrochloride)
PDADMAC	poly(diallyldimethylammonium chloride)
PEI	poly(ethyleneimine)
PMAA	poly(methacrylic acid)
PMMA	poly(methyl methacrylate)
PMT	photomultiplier tube
PS	polystyrene
PSS	sodium poly(styrenesulfonate)
PSS-co-maleic acid	poly(4-styreneulfonate)-co-maleic acid sodium salt
PSS-co-PS	poly(styrenesulfonate)-co-polystyrene
PVP	poly(vinylpyrrolidone)
Rho	rhodamine B
Rho-PAH	rhodamine B labelled poly(allylamine hydrochloride)
RIfS	Reflectometric Interference Spectroscopy
ROI	region of interest
SDS	sodium dodecyl sulfate
SiO_2	silica
SPR	Surface Plasmon Resonance
TCDI	1,1'-Thiocarbonyldiimidazole
TE	transversal electric mode
TFA	trifluoroacetic acid
THF	tetrahydrofuran
TIR	Total Internal Reflection
TM	transversal magnetic mode
WGM	Whispering Gallery Mode
QCM	Quartz Crystal Microbalance
Q-Factor	Quality Factor
UV/Vis	ultraviolet/visible

Abstract

Fluorescent spherical microcavities that confine the emission light in low-Q Whispering Gallery Modes (WGMs) resonance can be used as the next-generation of miniaturized label-free biosensors. Integration of WGM sensors with a suitable microfluidic cell array and high-resolved optical components allowed to multiplexed detection of different biomolecules in real-time.

The aim of this work was to develop and characterize fluorescent low-Q WGM resonators which were exploited in label-free bioanalysis. Six key aspects in the fabrication of low-Q WGM microparticles and their impact on the signal quality and sensing performance were studied: the resonator material type, the polymerization method, the resonator size, the fluorescent dye, the dye distribution and the surface functionalization.

The investigation of different particle materials showed that the best spectra characterized by high intensity and narrow peaks bandwidth can be obtained for PS particles. The most crucial parameters of WGM microsensors determining the quality of resonance are found to be the refractive index and the surface roughness. The best-suited polymerization method to fabrication of polystyrene low-Q WGM sensors was seeded-growth polymerization because of high WGM performances, monodispersity, and easy control of particle size. Setting the acceptable upper limit of peak bandwidth to 0.1 nm, the minimal diameter of PS particles should be above 8.5 µm. Nevertheless, if the particles are bigger than 11.5 µm many additional weak peaks in the WGM spectra can be observed. A new type of WGM particle sensors were developed by assembling the fluorescent dye molecules outside of the particle on its surface. Nanometer thin layers of coumarin covalently linked to polyelectrolytes were assembled by the LbL technique on non-fluorescent PS particles yielding highly qualitative WGM sensors with narrow bandwidth, low background signal, and easy post-modification possibility. However, continuous measurement lead to a faster photobleaching of the dyes than for dyes immobilized inside the PS particles.

The studies of sensing performance showed that the low-Q WGM system can be compared with other well-established label-free detection methods such as SPR or QCM and successfully used for the analysis of the binding and release kinetics of many molecules such as polymers, proteins or antibodies.

The obtained results suggest that fluorescent low-Q WGM particles have a great potential for their future application as small scale sensors for label-free, low-cost and multiplexed detection of (bio)molecules.

Streszczenie

Intensywny rozwój badań prowadzony w ostatnim dwudziestoleciu nad bezznacznikowymi (ang. *label-free*) technikami diagnostycznymi wykorzystującymi specyficzne bioczujniki przyczynił się znaczącego udoskonalenia analityki medycznej a tym samym do szybszej i bardziej wiarygodnej diagnozy wielu chorób człowieka, takich jak nowotwory,[1,2] choroby autoimmunologiczne[3] czy infekcje patogenne.[4,5] W porównaniu do klasycznych i powszechnie stosowanych metod diagnostycznych, w których detekcja oparta jest o znakowanie cząstek receptorowych markerami fluorescencyjnymi lub radioaktywnymi w celu uwidocznienia reakcji wiązania z ligandem, metody bezznacznikowe wykorzystują optyczne,[6,7] elektryczne[8] lub mechaniczne[9,10] przetworniki informacji o biochemicznych oddziaływaniach międzycząsteczkowych w mierzalny sygnał. Takie podejście pozwala na wyeliminowanie czasochłonnych i kosztownych modyfikacji cząsteczek receptorowych, zachowując ich strukturę, ładunek powierzchniowy i bioaktywność w stanie natywnym.

Ze względu na dużą szybkość i czułość detekcji, a także możliwość śledzenia kinetyki reakcji w czasie rzeczywistym oraz łatwość automatyzacji pomiarów, bezznacznikowe systemy bioczujników wykorzystujące mechanizm przetwornika optycznego, takie jak klasyczny powierzchniowy rezonans plazmonowy (*SPR*)[11] oraz jego odmiany (np. *imaging SPR, localized SPR, lattice SPR*),[12,15] interferometria biowarstw (ang. *biolayer interferometry, BLI*),[13] czy spektroskopia interferencji reflektometrycznej (ang. *reflectometric interference spectroscopy, RIfS*)[14] cieszą się obecnie duża popularnością. Jednakże duża wadą wymienionych wyżej metod jest stosowanie geometrycznie płaskich oraz stosunkowo dużych (w zakresie kilku milimetrów) bioczujników, które są zwykle na stałe związane z elementami optycznymi detektora. To ogranicza ich zastosowanie w diagnostyce *in vivo* jak np. w śledzeniu ekspresji białek wewnątrz pojedynczych komórek lub tkanek. Ponadto, z uwagi na ich wysoką wrażliwość na niewielkie zmiany temperatury otoczenia, wymagane jest stosowanie odpowiedniej aktywnej izolacji termicznej aparatury detekcyjnej, co z kolei znacznie podnosi koszty produkcji urządzeń pomiarowych.

Biorąc pod uwagę znaczące ograniczenia powszechnie używanych biosensorów optycznych, zaproponowane w niniejszej pracy mikrometrowe, kuliste bioczujniki wykorzystujące zjawisko optycznego rezonansu *Whispering Gallery Mode (WGM)* w celu transformacji sygnału

biochemicznego na elektromagnetyczny, wydają się obiecującą koncepcją dla nowej generacji bezznacznikowych metod diagnostycznych.

Zasada działania mikrorezonatorów WGM opiera się na wielokrotnym totalnym wewnętrznym odbiciu fali świetlnej w zamkniętym ośrodku (sferze) o współczynniku załamania światła wyższym niż współczynnik załamania światła otoczenia, wskutek czego dochodzi do jej interferencji i powstania specyficznych modów określanych jako *Optyczne Rezonanse Modów Galerii Szeptów* (ang. *Whispering Gallery Modes, WGMs),*[42-45] co historycznie wzięło swoją nazwę od kopuły (ang. *gallery dome*) katedry św. Pawła w Londynie, w której to w 1878 roku sir Lord Rayleigh badając odbicie fal dźwiękowych wewnątrz sferycznych obiektów, odkrył zjawisko rezonansu WGM.[69,70] Jednak kluczem do wykorzystania rezonatorów WGM jako swoistych (bio)sensorów stała się zależność między długością fali modów interferencyjnych WGM a średnicą optyczną rezonatora oraz jego współczynnikiem załamania światła. Każda niewielka zmiana jednego z ww. czynników, wskutek np. oddziaływania modyfikowanej powierzchni rezonatora ze specyficznym ligandem, powoduje proporcjonalną zmianę długości fali modów interferencyjnych widoczną jako przesunięcie spektralne rezonansu WGM. Śledzenie zmian długości fali pików rezonansowych pozwala tym samym na badanie kinetyki reakcji biochemicznych zachodzących na powierzchni mikrorezonatora WGM w czasie rzeczywistym.

Biorąc pod uwagę technikę wprowadzania fali świetlnej do wnętrza zamkniętego układu sferycznego rezonatora, należy rozróżnić rezonatory WGM wzbudzane z użyciem światłowodu bądź pryzmatu oraz zjawiska przenikania fali światła w polu zanikającym (ang. *evanescent field*) na granicy rezonator/otoczenie (zwykle rezonatory o dużej średnicy i wysokim parametrze dobroci Q oznaczane jako *High-Q WGM*)[43,47] oraz rezonatory WGM, w których rozchodzenie się fali świetlnej zachodzi na skutek wzbudzenia barwnika fluorescencyjnego lub kropek kwantowych znajdujących się wewnątrz ich struktury (rezonatory o małej średnicy i niskim parametrze dobroci Q oznaczane jako *Low-Q WGM*).[44,49-51,53] Należy zaznaczyć jednakże, że w odróżnieniu od klasycznych metod diagnostycznych, w których barwnik fluorescencyjny znakowanego ligandu może mieć bezpośredni wpływ na jego bioreaktywność i oddziaływanie z receptorem, fluorofory zawarte wewnątrz rezonatorów *Low-Q WGM* nie biorą udziału w reakcjach międzycząsteczkowych na ich powierzchni.[190]

Celem niniejszej pracy doktorskiej była synteza, charakterystyka fizykochemiczna i optymalizacja fluorescencyjnych mikrorezonatorów *Low-Q WGM* oraz ich wykorzystanie w

bezznacznikowej analizie biochemicznej. Przeprowadzone przeze mnie badania miały na celu stworzenie zaawansowanch optycznych bioczujników zdolnych do bezznacznikowej detekcji szeregu biomolekół i mających w przyszłości potencjalne zastosowanie w diagnostyce medycznej.

W pracy przebadano sześć kluczowych parametrów syntezy fluorescencyjnych mikrorezonatorów *Low-Q WGM* i ich wpływ na jakość sygnału i wydajność detekcji: rodzaj materiału rezonatora, typ polimeryzacji, rozmiar rezonatora, rodzaj i rozkład barwnika fluorescencyjnego oraz techniki funkcjonalizacji powierzchni. Zdolności detekcyjne nowo zsyntetyzowanych fluorescencyjnych mikrorezonatorów *Low-Q WGM* badano w oparciu o niespecyficzną adsorpcję na ich powierzchnii polielektrolitów oraz białka lizozym wykorzystując oddziaływania elektrostatyczne oraz wodorowe (metoda *Layer-by-Layer*). Oddziaływania specyficzne receptor-ligand badano poprzez modyfikację powierzchni mikrorezonatorów biotyną, a następnie wiązanie białka streptawidyna.

Praca została podzielona na sześć rozdziałów. W pierwszym rozdziale zatytułowanym *Introduction* przedstawiono ogólne wprowadzenie do optycznych metod detekcji bezznacznikowych ze szczególnym uwzględnieniem metody WGM i jej głównych zalet.

Rozdzial drugi, *Literature review*, przedstawia przegląd obecnie stosowanych metod detekcji bezznacznikowych wykorzystujących optyczne przetworniki sygnału biochemicznego (*SPR, Elipsometria, BLI* oraz *RIfS*) oraz ich porównanie w odniesieniu do metody WGM. W dalszej części zaprezentowane zostały fizyczne podstawy zjawiska rezonansu WGM, jego zarys historyczny oraz porównanie rezonatorów WGM o wysokiej i niskiej wartości współczynnika dobroci Q ze szczególnym uwzględnieniem technik wprowadzania fali świetlnej do wnętrza rezonatora. W ostatniej części rozdziału drugiego opisano metodę warstwowych pokryć powierzchni polielektrolitami (ang. *Layer-by-Layer, LbL),* będącej główną techniką wykorzystywaną do funkcjonalizacji powierzchni biosensorów WGM. Zwrócono szczególną uwagę na rodzaje i dobór polielektrolitów oraz wielofunkcyjne właściwości filmu *LbL.*

Rozdział trzeci, zatytułowany *Materials and Methods,* przedstawia charakterystykę technik eksperymentalnych oraz sposób syntezy głównych biomolekół użytych do badań. W pierwszym podrozdziale wymienione zostały materiały i odczynniki użyte w eksperymentach. Następnie została opisana synteza polikationu znakowanego barwnikami fluorescencyjnymi (*PAH-Rho i PAH-C343*) oraz polianionu znakowanego biotyną (*PMAA-biotin*) wykorzystując zarówno karbodiimidazol (*CDI)* jak rownież etyl-dimethylaminopropyl-karbodiimid (*EDC).* W

dalszej części przedstawiono opis innych metod stosowanych do modyfikacji powierzchnii biosensorów *Low-Q WGM*. W podrozdziale *Methods* przedstawiono opis technik analitycznych wykorzystanych do badań.

W rozdziale czwartym *Results and Discussion,* przedstawiono wyniki przeprowadzonych badań wraz z dyskusją. W pierwszym podrozdziale opisany został wpływ poszczególnych parametrów nowo zsyntetyzowanych sensorów o niskim Q na jakość, czułość i wydajność sygnału WGM. W szczególności zwrócono uwagę na oddziaływanie współczynnika załamania światła materiału rezonatora, chropowatość powierzchni, typ zastosowanej polimeryzacji oraz średnice rezonatora na właściwości rezonansu WGM. W ostatniej części podrozdziału pierwszego przedstawiono metody fluorescencyjnego barwienia mikrorezonatorów WGM oraz wpływ poszczególnych rodzajów fluoroforów i ich dystrybucji wewnątrz struktury rezonatora na intensywność i stabilność sygnału WGM. W podrozdziale drugim przedstawiono praktyczne użycie fluorescencyjnych mikrorezonatorów *Low-Q WGM* w bezznacznikowej analizie biomolekół. W pierwszej części badano niespecyficzną adsorpcję polielektrolitów na powierzchnii mikrorezonatorów WGM, wykorzystując oddziaływania elektrostatyczne (kombinacje PAH/PSS i PDADMAC/PSS) oraz wodorowe (PVP/PMAA). Następnie przedstawiono analizę porównawczą metody WGM, QCM oraz SPR na przykładzie niespecyficznego wiązania białka lizozym o różnym stężeniu. Oddziaływania specyficzne receptor-ligand badano poprzez wiązanie białka streptawidyna na powierzchni mikrorezonatorów *Low-Q WGM* funkcjonalizowanych biotynylowanym polielektrolitem (PMAA-Biotin). Zwrócono szczególną uwagę na wpływ liczby cząsteczek biotyny oraz zastosowanych polielektrolitów na ilość wiązanej streptawidyny. W ostatniej części podrozdziału drugiego mikrorezonatory *Low-Q WGM* zostały przetestowane pod kątem wykrywania zanieczyszczeń wody wywołanych rozpuszczalnikami organicznymi (THF, Toluen, Aceton). Na zakończenie każdego podrozdziału przedstawiono podsumowującą dyskusję.

Rozdział piąty, *Conclusions,* podsumowuje wyniki badań. Stwierdzono utworzenie idealnie kulistych, stabilnych oraz wysoce czułych biosensorów *Low-Q WGM* zdolnych do detekcji różnorodnych biomolekół.

Poniżej wymieniono ważniejsze wnioski płynące z przeprowadzonych eksperymentów:

1. Najlepszym rodzajem materiału do produkcji mikrorezonatorów *Low-Q WGM* jest polistyren (PS). Mikrorezonatory PS charakteryzują się wysoką intensywnością oraz

jakością sygnału WGM, a także niewielką szerokością połówkową (FWHM) modów rezonansowych. Badania z użyciem mikroskopii sił atomowych (AFM), skaningowej mikroskopii elektronowej (SEM) oraz WGM potwierdziły ich idealną kulistość, gładką powierzchnię oraz wysoki współczynnik załamania światła.

2. Użycie polimeryzacji spęczniania (*seed polimeryzation*) w procesie syntezy pozwala na łatwiejszą i bardziej precyzyjną kontrolę wielkość cząstek co tym samym zwiększa ich monodyspersyjność oraz przekłada się na polepszenie jakości, oraz wydajności sygnału WGM.

3. Optymalna średnica mikrorezonatorów *Low-Q WGM* zbudowanych z polistyrenu leży pomiędzy 8,5 a 11 μm. W tym zakresie mikrorezonatory PS charakteryzują się najwyższą intensywnością sygnału oraz najmniejszą szerokością połówkową modów rezonansowych. Dla średnicy powyżej 11 μm zaobserwowano pojawienie się dodatkowych pików interferencyjnych utrudniających prawidłową analizę widma rezonansu WGM.

4. Kumaryna 6 okazała się najlepszym barwnikiem fluorescencyjnym dla polistyrenowych mikrorezonatorów *Low-Q WGM*. Mikrorezonatory PS barwione kumaryną 6 charakteryzują się wysoką wydajnością oraz wartością molowego współczynnika ekstynkcji, a także dużą odpornością na fotowybielanie (ang. *photobleaching*). Względnie krótka długość fali emisji światła (479 nm) zwieksza wielkość przesunięcia modów WGM a tym samym czułość detekcji.

5. Immobilizacja barwnika fluorescencyjnego (kumaryna 343) na powierzchni mikrorezonatów PS z użyciem techniki LbL pozwala znacząco zmniejszyć wielkość sygnału tła fluorescencji, zachowując przy tym małą szerokość spektralną modów rezonansowych. Ponadto technika barwienia LbL umożliwia szybszą oraz łatwiejszą funkcjonalizację powierzchni mikrorezonatorów WGM białkami receptorowymi.

6. W porównaniu do innych bezznacznikowych systemów optycznych, takich jak SPR lub elipsometria, mikrorezonatory *Low-Q WGM* wykazują bardzo niską czułość na zmiany temperatury. Zaobserwowane przesunięcie widmowe rezonansu WGM mieści się w zakresie od 0.004 do 0.007 nm/°C.

7. Analiza adsorpcji polielektrolitów na powierzchni fluorescencyjnych mikrorezonatorów *Low-Q WGM* wykazała pozytywną zależność pomiędzy grubością warstw filmu LbL a stężeniem soli w roztworze polielektrolitu. Charakterystyczny,

ekspotencjalny wzrost filmu LbL w wysokich stężeniach soli zaobserwowano dla kombinacji PDADMAC/PSS. Kombinacja PAH/PSS charakteryzowała się wzrostem liniowym, który był w mniejszym stopniu zależny od stężenia soli w roztworze. Badania te potwierdziły wcześniejsze wyniki uzyskane metodą QCM oraz elipsometrią.

8. W detekcji niespecyficznej adsorpcji białka lizozym na powierzchni różnych typów optycznych biosensorów (SPR, QCM, WGM) najbardziej czułe okazały się mikrorezonatory WGM oraz QCM. Jednakże metoda WGM charakteryzowała się najwolniejszą kinetyką reakcji wiązania lizozymu co bylo spowodowane w głównej mierze ograniczeniami układu mikroprzepływowego.

9. Immobilizacja biotyny na powierzchni mikrorezonatorów *Low-Q WGM* przy użyciu techniki LbL pozwala na specyficzne wiązanie białka streptawidyna a tym samym na bezznacznikowe śledzenie kinetyki oddziaływań receptor-ligand w czasie rzeczywistym. Granica wykrywalności (ang. *limit od detection, LOD*) metody WGM dla streptawidyny została określona na 0.2 nM, co jest wynikiem porównywalnym z innymi optycznymi metodami bezznacznikowymi takimi jak SPR.

10. Wykazano, że fluorescencyjne mikrorezonatory *Low-Q WGM* mogą być również z powodzeniem stosowane w analizie zanieczyszczeń wody rozpuszczalnikami organicznymi takimi jak aceton, toluen czy tetrahydrofuran.

W rozdziale szóstym, *References,* zawarto spis literaturowy.

Na końcu pracy zamieszczony został mój krótki życiorys, lista publikacji oraz konferecji i sesji posterowych, w których brałem udział.

1 Introduction

In the last decade, a growing number of studies devote to the development of label-free analytical methods, contribute to a faster and more reliable diagnosis of many human diseases such as cancers,[1,2] autoimmune diseases[3] or pathogenic infections.[4,5] In comparison to common analytical techniques requiring labeling target molecules with fluorescent or radioactive markers to make the specific binding events visible, label-free methods exploit optical,[6,7] electrical[8] or mechanical[9,10] transducer mechanisms to translate the binding information into a measured signal. This approach allows eliminating time- and cost-consuming molecules modification and keeps their structure, surface charge, and bioactivity intact. In particular, the label-free biosensing systems applying optical transducer mechanism such as surface plasmon resonance (SPR),[11] biolayer interferometry (BLI)[13] or reflectometric interference spectroscopy (RIfS)[14] are rapidly gaining in popularity because of their fast assay development time, real-time kinetic analysis, the possibility of automation and high sensitivity. However, the high sensitivity is achieved usually by applying planar and relatively large (in the range of millimeters) transducer systems. That significantly limits the use of them in small volumes such as cell arrays or even inside cells. Furthermore, the large geometry often requires temperature stabilization, which in turn leads to high instrumental efforts and prices. Based on these limitations, miniaturization of such systems based on micrometer-sized spherical sensors such as fluorescent Whispering Gallery Modes microresonators proposed in this work seems to be a promising concept in new-generations of label-free diagnostic systems.

2 Literature review

2.1 Optical label-free detection systems

2.1.1 Surface Plasmon Resonance (SPR)

Surface plasmon resonance is the resonant oscillation of delocalized electrons (known as plasmons) in a thin metallic layer, which occurs in response to their excitation with a polarized light under total internal reflection conditions. The principle of the SPR technique is based on the detection of changes in the refractive index on a thin metal layer when material/molecules are adsorbed. SPR-based biosensing is a quantitative, real-time, and label-free detection method to follow bimolecular interactions.[15,16] A schematic principle of surface plasmon resonance technique is shown in Figure 1.
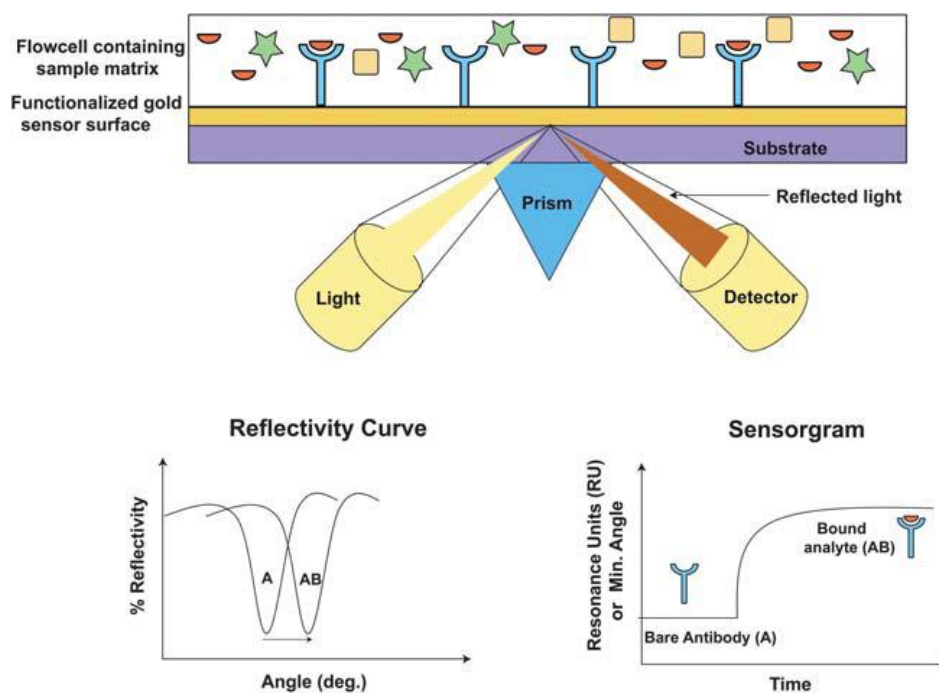
Figure 1. Principle of surface plasmon resonance technology. Adapted from [16].

There are three commonly used configurations of SPR-instruments: prism coupler-based SPR-systems, grating coupler-based SPR-systems, and optical waveguides-based SPR-systems.

Prism coupler-based SPR-systems

Most SPR detection systems are configured with a glass prism which couples polarized light directly into the sensor surface coated with a thin metal film. This approach can be applied using the Kretschmann or Otto arrangement (Figure 2). In Otto configuration, the prism is located below the metal layer with a small space filled with an optical medium possessing a low refractive index. In the case of light excitation, photons will be total internal reflected on the prism-space boundary. However, because of a close position of the metal layer, evanescent waves can pass through and excite the plasmons.[17] This approach is useful for monitoring interactions of solid-phase media. Due to the reduced sensitivity, the Otto configuration is less useful in applications with solutions.

In Kretschmann's arrangement, the metal layer is placed directly on top of the glass prism. In this case, the light wave comes from a high refractive index material (prism) and will be total internal reflected at the metal surface. The evanescent wave passes through the metal layer and plasmons are formed at the top layer of the film.[18] This approach offered advantages in freedom of design of the microfluidic system, enabling a more sensitive detection and independence of the analyzed material state.
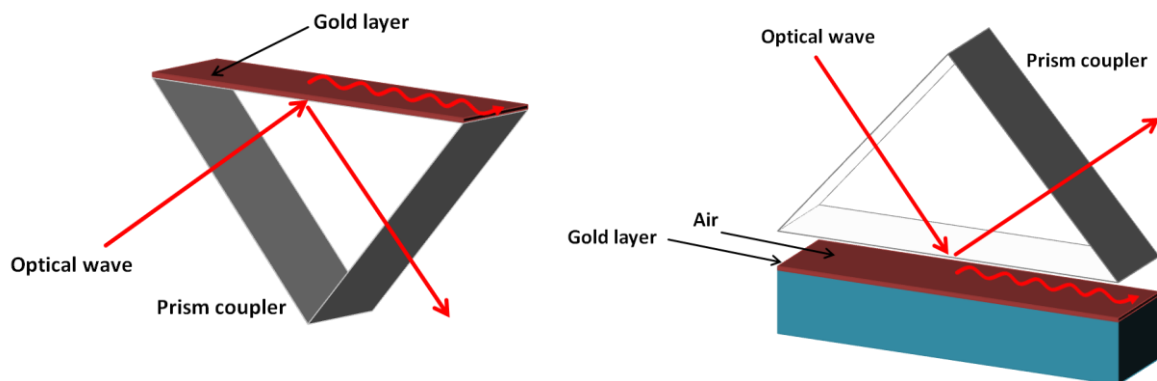
Figure 2. The Kretschmann (left) and the Otto configuration (right) of SPR.

Grating coupler-based SPR-systems

The application of diffraction grating (GC) as the coupler for SPR sensors was first proposed by Tiefenthaler and Lukosz in 1983.[19] In this configuration; glass prism is replaced by a diffraction grating covered with a gold layer (Figure 3). The flow channel is located over GC, therefore the angle at which light couples to the waveguide is dependent on the refractive index of analyzed molecules solution. By diffraction of waves at incidence angle, the grating generates light with larger wave-vector values than that of the incidence light.[20] Adjusting of

incidence beam angle enables to generate plasmons at the gold surface. In the case of molecules adsorption, the effective refractive index at the sensor surface is changing, and the incidence angle of the beam must be re-adjusted.
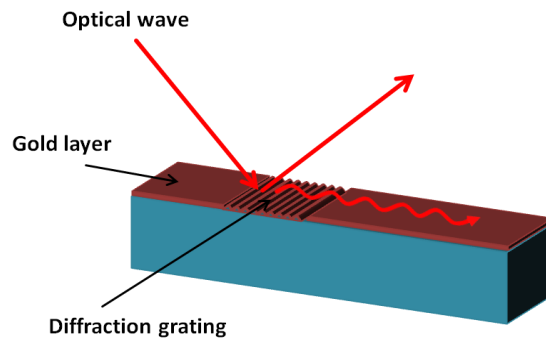
Figure 3. Diffraction grating SPR.

Fiber optic-based SPR-systems

The optical fiber as a waveguide in the SPR sensing system was first demonstrated by Jorgenson and Yee.[21] In this approach, the need for coupling prism or diffraction grating is eliminated by using the multimode fiberglass. The light from a polychromatic source is launched into the optical fiber and waves are propagated along with the core-cladding interface by total internal reflection. The surface plasmon resonance is realized by removing a certain portion of the silicon cladding from the fiberglass and coating the core with a thin metal layer such as silver. The evanescent waves formed by the total internal reflection of guided rays excite in further the surface plasmons at the core-metal sensing interface (Figure 4). By measuring the dip in the intensity of light leaving the fiber, a spectrometer can determine which wave coupled with the surface plasmons and consequently calculated the adsorbed mass of analyte.
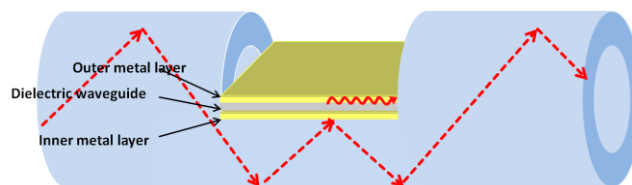
Figure 4. Fiber-optic SPR.

Fiber optic-based SPR-systems have many advantages over the prism- or diffraction grating SPR configurations. Basically, due to the small size and no requirement of complex optical and mechanical parts, fiber optic SPR-systems can be applied in many fields as miniaturized, portable biosensors. They also have a low fabrication cost and capability of remote sensing what makes them especially useful for in situ monitoring of biomolecular interactions and process controlling in industries.[22]

2.1.2 Ellipsometry

Ellipsometry is an optical technique used for determining film thickness and roughness as well as the optical properties of materials and visualization of biomolecular interactions. Fundamentally, ellipsometry measures the changes in polarization as the light beam is reflected or transmitted from a material surface.

Ellipsometers are configured with a single-wavelength light source, two polarizers, optional compensators, and detector (Figure 5a). The unpolarized light source is typically a low power He-Ne laser (emission at 632.8 nm) or a high band Xe arc lamp.[24] As polarizer, calcite, or quartz crystal is widely applied.[24,25] The light emitted from the source passes through the polarizer being linear polarized. After reflection from the sample surface, the light becomes elliptically polarized and falls into the second polarizer, which is called analyzer. A detector is placed behind the analyzer and converts light to a voltage whose dependence yields the measurement of the reflected polarization. In some configurations, a compensator (usually a retarder) is set between a polarizer and sample to converts linearly polarized incidence light to elliptically or circularly polarized. This optical element enhances measurement accuracy and deprives ellipsometry of some limitations.[24,25] Depends on the material sample and film structure, three general types of ellipsometers are used: null, phase modulating, and rotating elements ellipsometer.

The ellipsometry measures the changes in two components (also called ellipsometric angles): relative amplitude - Ψ and phase difference – Δ which characterized p-polarized and s-polarized light. P-polarized light is oscillating parallel to the plane of incidence, whiles-polarized light is oscillating perpendicular to the plane of incidence (Figure 5b). The changes in ellipsometric angles are described by the relation:[24,]

$$\rho = \frac{R_p}{R_s} = \tan \Psi \exp(i\Delta) \tag{1}$$

Here, ρ is the complex reflectance ratio, R_p - reflectance coefficient of p-polarized light and R_s - reflectance coefficient of s-polarized light.
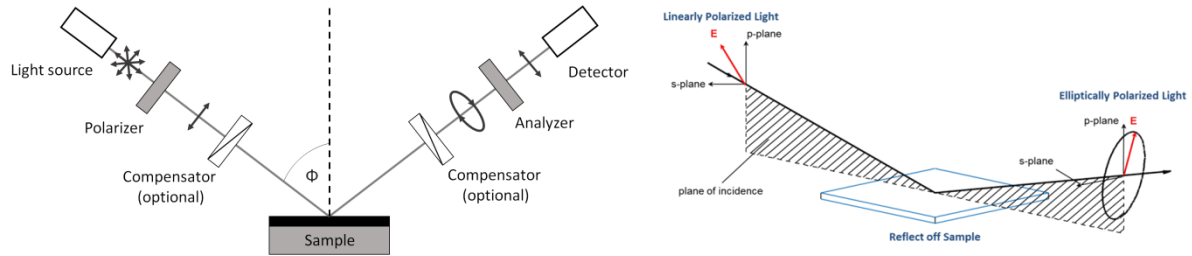
Figure 5. The basic scheme of ellipsometry components (left) and the general measurement principle (right). Adapted from [26].

One of the awkward disadvantages of ellipsometry is the limited possibility of direct conversion of the ellipsometric components to optical constants. To obtain relevant information about film structure and thickness as well as optical parameters of material, a model analysis has to be constructed.[27] In most cases, an appropriate model should contain optical constants as refractive index or dielectric permittivity of material and usually some physical parameters, e.g., a layer thickness. In follow, experimental Ψ and Δ values are converted to optical constants and matched with calculated data to find best-fit model.[24-27]

2.1.3 Reflectometric interference spectroscopy (RIfS)

Reflectometric interference spectroscopy (RIfS) is a direct optical method used in chemosensing systems as well as for investigating biomolecular interactions. RIfS is based on white light interference on thin layers and is corresponding to the operating principle of the Michelson interferometer. A schematic detection principle of RIfS is shown in Figure 6.
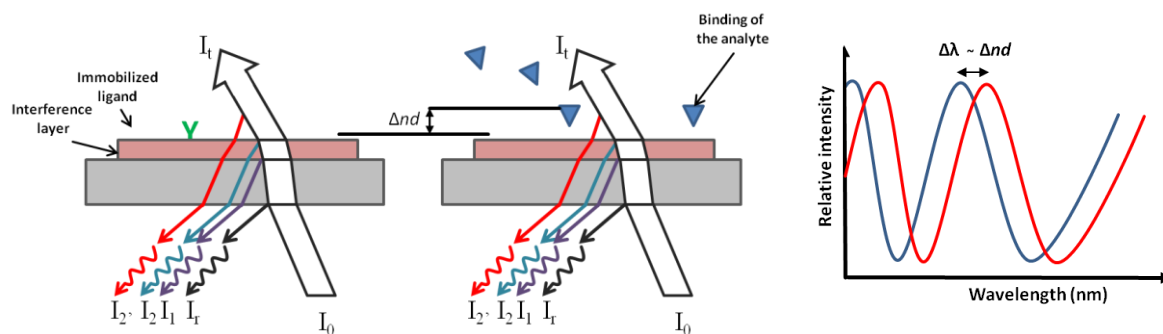
Figure 6. Principle of reflectometric interference spectroscopy.

A white light beam usually comes from a halogen lamp, is directed via an optical fiber onto a multilayer transducer. The RIfS standard transducer is made from glass (1μm in thickness) coated with a 10nm, Ta_2O_5 or Nb_2O_5 layer and on the top with a chemical modified SiO_2 layer (thickness around 330nm). The deposition of the tantalum or niobium oxide layer between SiO_2 layers enhances the interference contrast because of their high refractive index. The light beam is reflected at each phase boundary and transmitted into the detector (CCD camera). By binding of target molecules onto the chip surface, the optical thickness of the upper SiO_2 layer is changing. That makes a result in modulation of the interference spectrum. Optical thickness is the product of the physical thickness (d) and the refractive index (n) of the layer and can be determined from the position of an extremum with a given order value m by equation[28] :

$$nd = \frac{m\lambda}{2} \tag{2}$$

Monitoring the shift of interference spectrum vs. time allows observing the kinetic behavior and determination of binding constants of biomolecules. The RIfS technique enables to detect shifts in interference lower than 2 pm, which corresponds with an adsorbed mass in the order of magnitude of 1,5 pg/mm^2. Drift measured with the set-up ranges typically smaller than 10 pm/h.[29]

One of the main advantages of RIfS is its resistance to changes in temperature.[28,30] Other standard label-free sensing methods such as Surface Plasmon Resonance (SPR), Ellipsometry or Quartz Crystal Microbalance (QCM) show very high sensitivity to temperature variations. In the case of SPR and ellipsometry, even a small modification of temperature during the measurement cause changes in the refractive index (due to changes in density). The RIfS

method depends on the refractive index as well as the physical thickness of the sample. Thereby, if the temperature increases the refractive index decreases but contrary, the material thickness rising as a result of thermal expansion. That makes RIfS a suitable technique in many applications where temperature can fluctuate, for instance, in-vitro measurements. RIfs has been successfully employed to measure a variety of biomolecular interactions such as antibody affinity[28] adsorption of biopolymers,[31,32] cell adhesion[30], or epitope mapping.[33] Moreover, RIfS finds application in modeling and investigating of membrane proteins and their behavior.[33-35]

2.1.4 Biolayer interferometry (BLI)

Biolayer interferometry (BLI) is an optical, label-free analytical technique for measuring biomolecular interactions. This technology was pioneered and developed by the ForteBio Company and used in the flagship product: Octet® system.[36]

The measuring principle of BLI based on analysis of the interference pattern of white light reflected from two interfaces in a fiberglass biosensor: an internal reference interface located between the fiberglass and the outer proprietary bio-compatible layer and an interface between the surface chemistry and surrounding solution (Figure 7). When waves propagate back from two reflecting surfaces, they interact and generate constructive (red) or destructive (blue) interferences that vary with the wavelength (Figure 8a). Any change at the outer bio-compatible layer of the biosensor, for example, due binding of the ligand, leads to an increase in the optical path length and to change the interference pattern while the reflection from the internal layer remains the same. Plotting for all the wavelengths results in a new interferometric profile that is shifted to the right from the original pattern (Figure 8b). The shift in the wavelength ($\Delta\lambda$) is directly related to the change in the thickness of the biological layer and can be monitored in real-time. However, in comparison to other label-free analytical methods, the BLI technique is unresponsive for changes in the refractive index of the surrounding medium, the unbound molecules or variation in flow rate. It is a unique advantage that allows it to be the accurate and precise measuring of large samples, including crude cell lysates or periplasmic samples.
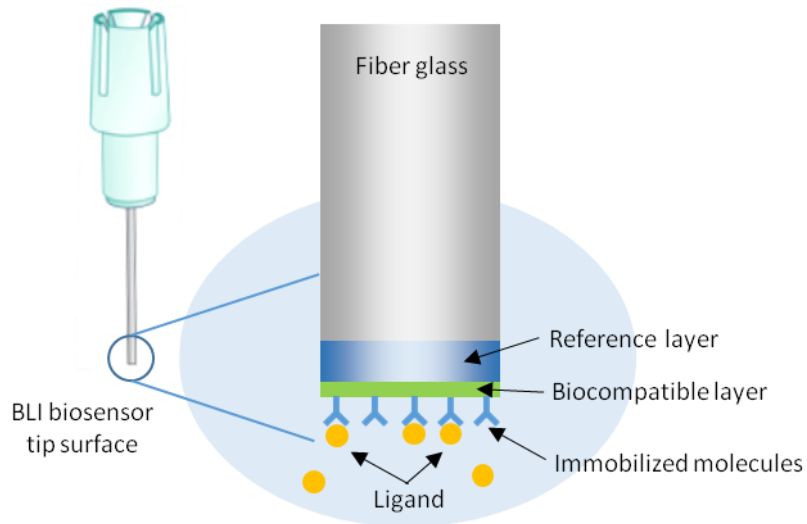
Figure 7. The schematic construction of BLI glass fiber-based biosensor.
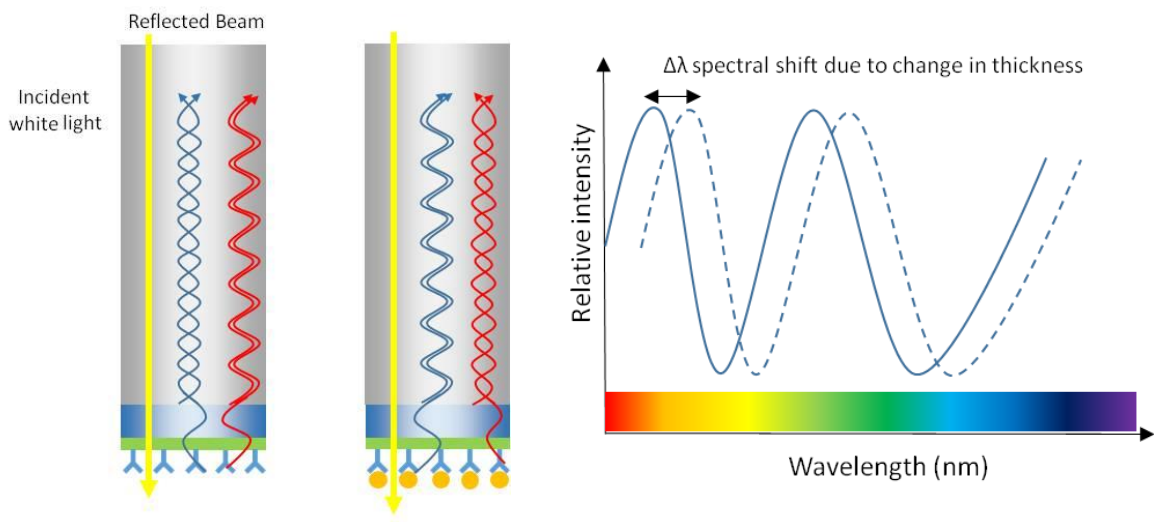
Figure 8. Principle of Biolayer Interferometry.

In the last decade, biolayer interferometry was extensively used to quantitative and qualitative characterize the molecular interactions of a wide variety of biomolecules, including proteins,[37] nucleic acids,[38] drugs[37,39], and viruses.[40] Wartchow was successfully applied BLI technology to determine the binding profile of small molecule fragments in the drug discovery process.[41]

2.1.5 Whispering Gallery Modes (WGMs)

2.1.5.1 Theory of Whispering Gallery Modes

Principle

Whispering Gallery Modes (WGMs) are specific eigenmodes of natural waves (e.g., acoustic waves, electromagnetic waves or various subatomic particle waves) circulating a concave surface (a cavity). This circulation is supported by continuous total internal reflection (TIR) at an interface of cavity and medium and allows building constructive interference (Figure 9a). WGM resonance can only be formed when the length of the optical path equals an integer number of wavelengths inside the resonator and depends significantly on its radius as well as the refraction index. Traditionally, the term whispering gallery mode refers to electromagnetic surface oscillation occurring in dielectric cavities.[42]

(a)   (b)
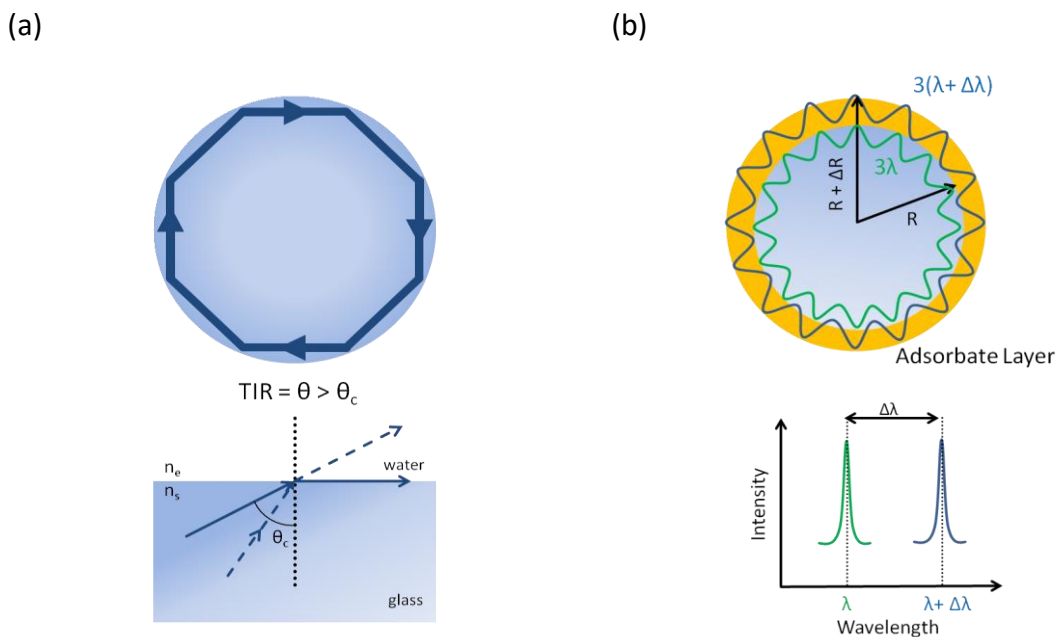
Figure 9. Total internal reflection (TIR) in the spherical resonator (a) and schematic illustrating the change in path length taken by light upon the adsorption of material to the surface of spherical WGM microresonator (b). Adapted from []

The fundamental sensing principle of WGMs resonators is based on measuring changes in resonance frequencies as a result of chemical-physical modifications on the surface. As the light is reflected at the cavity edge, a portion of photons extends around 200 nm outside the cavity forming the so-called evanescent wave.[43] This wave propagates tangential to the surface and is characterized by its high sensitivity to any changes in optical geometry or

refractive indices of the resonator as well as the surrounding environment. Binding of nanoparticles or single molecules on the resonator' surface increases the optical path length of the photon orbit, perturbing at the same time the resonance profile[43] (Figure 9b). This change is detectable as a shift (Δλ) in the spectral position of a WGM resonance and can be calculated according to the elementary ray optics model: [43,44]

$$\Delta\lambda = \frac{2\pi n_s \Delta R}{l} = \lambda \frac{\Delta R}{R} \tag{3}$$

Here, λ is the wavelength of the WGM with the integer mode number l, n_s the refractive index of the sphere, R it is radius and ΔR increase of sphere radius by adsorbate layer. This equation is a simple approximation as it will be explained in the next paragraph.

Parameters

WGMs are characterized by three mode parameters (indices) q, l, and m, which correspond to the radial, angular, and azimuthal modes numbers, respectively. The angular mode l specifies the full number of wavelengths that fit into the optical length of the equator. The radial mode q is equal to the number of field maxima along the radial direction whereas the azimuthal mode m describes the number of electromagnetic fields along the vertical angle φ at a given horizontal angle θ, i.e., perpendicular to the equatorial plane.[45,46] In perfect spherical resonator modes with the same l-number but different m-numbers are entirely dissipated. However, for spheres made by the melting of a fiber tip this degeneracy is typically removed and instead, they exhibit a spectrum rich with modes of different m numbers (usually called Higher Order Modes).[47] A graphical definition of coordinates and the effect of varying mode numbers are shown in Figure 10.
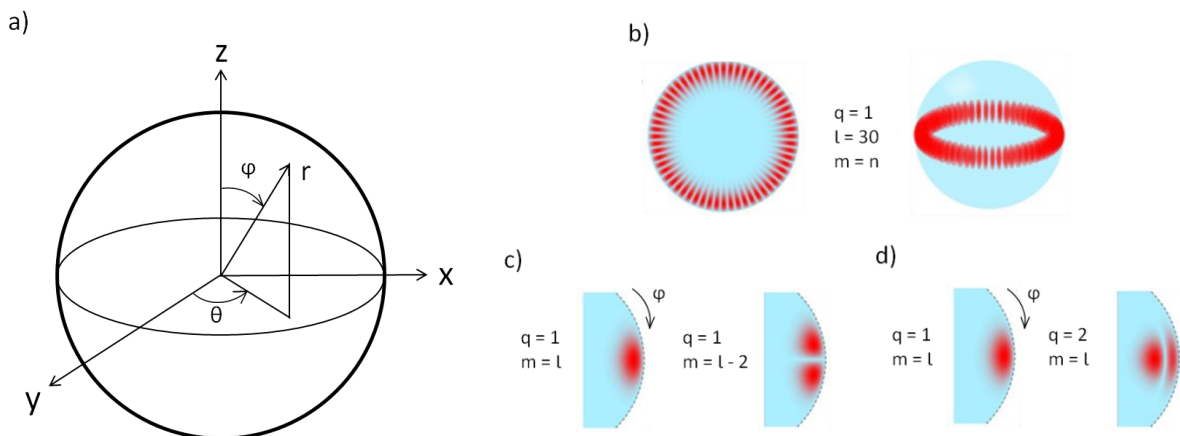
Figure 10. Definition of coordinates in WGM microresonator (a) and influence of different mode numbers: angular mode *l* (b), azimuthal mode m (c) and radial mode q (d). Reprinted from [46].

Depending on the polarization of light, two types of WGMs can be distinguished: transversal magnetic modes (TM-modes) and transversal electric modes (TE-modes). In the TM-mode, the magnetic fields are perpendicular to the normal of the sphere surface and parallel to the direction of light propagation, whereas in the TE-mode the electric fields are parallel to the normal of the sphere surface and perpendicular to the direction of light propagation[46] (Figure 11).
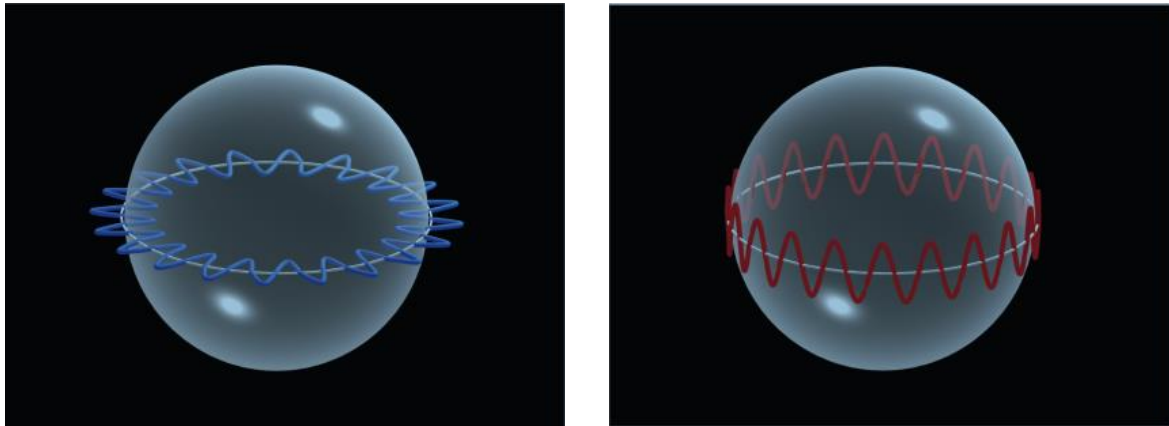
Figure 11. Schematic illustrating of two polarization modes in spherical resonator: transversal magnetic modes (TM-modes) (left) and transversal electric modes (TE-modes) (right). Reprinted from [48].

In the fundamental equation of mode position (equation 1) the polarization of WGMs, as well as the refractive index of the sphere's environment, is not accounted. The reason for this lack is related to the evanescent-field nature of WGMs.[44] At the dielectric sphere/environment boundary, WGMs are propagated along the surface of a denser medium (i.e., sphere) and reach only subtly out into the environment. In terms of decay length of the evanescent field, the influence of mode polarization for the geometrical radius of the sphere is small and can be ignored. Nevertheless, if the system is used to detect adsorption of specific molecules which changes remarkably the effective refractive index of the sphere's environment, the simple approximation of layer (adsorbate) thickness (ΔR) could be invalid. For this reason and accurate calculation, the difference between TM and TE modes should be distinguished.[44,49] Typically, the calculation of TM- and TE-modes in a dielectric microsphere with refractive index n_s embedded in medium with index n_e has been solved within the framework of Mie theory and presented in the form of infinite series of spherical Bessel functions. However in practice, because of tedious calculation, the Bessel functions were replaced by Airy approximation,[51] which can also be presented in the analytical form:[49-51]

$$\lambda_{\text{TE}} \,(q=1) = 2\,n_s\pi R \left[v + 1.8557v^{\frac{1}{3}} - \frac{n}{\sqrt{n_c^2 - 1}} + 1.0331v^{-\frac{1}{3}} - \frac{0.6186n^3}{(n_c^2 - 1)^{\frac{3}{2}}}v^{-\frac{2}{3}} + O(v^{-1}) \right]^{-1} \tag{4a}$$

$$\lambda_{\text{TM}} \,(q=1) = 2\,n_s\pi R \left[v + 1.8557v^{1/3} - \frac{n}{\sqrt{n_c^2 - 1}} + 1.0331v^{-1/3} - \frac{1.8557(n_c^4 - \frac{2}{3})}{n_c^3(n_c^2 - 1)^{3/2}}v^{-2/3} + O(v^{-1}) \right]^{-1} \tag{4b}$$

$$n_c = \frac{n_s}{n_e} \,, v = l + \frac{1}{2} \tag{4c}$$

Here, λ_{TM} and λ_{TE} are wavelength positions of first-order (q = 1). TM and TE modes located close to the particle surface. The value v is the order of Bessel function involved and related to mode number l. n_c is the contrast refractive index at the resonator/environment interface. In this work, Airy's approximation (equation 4) was used for simultaneous fitting of the measured mode positions λ_{TE} and λ_{TM} and determination of sphere radius R as well as refractive index (n_s and n_e).

One of the most important and widely used quantity characterizes sensing performance of WGM resonator is the quality factor (Q-Factor) defined as[42,43,45,52]

$$Q = \frac{\lambda_m}{FWHM} \tag{5}$$

Here, λ_m is the mode wavelength, and FWHM is the full-width at half-maximum. Q-factor describes the rate of energy loss of light during circulation within the resonator and can also be determined as a sum of absorption, scattering, and intrinsic diffraction losses.[42,53] These values significantly depend on the resonator's size, geometry as well as material type. For example, High-Q resonators, where the number of light circulations is specified from 10^4 to 10^6 (see also § 2.1.5.2) perform better resolution of wavelength shift, allowing detecting even single molecules.

On the other hand, they require larger diameter (typically d = 100 – 200 μm), so that the high wavelength resolution is diminished by the smaller relative changes in optical diameter during the adsorption of molecules (eq. 1). Hence despite of the lower Q-factor, the sensitivity of Low-Q resonators made with smaller particles (d < 12 μm) can be comparable to more commonly performed high-Q sensors. Table 1 shows typical Q-factor values of different resonator materials and shapes.

Table 1. A magnitude of Q-factor values for various resonator materials and shapes.

Resonator's shape	Material	Q factor in air/water	Diameter (µm)	Reference
sphere	silica (SiO_2)	10^9-10^{10}/10^6-10^8	0.5-1 x 10^3	[54], [55]
	polystyrene (PS)	/10^3-10^4	5-20	[44], [49], [50], [53]
	melamine-formaldehyde (MF)	/10^3-10^4	5.6-12	[56], [57]
	polydimethylsiloxane (PDMS)	10^4	37	[58]
	magnesium fluoride (MgF_2)	/10^8	5.8	[59]
	sapphire	10^5-10^9	$10^4 - 10^5$	[60], [61]
	calcium fluoride (CaF_2)	10^{10}	4-7 x 10^3	[62]
	$LiNbO_2$	10^8	0.7-7 x 10^3	[63]
	Fe^{3+}: Al_2O_3	10^9	data not available	[64]
toroid	titanium dioxide (TiO_2)	10^5/10^5	160	[65]
	silicon nitride (Si_2N_3)	10^5	224	[66]
disc	silicon carbide (SiC)	10^4	12.5	[67]
goblet	poly(methyl methacrylate) (PMMA)	10^6	40	[68]

History of WGM's

The Whispering Gallery Modes term was first proposed by John William Strutt, better known as Lord Rayleigh, almost a century ago in publication: "Problem of the Whispering Gallery".[69] He studied the characteristic of acoustic waves, traveling around the dome of St. Paul's Cathedral in London. According to his observation, the intensity of sound propagated along the dome wall decreased only proportionally to the distance from a source, while at any others points in free space of the dome interior the decreasing of sound intensity was proportional to the square of the distance.[69,70] He explained this effect as a series of specular reflections of sound rays, which circulate along the curved wall and build a constructive interference. Furthermore, he predicted that the whispering gallery phenomenon would also exist for light or other waves and could find practical application due to the extreme confinement of the field. At the same time, Debye, Lorentz, and Mie independently studied adsorption and scattering of electromagnetic waves in free dielectric and metallic spheres. Their results, today knows as Lorentz-Mie-Debye solution (or shortly Mie scattering), provided a first theoretical and mathematical explanation for resonant eigenfrequencies within small cavities.[71,72] A couple of years later, Richtmyer showed that suitably shaped objects as microparticles or

microrings made of a dielectric material could sustain high frequencies oscillations.[73] He developed the theory that losses of resonance intensity could be significantly reduced by applying larger resonators in comparison to the wavelength. The first observation of fluorescent emission into optical WGMs of spheres was performed by Garrett et al. in 1961.[74] They measured pulse laser oscillations in highly polished CaF_2 crystals with diameters of 1-2 mm doped with samarium and placed in a dewar containing liquid hydrogen.

WGMs have also been observed in liquid microspheres. In 1984 an inelastic laser emission from individual ethanol droplets suspended in the air (60μm diameter) and containing rhodamine 6G was detected by excitation them with a cw laser (545.5 nm).[75] Biswas et al. produced high-intensity nanosecond pulses by irradiation micrometer-sized droplets of a water/ethanol mixture doped with Rhodamine 6G using a frequency-doubled Nd: YAG laser. They noticed that the coupling of the spontaneous fluorescence emission with natural resonant modes of the spherical droplets resulted in stimulated emission, with each droplet behaving like a laser cavity.[76] However, despite the secure handling and stability of such liquid microresonators, their quality (Q) factor was relatively low (~10^4).

The first WGMs with very high-quality factor (~10^8) were detected in 1989 in solid silica microspheres formed by melting the tip of optical fiberglass using a torch.[77] Several years later, Gorodetsky et al. performed experiments with an ultimate Q factor of – 10^{10} of whispering gallery modes in fused-silica microspheres measured in air at 633 nm.[54] This value was in the magnitude of today's experimentally measured Q-factors. However, its value is still smaller than the (theoretical) limit determined by Mie and Debay.[71,72] Leakage during the circulation of light is caused by many factors, for example, radiative losses, contaminations, material absorption, scattering by surface imperfections or bending losses by the curvature of the cavity[54].

The practical sensing application of WGM resonators was first demonstrated in the early 1990s. Rhodamine- containing liquid droplets with a diameter between 13 to 18 μm were used to monitor the changes in pH by measuring the absorption of an indicator dye.[78] A few years later, Serpengüzel et al. proposed WGM resonators as promising and very sensitive biosensors.[79] Here, 10 μm polystyrene microspheres were embedded in water and excited by an optical fiber coupler. They calculated a minimal detectable layer thickness for such beads of 0.01 nm, which allowed supposing that the detection of molecules with molecular weights smaller as typical proteins (50kDa) could be possible. In 2002, silica microspheres coupled with

optical fiber as waveguide was used to measure the adsorption of low concentrated bovine serum albumin (BSA) solutions as well as the binding of streptavidin on biotinylated BSA.[80] Since this time, WGM resonators have been widely used in detection of bacteria,[81] cells,[82] viruses,[83,84] DNA,[85] RNA,[86] antibodies,[86] exosomes,[87] single protein molecules or tumor markers.[87-90] It was also applied to determination physical properties of materials including size,[91,92] temperature,[91,93,94] pressure,[95,96] force,[97] refractive index[91,92] and electromagnetic field.[98,99]

2.1.5.2 High-Q WGM resonators

Generally, the term high-Q WGM resonator is related to resonators with Q-factor from 10^4 up to 10^6 and ultra-high-Q to resonators with Q-factor above 10^7. High-Q WGM resonators can confine light over a long period because of their large diameter, minimal reflection losses and potentially shallow material adsorption (e.g., in dielectric materials). Moreover, in comparison to single-pass optical methods (e.g., surface plasmon resonance or reflectometric interference spectroscopy), where the light interacts with target molecules only once, high-Q resonators show significantly better sensitivity performance due to enhancing the interaction between the light and a bound analyte.[47] On the other hand, large resonators show the smaller magnitude of resonance shift ($\Delta\lambda$), because bound molecules increase the optical path length only slightly. Sharp resonance modes and small shifts require specific optical conditions and high-resolved photodetectors, which enhance the costs and complexity of the detection setup. While the label-free sensing systems based on high-Q resonators promised utmost sensitivity and were used in many sensing applications, these limitations as well as the need for precise light coupling devices (see below) significantly constrict their commercialization and marketing.[50]

Overview of coupling method

An essential aspect of the fabrication of High-Q-WGM microsensors is the efficiency and robustness of light coupling from the outside. Methods based on a free-beam optic are not practical due to fragile radiative transfer to WGMs which can be seen as a quasi-bound state of light trapped inside a dielectric material. Hence, in recent years several coupling schemes rely on energy transfer between a resonator and waveguide via evanescent field have been

developed. Figure 4 shows typical approaches to couple light into symmetric optical microcavities.

One of the oldest methods applied is a prism coupling configuration based on frustrated TIR[100] (Figure 12a). Typically, this approach shows efficiencies close to 80%, but because of the large number of possible output modes, it has a lower practical utilization.[101] More recently, tapered fibers with a micrometer or even smaller diameters have been used to the evanescent coupling of High-Q resonators (Figure 12b). This technique allows achieving almost 100% efficiency for coupling fused silica resonators.[102] On the other hand, this configuration is very tedious in handling due to the requirement of precise control of the distance between the coupler and resonator's surface down to a few tens of nanometers.[103] Another disadvantage for practical application of the tapered fiber couplers is their fragility.[101] The evanescent coupling can also be realized with half-block couplers[104] (Figure 12c) or by using angle-polished fibers[105] (Figure 12d). However, these methods are less efficient although they have the advantage of being more robust.[106]
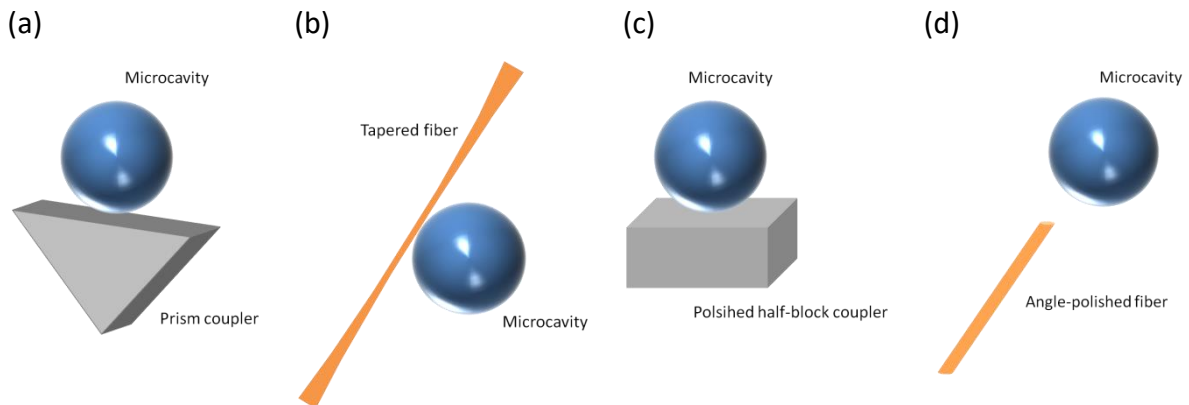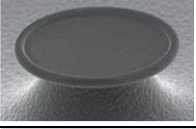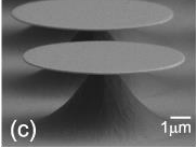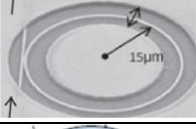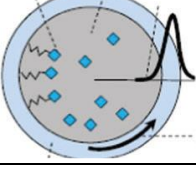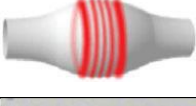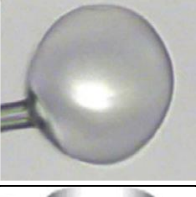
Figure 12. Schematic presentations of light coupling into WGM resonators. Prism coupling (a); Tapered optical fiber coupling (b); Half-block coupling (c) and angle-polished optical fiber coupling (d). Adapted from [106].

Types of High-Q WGM resonators

There is a multitude of different resonators geometries proposed for WGM sensing. Table 2 summarizes the most recent microcavity geometries that have been used in biosensing applications.

Table 2. Examples of different types of proposed High-Q-WGM resonators. Adapted from [47].

Optical resonator	Device example	Q-factor in air/water	Diameter	Fabrication
Microspheres, waveguide coupled [43], [54], [107], [108], [131]		$10^{10}/10^7$–10^8	50–500 µm	Usually formed by melting a fiber tip
Microtoroids, fiber coupled [111], [112], [113]		$8 \times 10^8/10^7$–10^8	30-200 µm	CO_2 reflow of an undercut silica micro-disk on silicon wafer
Microdisk, waveguide coupled [114], [115], [116]		~10^4	10–100 µm	Fabricated from silicon oxy-nitride film on a silicon wafer by lithography technology
Microgoblet, waveguide coupled [117]		10^5-10^6	50 µm	Mask-based optical lithography using thermal reflow
Ring resonators, waveguide coupled [118], [119], [120], [121]		/4×10^4–2×10^5	20–200 µm	Fabricated by lithography technology
Capillary, fiber-coupled (LCORR) [122]		/10^5–10^7	~150 µm	Softening (CO_2 laser) and stretching a fused silica capillary
Bottleneck resonator [123]		~10^8	30–40 µm	Fabricated from standard optical glass using a two-step heat-and-pull process
Microbubble [124], [125], [126]		10^3~10^7	70~500 µm	Heating a glass capillary with a CO_2 laser
Microcoil [127], [128], [129]		10^6	500 µm	Wind a microfiber coil on a cylindrical rod with lower refractive index

Most commonly applied High-Q resonators are microsphere cavities. They can be easily fabricated from glass or polymer optical fiber by heating and stretching the extremity with hydrogen torch[54] or CO_2 laser beam[130]. Excitation is typically realized by the same supporting fiber or by another fiber placed close to the microspheres' surface (coupling via evanescent field). Dielectric microspheres are usually fabricated in the range of 50-500 µm and

characterized by very high Q-factors up to 10^7-10^8 (in water) in the visible/near-infrared region.[43,47,108,131] Thanks to extremely sharp WGMs and utmost sensitivity, spherical resonators are one of the best candidates for single-molecule detection[132].

Another interesting resonator's geometry is micro-toroids, -disks or -goblets fabricated from silicon[133,135], glass[111,112] or polymers[136,137] by using photolithographic techniques, dry etching, deposition, or pattern transfer. Such structures have simpler mode spectra than spheres due to their confining and flat geometry. Those resonators exhibit "cleaner" WGMs (less Higher Order Modes) and reduced scattering losses (high Q-factor) because of fewer surface imperfections and more controllable shape. Another advantage is the possibility of easy up-scaling and combining them with microfluidic systems, which allows the production of multiple sensors chips for chemical or biological detection.

An exciting category of High-Q-WGM sensors are ring resonators. Typically, they are made from silicon, silicon nitride, glass or polymers using different lithographic techniques as UV lithography, electron-beam lithography or focused-ion-beam lithography. A great practical advantage of those resonators is the facility of waveguide coupling, which can be directly etched on the resonator platform. Presently, a multiplex photonic detection system based on WGM ring resonators (Maverick) is offered by Genalyte.[138] There are twelve chips per platform: each containing two sample channels with 16 ring resonators of 30 μm in diameter, made from silicon in standard etching technique. This system can detect up to 24 samples against 16 analytes or 12 samples against 32 analytes.

Liquid core optical ring resonators (LCORR or capillary resonators) are another form of resonator conventional used as WGM sensors. They are derived from thin tubular structures (microcapillaries) by softening and pulling a glass capillary (total diameter of 50-75μm).[47,52] This configuration offers a significant advantage because it is easily integrated within a microfluidic system where the analyte flows inside a capillary and interacts with the internal evanescent field of the resonator. The protein detection limit of such LCORR was determined in the sub-pg/mm^2 range.[139]

2.1.5.3 Low-Q WGM resonators

WGM resonators operating in the so-called low-Q regime (Q-factor <10^4) exhibit significantly broader bandwidths (typically in the range of 0.02-0.2 nm)[44] compared to high-Q resonators due to their smaller size and lower reflection possibilities. Their low wavelength resolution

seems disadvantageous in terms of sensor sensitivity but can be at least partially compensated by their larger magnitude of wavelength shift according to the equation 1 ($\Delta R/R = \Delta\lambda/\lambda$). Moreover, because the free spectral range of WGM modes scales inversely with particle size, smaller particles offer a bigger distance between peaks that facilitate their detection in a simple spectroscopic system.[50] The possibility of distinguishing more than a single mode position is a unique advantage since mode spacing contains information about the resonator dimension.[44]

Generally, low-Q WGM resonators can be evanescent field coupled using standard methods such as a prism or tapered fiberglass. However, in contrast to sub-millimeter high-Q spheres usually made from silica or crystals, low-Q microbeads have been prepared from other materials such as polystyrene[44,49,50,53,110] or melamine formaldehyde[56,57] because of their smaller dimension (typical diameters are between 6-12 μm). The use of polymeric materials simplifies the synthesis, making it also more controllable. However, the critical advantage of polymer substrates is the possibility of incorporation of fluorescent dyes or quantum dots inside the particle matrix and remote WGMs excitation by an external light source, i.e., diode laser (Figure 13a). Detection of WGMs is performed by a highly resolving spectrograph displaying peaks in the fluorescence emission spectra (Figure 13b). This approach eliminates the need for awkward evanescent field coupling making the Low-Q microparticles easier in handling, remotely operable and opens an opportunity for simple multiplexing.[50]
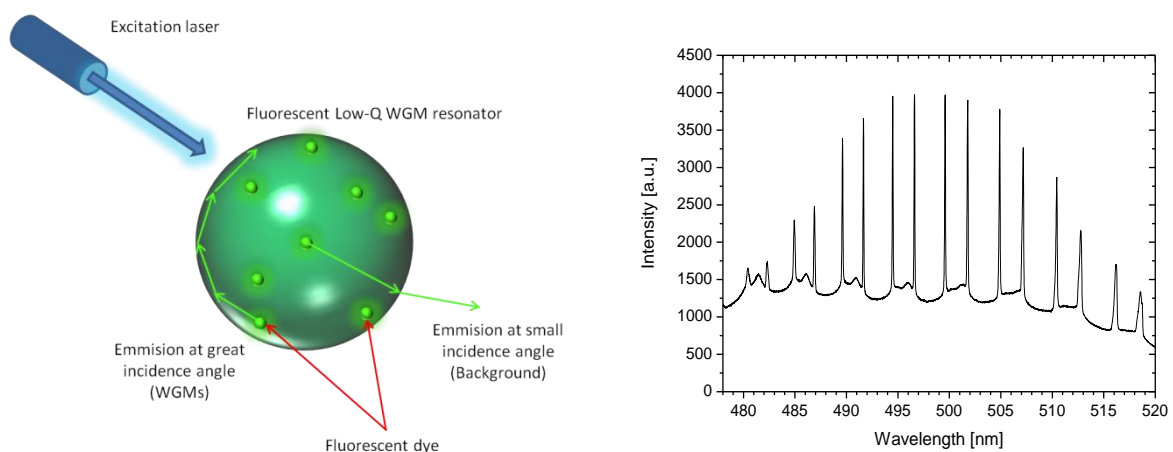
Figure 13. The principle of fluorescent low-Q WGM resonators (left) and typical WGM spectra of fluorescent polystyrene microbeads (right, nominal diameter 10 μm, measured in water).

Label-free optical sensors based on Low-Q WGMs in fluorescent or quantum-dots microbeads have been investigated over thirty years for the determination of refractive indices,[51,140] biomechanical forces[97], and detection of biomolecules such as oligonucleotides[141] or proteins, e.g., streptavidin.[44,50] One of the crucial advantages of this system, compared to the other label-free sensing methods (including also High-Q WGM resonators), is the possibility for remote detection of reactions taking place directly in living cells.[97,142] Due to their compact size (smaller than most eukaryotic cells), low-Q microsensors can be incorporated into cell lysosomes via natural endocytosis processes and attend for instance in the monitoring of intracellular signaling mechanisms or production of proteins.

2.2 Layer-by-Layer thin film fabrication technique

The Layer-by-layer (LbL) self-assembly is a technique for fabrication multilayer thin films on various materials by alternating deposition of synthetic polymers,[143-146] colloids,[147] biomolecules (including proteins,[148] nucleic acids,[149] lipids,[150] polysaccharides[151] or viruses[152]) inorganic nanoparticles[153,] and even cells.[154] The basic principle based on multiple intermolecular interactions such as electrostatic interactions, hydrophobic interactions, or hydrogen bonding between multilayer materials themselves as well as substrates. LbL self-assembly technique offers simply a fabrication, low costs, quickly process control, and above all, an unprecedented versatility and functionality compared to the other thin film deposition methods.

Historically, LbL technology was first reported by Iler in 1966 in the work of multilayers structures on colloidal particles.[155] In fact, however, it was not until the late 1990s, when it became clear that multilayer films can also be formed on non-planar surfaces,[156] the LbL technology was rapidly gaining popularity. After forming of multilayer thin film on charged substrates by using of oppositely charged polyelectrolytes, performed by Decher and Hong,[143-145] LbL technique was introduced to different coating substrates such micro- and nanoparticles,[157] biomedical materials,[158] textiles,[159] paper or skin of fruits and plants.[160]

2.2.1 Polyelectrolytes

As mentioned, many different materials can be successfully applied in the fabrication of LbL films. The most used and well-described materials are commercially available, charged polymers known as polyelectrolytes. Generally, the term polyelectrolyte describes polymer (from the natural origin, e.g., DNA, alginic acid or synthetic origin, e.g., polyallylamine (PAH)) possessing dissociated ionic groups in their repeating units. Thus, besides macromolecular nature, they have also electrolyte character giving them several useful properties. Polyelectrolytes can be classified as polycations, polyanions, and polyampholytes according to whether a polymer chain has a positive charge, a negative charge, or both. The most common cationic groups in polycations are primary, secondary and quaternary ammonium ($-NH_3^+$, $-NRH_2^+$, and $-NR_3^+$) whereas the negative charge on polyanions comes from carboxylate ($-COO^-$), phosphonate, phosphate ($-PO_3^-$, $-PO_4^{2-}$), and sulfonate ($-SO_3^-$) groups.

Depending on the ionic groups and their dissociation constants, polyelectrolytes can be further divided into "strong" and "weak" types. Strong polyelectrolytes dissociate completely, possessing a permanent charge in the whole range of pH. Weak polyelectrolytes, in contrast, are only partially dissociated in solution since the dissociation degree of ionic groups is highly dependent on the pH value.

2.2.2 Assembly of LbL thin films on charged substrates

A simplified molecular concept of LbL self-assembly and correspond schematic coating process on a planar surface performed by immersion and spraying is shown in Figure 14. A positively charged substrate is incubated for several minutes with polyanion until the surface charge is reversed in the base of electrostatic adsorption. Since a defined surface charge is accomplished, an electrostatic repulsion provides self-limitations of the further adsorption of polyelectrolytes. The self-limiting process offers many benefits of LbL thin films such as homogenous layers, precise thickness, and well reproducibility. In the next steps, the none-adsorbed polyanions are removed by washing the substrate with water so that positively charged polyelectrolytes can be deposited. This alternating adsorption of polyelectrolytes can be repeated at will and leads to build-up a multilayer thin film.[143-146]
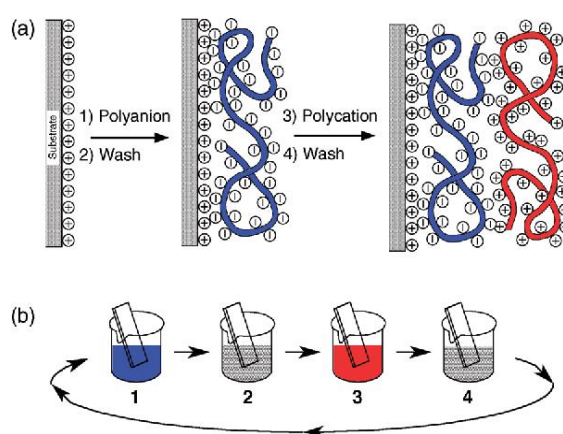
Figure 14. (a) Scheme of self-assembly adsorption of polyelectrolytes on a planar surface. (b) LbL-film deposition method using glass slides and beakers. In steps 1 and three glass slides are immersed in polyanion, and polycation, respectively, and steps two and four are washing steps. Adapted from [145]

Besides electrostatic forces between oppositely charged materials, there are several other interactions which have been successfully employed in LbL film assembly such as hydrogen

bonding,[161,162] hydrophobic interactions,[163] covalent bonding,[164] DNA hybridization[165,166] or steric interactions.[167]

2.2.3 Multifunctional properties of the LbL films

Basically, thin films having more than a single functional property can by produced by multifunctional LbL-coatings. In addition to charged groups, LbL-films can be equipped with different specific functional components including fluorescent dyes, biomolecules (e.g., antibodies, DNA, enzymes, hormones, polysaccharides, etc.), conducting or magnetic materials, nanoparticles or even living cells.[168] Of high interest in the last decade is a construction of drugs-delivery systems based on multifunctional LbL-carriers.[169] Unlike traditional methods to produce drug-delivery systems, the LbL-technique offers a large variety of biocompatible materials that can be fine-tuned to the nanometer scale, providing a tailored control of drug release. As it was already demonstrated, LbL-based drug-delivery systems have been prepared both on planar surfaces such as coronary stents[170,171] or soft contact lenses[172,173] as well as on micro- and nanoparticles (including capsules).[156,174,175]

Another example of multifunctional LbL thin film for biological applications is Polyelectrolyte Multilayer (PEM) systems engineered for controlled adhesion, growth, and proliferation of living cells or bacteria. As reported by Wittmer et al.[176], the use of (poly-L-lysine/dextran sulfate) film with incorporated fibronectin, promotes good adhesion and proliferation of human umbilical vein endothelial cells (HUVECs). In turn, Zhan et al.[177] demonstrated multifunctional antibacterial LbL films consisting of Hyaluronic acid and poly(amidoamine) dendrimer and assembled on biocompatible polyester poly(3-hydroxybutyrate-co-4-hydroxybutyrate). Improved hydrophilicity of the substrate surface produced by the LbL film was responsible for the bacterial adhesion resistance against E. coli. Besides a positive charge, PAMAM also exhibited bactericidal activity.

Multifunctional LbL assemblies can also be used for sensing applications. Loh et al.[178] presented multifunctional LbL thin films consisting of PSS/ poly(vinyl alcohol) and PSS/ polyaniline assembled on carbon nanotubes for mechanical strength and pH sensing. Carbon nanotubes based on similar LbL coatings were also used for development passive radio frequency identification (RFID)-based sensors for structural health monitoring (SHM) applications.[179] Another example is the highly sensitive electronic tongues achieved by

combining impedance spectroscopy measurements and the use of Langmuir–Blodgett or LbL films deposited onto interdigitated gold electrodes.[180] They were used not only to identify the basic tastes but also to distinguish between different wine[181] or coffee samples.[182]

3 Materials and Methods

In this chapter, all chemicals which were used in this work are listed. The syntheses of fluorescently labeled polyelectrolytes, biotin-labeled polyelectrolytes, and proteins, as well as other sample preparation, are described. In the second part, the basic principles of the used analytical techniques are presented with emphasis on their practical application in this work.

3.1 Materials

All chemicals were used without further purification. Fluorescent and plain polystyrene (PS) particles in diameter from 6.3 μm to 13.5 μm, melamine-formaldehyde (MF) particles in diameter from 4μm to 11.5 μm, poly(methyl methacrylate) (PMMA) particles, 10.7 μm in diameter were synthesized by Surflay Nanotec GmbH (Berlin, Germany). Uncolored silica particles (SiO_2) of 7.6 μm and PS particles of 9.3 μm were purchased from Microparticles GmbH (Berlin, Germany). Uncolored borosilicate glass particles (BS) and poly(methacrylic acid) (PMAA) (Mw = 100kDa) were supplied by Polysciences Inc (Eppelheim, Germany). Coumarin 6, coumarin 343, rhodamine B, poly(diallyl dimethylammonium chloride) (PDADMAC) (Mw = 200-350kDa), poly(allylamine hydrochloride) (PAH) (Mw = 15kDa), sodium poly(styrene sulfonate) (PSS) (Mw = 70kDa), poly(4-styrene sulfonate)-co-maleic acid sodium salt (PSS-co-maleic acid) (Mw = 20kDa), sodium dodecyl sulfate (SDS), bovine serum albumin (BSA) (Mw = 66 kDa), d-Biotin, biotin N-hydroxysuccinimide ester (Biotin-NHS), lysozyme (Mw = 14.3 kDa), 1,1'-carbonyldiimidazole (CDI), 4-(2-hydroxyethyl) piperazine-1-ethane sulphonic acid (HEPES), trifluoroacetic acid (TFA), sulfuric acid, N,N-Dimethylformamide (DMF), 1,2-dimethoxyethane (DME), xylene and tetrahydrofuran (THF) were purchased from Sigma Aldrich (Germany). Ethylenediaminetetraacetic acid disodium salt (EDTA), N-hydroxysuccinimide (NHS), N-Boc-ethylenediamine, and N, N'-dicyclohexylcarbodiimide (DCC) were supplied by Fluka (Steinheim, Germany). Poly(styrenesulfonate)-co-polystyrene (PSS-co-PS) was obtained from Tosoh (Tokio, Japan). Poly(vinylpyrrolidone) (PVP) (Mw = 45-54 kDa) were purchased from BASF (Weinheim, Germany). Streptavidin (Mw = 56 kDa) was obtained by Thermo Fisher Scientific (Waltham, USA). The biotinylated antibody was supplied by Exbio Antibodies (Vastec, Czech Republic). Biacore gold sensor chips were purchased from GE Healthcare (Penzberg, Germany). Toluene, sodium chloride (NaCl) and chloroform were

purchased from Carl Roth GmbH (Karlsruhe, Germany). 2-propanol, methanol, and ethanol were obtained by Merck (Darmstadt, Germany). Dichloromethane (DCM) was supplied by VWR Chemicals (Darmstadt, Germany). Dimethyl sulfoxide (DMSO) was purchased from Chemsolute (brand of TH Geyer, Germany).

All aqueous solutions were prepared with ultra-pure water from the three-step Purelab Pulse purification system (Elga, Germany). The chemical structures of used polycation and polyanions are presented in Figure 15 and Figure 16, respectively.
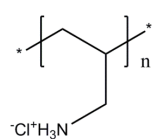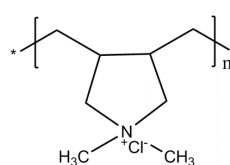
PAH*   PDADMAC*

Figure 15. Structural formulas of polycations used.
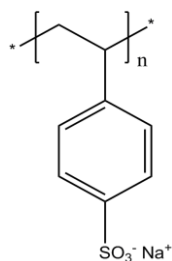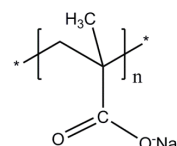
PSS   PMAA
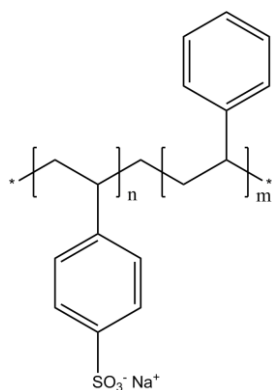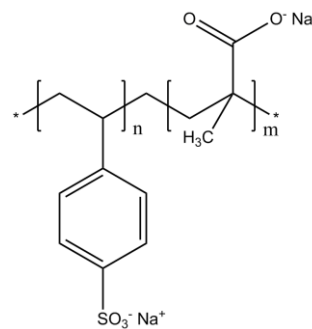
PSS-co-PS   PSS-co-Maleic acid

Figure 16. Structural formulas of polyanions used.

3.2 Synthesis of fluorescently labeled polyelectrolytes

Different polycations with defined fluorescent dyes and variable label degrees were self-synthesized. The overview is presented in Table 3.

Table 3. Overview of synthesized fluorescent-labeled polyelectrolyte

Polyelectrolyte	Dye	Abbreviation	Mw (kDa)	Label Degree*
PAH	Coumarin 343	C343-PAH	15	460
PAH	Rhodamin B	Rho-PAH	15	400

* Label degree defined as the number of monomer units/dye units on the polymer chain (determined by UV/Vis Spectroscopy)

3.2.1 Preparation of C343-PAH

38 mg of PAH was dissolved in 1 mL of HEPES buffer/methanol solution prepared in ratio 3:2. 2.3 mg of Coumarin 343 was dissolved in 550 µL DMSO followed by the addition of 1.6 mg CDI. The activation step was carried out for 1 h at room temperature. Then, the activated dye solution was added to the polymer and stirred for 24 h at room temperature. Afterward, the obtained product was purified by dialysis (Roth, MWCO 8000) for 5 days against water. The extinction coefficient for Coumarin 343 $\varepsilon_{Coumarin343}$ was taken as 44.500 $M^{-1}cm^{-1}$ at 445 nm.

3.2.2 Preparation of Rho-PAH

500 mg of PAH was dissolved in 5 mL ultra-pure water and pH was adjusted to 8.4 with 1 M NaOH. 61 mg of rhodamin-B-isothiocyanate was dissolved in 10 mL DMF and added to the PAH solution. The coupling reaction was carried out on the orbital stirrer for 1h at room temperature. After that, the reaction mixture was diluted with 10 mL ultra-pure water, and pH was adjusted to 8.5. After 24h incubation, the final product was purified by dialysis (Roth, MWCO 8000) for 5 days against water. The extinction coefficient for Rho ε_{Rho} was taken as 100.000$^{-1}cm^{-1}$ at 550 nm.

3.3 Synthesis of biotin-labeled polyelectrolytes

Different polyelectrolytes were covalent coupled with biotin molecules under varied stoichiometric ratios. An overview of self-synthesized biotinylated polymers is given in Table **4**.

Table 4. Overview of self-synthesized biotinylated polyelectrolytes and proteins

Polyelectrolyte/Protein	Mw (kDa)	Biotin derivate	Stoichiometric ratio*
PMAA	100	biotin-hydrazide	50
PMAA	100	biotin-amine	5/10/25/50/100/350/500
PAH	15	biotin-NHS	50

* Defined as the number of monomer/biotin molecules on the polymer chain.

3.3.1 Preparation of Biotin-PMAA by CDI activation

PMAA was covalently coupled with biotin by the mediation of CDI in organic solvent DMSO (Figure 17**)**. 50 mg of PMAA was dissolved in 580 µL DMSO followed by the addition of 32.5 mg CDI. 30 min was allowed for this reaction before 3 mg Biotin-hydrazide was added. The coupling reaction was carried out on the orbital stirrer for 24 hours at room temperature. Afterward, the Biotin-PMAA formed was purified by dialysis (Roth, MWCO 8000) for 5 days against water.
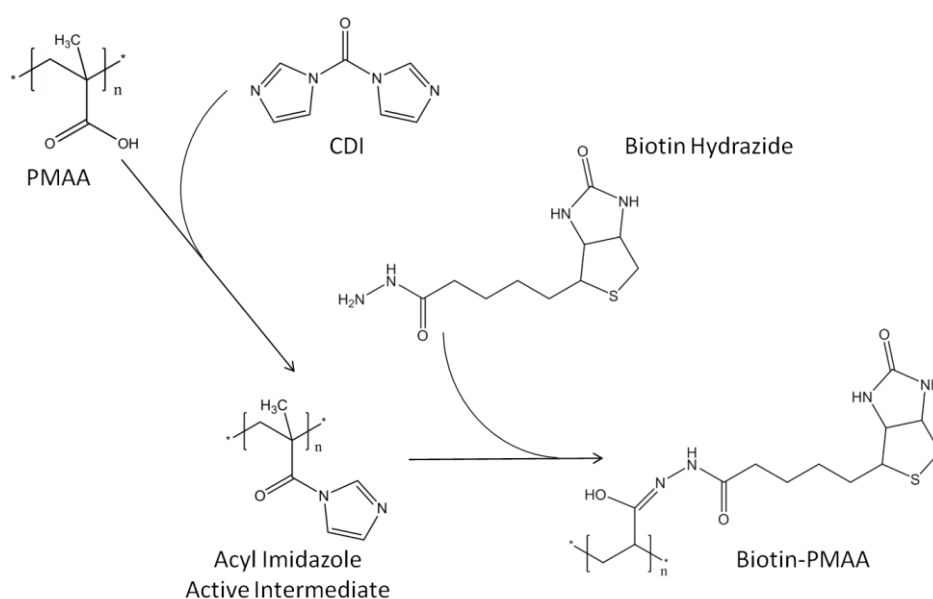
Figure 17. The coupling mechanism of Biotin Hydrazide to PMAA by CDI activation.

3.3.2 Preparation of Biotin-PMAA by EDAC activation

PMAA was covalently coupled with biotin also by the mediation of EDAC/NHS in an aqueous environment (Figure 18). In this method, biotin-NH$_2$ was self-synthesized.

Synthesis of biotin-amine

600 mg of NHS was dissolved in 20 mL DMF. 1,2 mg of DCC has dissolved 10 mL DMF and added to the NHS solution. 1,22 mg of biotin was added NHS-DCC solution and placed on a stirrer for 1h at 75°C. After then, 800µl of 5mM Boc-EDA solution (dissolved in DMF) was added to NHS-activated biotin and placed on a stirrer for 30 min at 75°C. BOC protecting group was removed from biotin-amine by adding 40 mL of DCM and 12 mL of TFA and evaporation in a rotary evaporator. Finally, biotin-amine was washed in 60 mL of MeOH/DME solution (ratio 1:20) and dried in freeze-dryer over 24h.

Coupling biotin-amine with PMAA

350 mg of PMAA was dissolved in 3.5 mL HEPES-Buffer (pH 7.4). 420 mg of EDAC and 122.5 mg of NHS has dissolved 3.5 mL HEPES-Buffer and added to PMAA solution. 1 mL of PMAA-NHS-EDAC solution was added to each of 37.5; 18.8; 10; 5; 2.5; 1.25; 0.7; 0.5 mg of biotin-NH$_2$ to achieve theoretical label degree (biotin unit/PMAA monomer in polymer chain) of 1:5; 1:10, 1:25; 1:50; 1:100; 1:200; 1:350 and 1:500, respectively. The coupling reaction was allowed to stir for 24h at room temperature. Afterward, the PMAA-biotin solution was purified by dialysis (Roth, MWCO 10,000) for 7 days against water. The final product was concentrated under reduced pressure followed by freeze-drying.
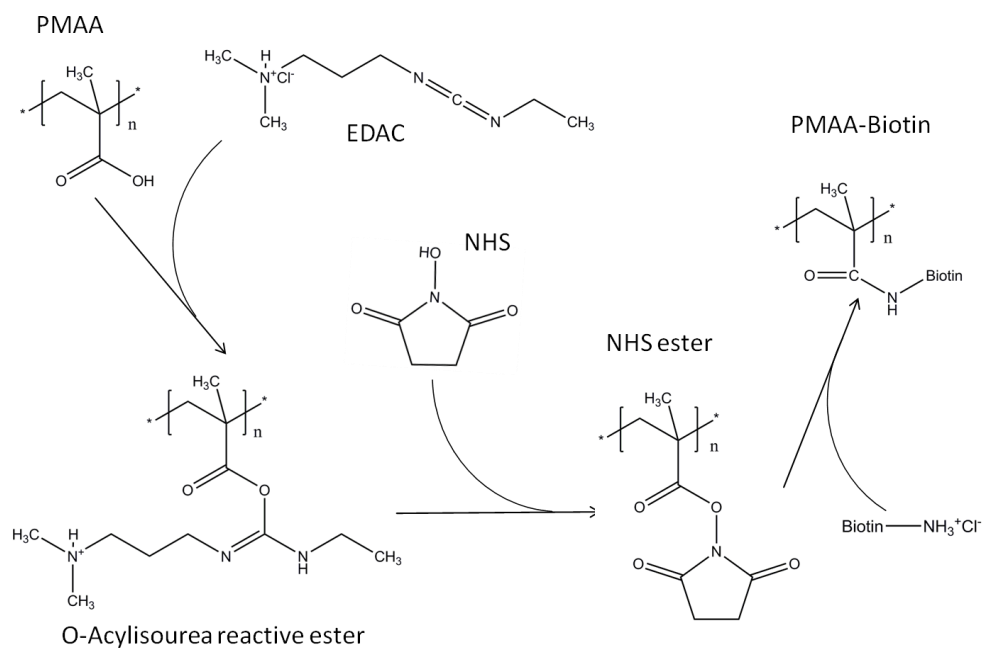
Figure 18. The coupling mechanism of Amine-Biotin to PMAA by EDAC/NHS activation.

3.3.3 Preparation of Biotin-PAH

PAH was covalently coupled with biotin by using reactive NHS-biotin ester (Figure 19). 200 mg PAH was dissolved in 6mL ultra-pure deionized water. 9.4 mg Biotin-NHS was dissolved in 100 µL DMF and added to the polymer solution. The reaction mixture was carried out on the orbital stirrer for 24h at room temperature. The Biotin-PAH formed was purified by dialysis (Roth, MWCO 8000) for 5 days against water.
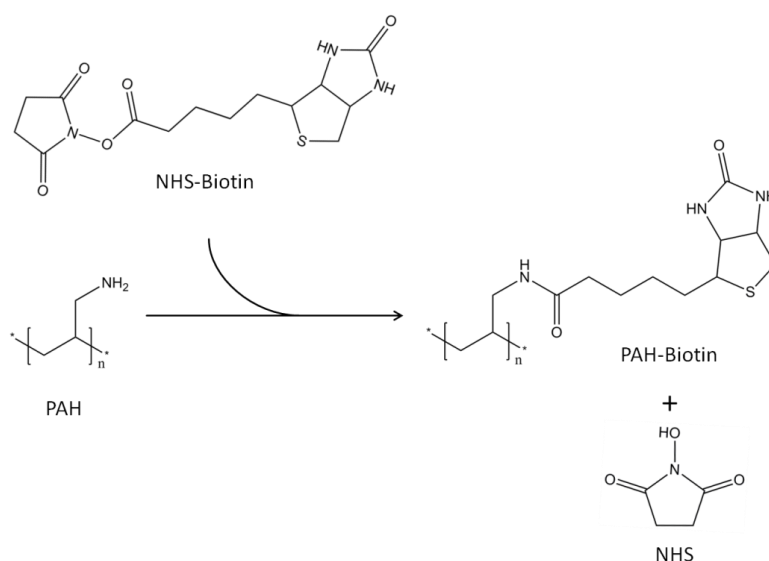
Figure 19. The coupling mechanism of NHS-Biotin to PAH.

3.4 Other sample preparation

3.4.1 Preparation of fluorescent WGM particles utilizing the gradual evaporation method

Plain PS particles of 9.3 µm (Microparticles GmbH) were employed as a template for the preparation of fluorescent WGM beads by the gradual evaporation method.[196] 2 mg of Coumarin 6 was dissolved in 1 mL of chloroform/2-propanol mixture prepared in ratio 1:4; 1:7 and 1:10 (25%, 12.5% and 10% concentration of chloroform, respectively). 20µL of 10% particle suspension was added to organic solvent/alcohol mixture and vortex intensively to obtain a homogenous solution. The dye-doping was carried out at 40°C to evaporate the aromatic solvent phase. After that, the particles were washed three times with 2-propanol and three times with ultra-pure water.

3.4.2 LbL film assembly on WGM particles

LbL film was formed onto particle surface by alternating deposition of negatively charged polyanions and positively charged polycations from solution (1 mg/mL polyelectrolyte, 200 mM NaCl, 50 mM Acetate buffer pH 5.6). The first layer for MF was polyanion while for PMMA, PS and SiO2 particles were polycations. After 20min incubation particles were centrifugated (2 min at 300 g) and washed three times with ultra-pure deionized water to remove the non-adsorbed polyelectrolytes.

3.4.3 Modification of particle surface

3.4.3.1 Sulphonation and nitration

750 mg of fluorescent PS beads were dissolved on an ice bath in 5 mL of concentrated sulfuric acid and 4 mL of nitric acid, respectively. The beads solutions were stirred for 60 min in PTFE sealed flask at 50°C. After that, the beads were washed three times with ultra-pure water, one time with PBS buffer (pH 7.4) and again three times with water.

3.4.3.2 Plasma treatment

200 μL of PS particles (5% aqueous suspension) was placed on the glass slide and left for drying in a vacuum desiccator. Zepto Plasma Laboratory Device (Diener Electronics GmbH) was used as a source of plasma. Glass slide with PS particles was placed in a device chamber and treated with plasma under 10 mbar air pressures for 10 min. Nominal power was set at 50W. Afterward, the particles were gently resuspended in ultra-pure water and coated up to one bilayer of PAH-Rho/PSS under standard LbL coating conditions.

3.4.3.3 Adsorption of EDTA and SDS

2 mg of uncolored PS particles were dissolved in 200 μL ultra-pure water. 146 mg of EDTA or 20 mg of SDS was dissolved in 1 mL ultra-pure water and added to 100 μL particle suspension. The reaction mixture was placed on the orbital stirrer for 20 min to obtain homogenous adsorption. Afterward, the particles were washed three times in ultra-pure water and coated up to one bilayer of PAH-Rho/PSS layers under standard LbL coating conditions.

3.5 Methods

3.5.1 UV-Vis spectroscopy

UV-Vis spectroscopy measures the absorption of light in molecules in the ultraviolet (200-400 nm) and visible (400-700 nm) region of the electromagnetic spectrum. In this spectrum, many organic molecules adsorb photons leading electrons to the transition from the ground state to the excited state (electronic transition). The absorbance is directly proportional to the path length, and the concentration of the adsorbing species, following the Beer-Lambert law:

$$A = -\ln\frac{I}{I_0} = \varepsilon l c \qquad (6)$$

Here A is the measured absorbance, I_0 is the intensity of the incident light at a given wavelength, I is transmitted intensity, l the path-length through the sample, and c the concentration of the absorbing species. For each species and wavelength, ε is a constant known as the molar absorptivity or extinction coefficient[183].

The absorption spectra were recorded by a Cary 50 Scan UV-Vis spectrometer (Varian Inc., USA). Quartz cuvette with a path-length of 1 cm, was used to determine the label degree of fluorescent-labeled polymers as well as biotinylated proteins and polymers (HABA assay).

3.5.2 Fluorescence spectroscopy

Fluorescence spectroscopy is a spectrochemical method of analysis, where the molecules of the analyte are excited by irradiation at a specific wavelength and emit radiation of a different wavelength.

As shown in Figure 20a, when a molecule absorbs the light of appropriate wavelength, their ground electronic state is changing to one of many vibrational levels in one of the excited electronic states. The energy of the electronic transition can be lost either by non-radiative relaxation or by the emission of a photon (fluorescence or phosphorescence). Due to losing some energy through vibrational relaxation and internal conversion, the emitted wavelength is always longer than the excitation wavelength. The difference between the excitation and emission wavelength is called the Stokes shift (Figure 20b).
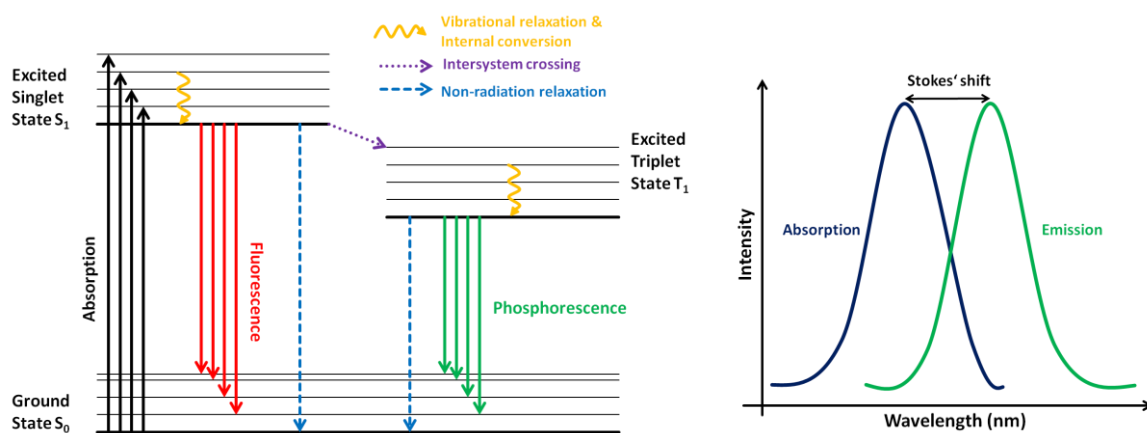
Figure 20 Jablonski diagram illustrated electronic states of molecules and transitions of them, including non-radioactive energy decay processes (left). Simplified representation of the Stokes shift in the electromagnetic spectrum (right).[184]

Typical set-up of spectrofluorometer contains an excitation light source (laser, LED or lamps: xenon arc or mercury vapor lamp), excitation and emission monochromator (usually diffraction grating), sample cell, fluorescence detector and recorder (Figure 21). To avoid interference between transmitted excitation light and emission light, the detector is placing at a 90° angle relative to the excitation light source. Utilizing adjustable optical slits, the excitation and emission bandwidth can be controlled.
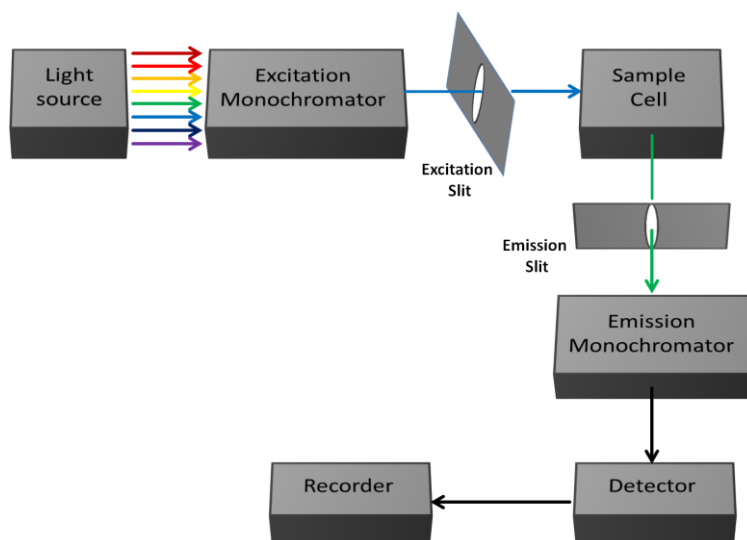
Figure 21. Scheme of the set-up of typical spectrofluorometer.

In the present work, fluorescence was recorded by a Cary Eclipse spectrometer (Varian Inc., USA) for the determination of excitation and emission spectra of dye-doped WGM particles.

The excitation monochromator slit was set with 2.5 nm width, while the emission monochromator slit with 5 nm width. Quartz cuvettes with a path length of 1 cm were used for measurements. Magnetic stirrer of 8 mm length was used to prevent particle sedimentation.

3.5.3 Confocal Laser Scanning Microscopy (CLSM)

Confocal laser scanning microscopy (CLSM) is a fluorescence-based technique for obtaining high-resolution images and three-dimensional reconstructions. The main advantage of CLSM over wide-field fluorescence microscopy is the ability to control depth of measured field, eliminate or significantly reduce the background information away from the focal plane. By measurement and collect serial optical sections from thick specimens, CLSM can build a spatial image of the sample. Placing an aperture (pinhole) in the image plane allows to eliminate out-of-focus light or glare in specimens (enhanced contrast), as well as improve significantly the sectioning (typically 0.5 μm, wide-field microscopy – 2-3 μm). A scheme of the CLSM is shown in Figure 22.
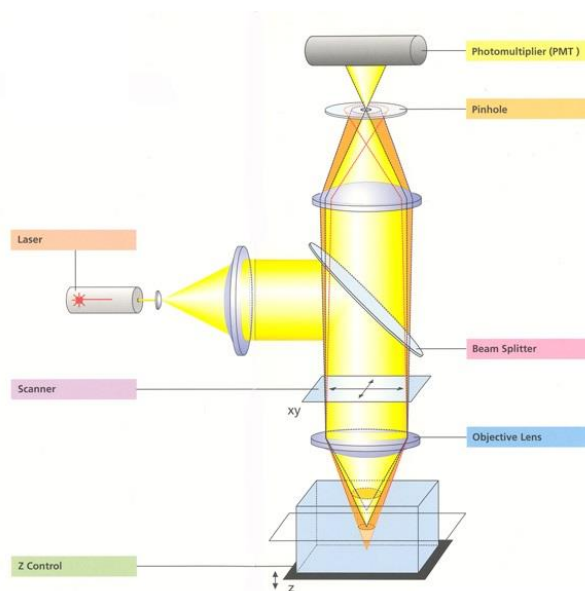
Figure 22. The basic scheme of confocal laser scanning microscopy principle. Adapted from [185].

In the typical confocal laser scanning microscope, laser light is adjusted and brought to a set of scanning multiple mirrors. This approach allows to control the oscillations and tilt the beam in XY directions exact and quick. The laser beam is then guided to the back focal plane of the

objective lens, which focuses it onto a sample. If the sample has a fluorescent marker, part of the fluorescent light is then re-collected by the objective lens and passes through the dichromatic mirror (beam splitter), reflects it away from the laser and toward the detection system. Due to the pinhole aperture, only lights from the focal plane can be directed through to the detector. Detection is realized by a photomultiplier tube (PMT), which amplifies and transforms the signal into an analog electrical one that is further converted to a series of digital numbers and recorded by a computer. 3D imaging is achieved using motorized Z-Stepper, which allows focusing on any focal plane within the sample (resolution > 10nm).

In this work, Leica TCS SP inverted confocal microscope (Leica, Germany) equipped with 63x oil immersion and 10x dry objective was used to obtain information about fluorescence intensity, photostability, relative dye distribution and size of WGM particles. In depending on the fluorophore type, solid-state diode lasers: 405 nm, 534 nm or 635 nm was used as the excitation source. The CLSM images were taken at photomultiplier voltage (PMV) of 800 V.

Quantification of the fluorescence intensity of LbL particles by CLSM was carried out by analysis of the area (Figure 23). The region of interest (ROI) was defined for a minimum of 5 particles, and the mean value was taken as the fluorescence intensity of each particle.

Channel.001	ROI.001	ROI.002	ROI.003	ROI.004
Mean Value	92,34	89,01	91,64	5,36
Sum Processed Pixel	13045 pixel	13446 pixel	13383 pixel	13686 pixel
Pixel Sum	1,210E6	1,210E6	1,2310E6	73332
Length	0	0	0	0
Frame Count	1	1	1	1
Variance	0	0	0	0
Standard Deviation	0	0	0	0
Average Deviation	0	0	0	0
Max Amplitude	92,34	89,01	91,64	5,36
Max Position	1	1	1	1
Min Amplitude	92,34	89,01	91,64	5,36
Min Position	1	1	1	1
Center Of Mass Pos.	1	1	1	1
ROI Area	13053,18 pixel	13458,58 pixel	13399,11 pixel	13694,73 pixel
ROI Area	95,26 µm²	98,22 µm²	97,78 µm²	99,94 µm²

Figure 23. Quantification of the fluorescence intensity by CLSM. (a) Definition of ROI and (b) the table of calculated values. Note that background intensity (ROI.004) should be subtracted from the particle intensity to obtain absolute values.

3.5.4 CPS Disc Centrifuge

The CPS Disc Centrifuge is a high-resolution system for particle size analysis. The operation principle based on centrifugal sedimentation of particles in a density gradient liquid medium.

Settling velocity (or terminal velocity) of the spherical particle in the gravitational field according to Stokes' Law (equation 7), and can be calculated from equation 8.

$$F = 6\pi\eta R v \tag{7}$$

$$v = \frac{2}{9}\frac{(\rho_p - \rho_f)}{\mu}R^2 \tag{8}$$

Here F is a drag force on the interface between spherical particle and fluid R is the radius of a spherical particle, η is the fluid viscosity, v is the velocity of the sphere relative to the fluid, ρ_p is the density of sphere, ρ_f is the density of fluid and μ is the dynamic viscosity. It is worth noting that Stokes' drag increases proportionally to the particle diameter during the terminal velocity as the square of particle diameter.

The schematic view of the CPS Disc Centrifuge principle is shown in Figure 24.
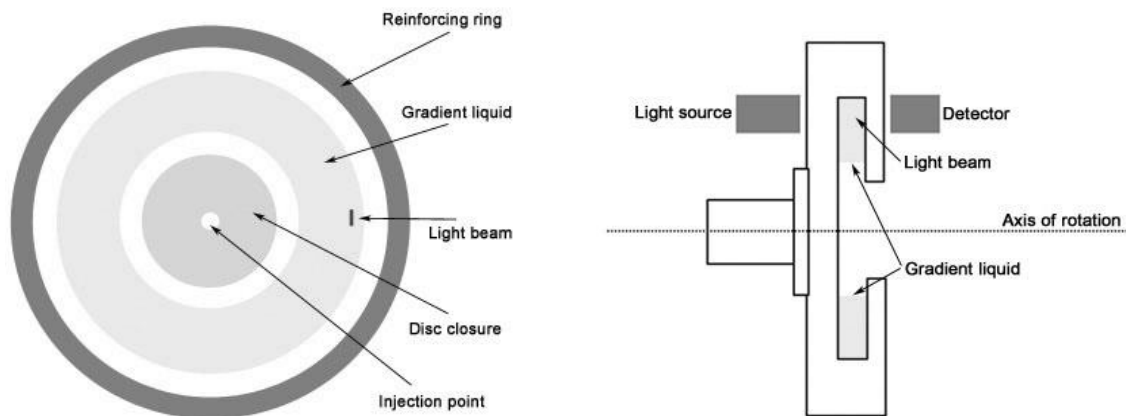
Figure 24. Schematic presentation of the CPS Disc centrifuge principle. Front (left) and cross-section (right) view of the disc. Adapted from [186]

The particles sediment within an optically clear rotating disc. A density gradient of separation media is prepared to stabilize the settling velocity and to obtain a narrow band of particle sizes. When particles approach the outside edge of the rotating disc, block or scatter a portion of a light beam that passes through the disc. The changes in light intensity are continuously recorded and used to determine the size of the particles. By measuring the time needed to reach the detector and compare it with reference particles (with known diameter) the particle

size can be calculated. The CPS Disc Centrifuge allows to analyze particles in the size range between >0,005 µm and <75 µm and separation resolution less as 5% of the diameter.[186]

A CPS Disc Centrifuge DC24000 UHR (CPS Instruments. Inc, USA) was used to evaluate particle size and dispersity. Sucrose water solutions in concentrations from 1% to 9% were used to build a density gradient. For all experiments, the disc rotation speed was set to 24000 RPM.

3.5.5 WhisperSense instrument

3.5.5.1 Basic Set-up

The basic principle of the Low-Q WGM technique was explained in chapter 2. A schematic scheme of Low-Q WGM setup and instrument image used in this work is presented in Figure 25. The instrument WhisperSense was jointly developed by NanoBioAnalytics and Surflay.
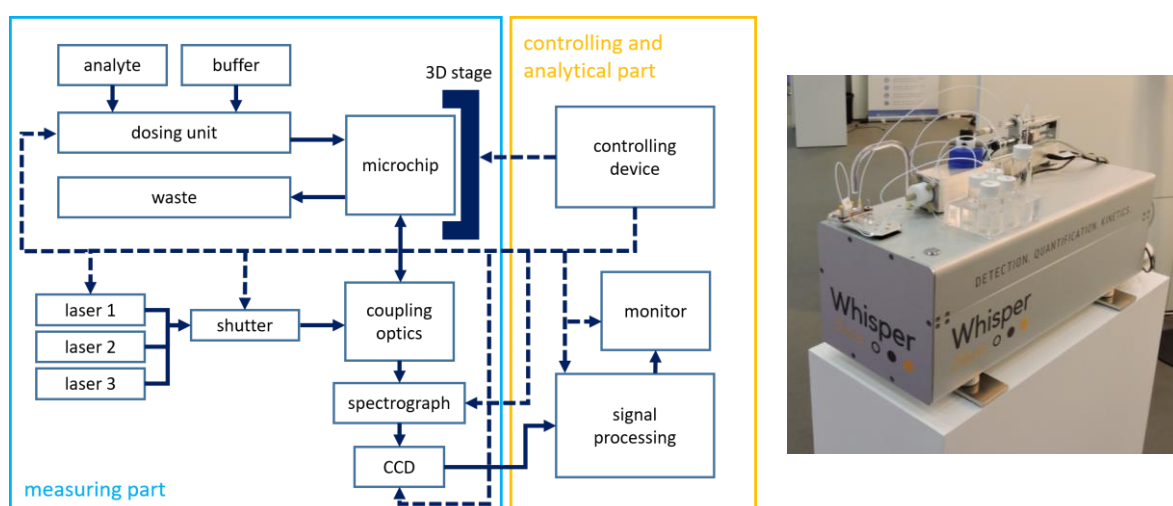
Figure 25. Schematic of the Low-Q WGM biosensing system (left) and WhisperSense device (right)

A dosing unit equipped with a peristaltic pump and some microfluidic valves allows the introduction of WGM sensors and analyte into a microfluidic system. Further, the microchip with fluorescently-labeled microresonators was positioned at the focal point of the objective by applying a 3D motorized stage with a total scan range of 2,25 cm^2 and accuracy of 1 µm. The fluorescence excitation was performed for 1 s by using appropriate laser chosen from three different laser diodes operating at 405, 455 and 532 nm, respectively. Emitted fluorescence was filtered from the excitation light through a dichroic beamsplitter, dispersed onto a spectrograph (focal length = 200 mm) and collected by a CCD-line camera (3600 pixels

and 200 μm^2 pixel size) with an optical resolution of 12 pm. The recorded spectrum was then numerically post-processed, including background correction and peak fitting of the different WGM modes present.

3.5.5.2 Microfluidic chip

The microfluid chip was used to fix the particles and control their position during WGM-measurements. The concept of micro-wells chip developed for this purpose is shown in Figure 26. A microfluidic sticky channel slide with Luer adapters (Ibidi GmbH, Figure 26a) was attached to a micropatterned glass slide (micro resist technology GmbH). The microstructures are patterned into SU-8 photoresist and arranged in regular arrays, as shown in Figure 26b and Figure 26c. The dimensions and geometry of the wells are chosen such that only a single WGM sensor may settle into a well at a time. To obtain the best value between particle sedimentation and analyte-particle surface interactions, three different well shapes, such as cylinders, squares, and stars, have been studied (Figure 26d). Because no significant differences between these three shapes of the well were noticed, in all WGM measurements, the cylinder wells were used.

(a)

(b)

(c)

(d)
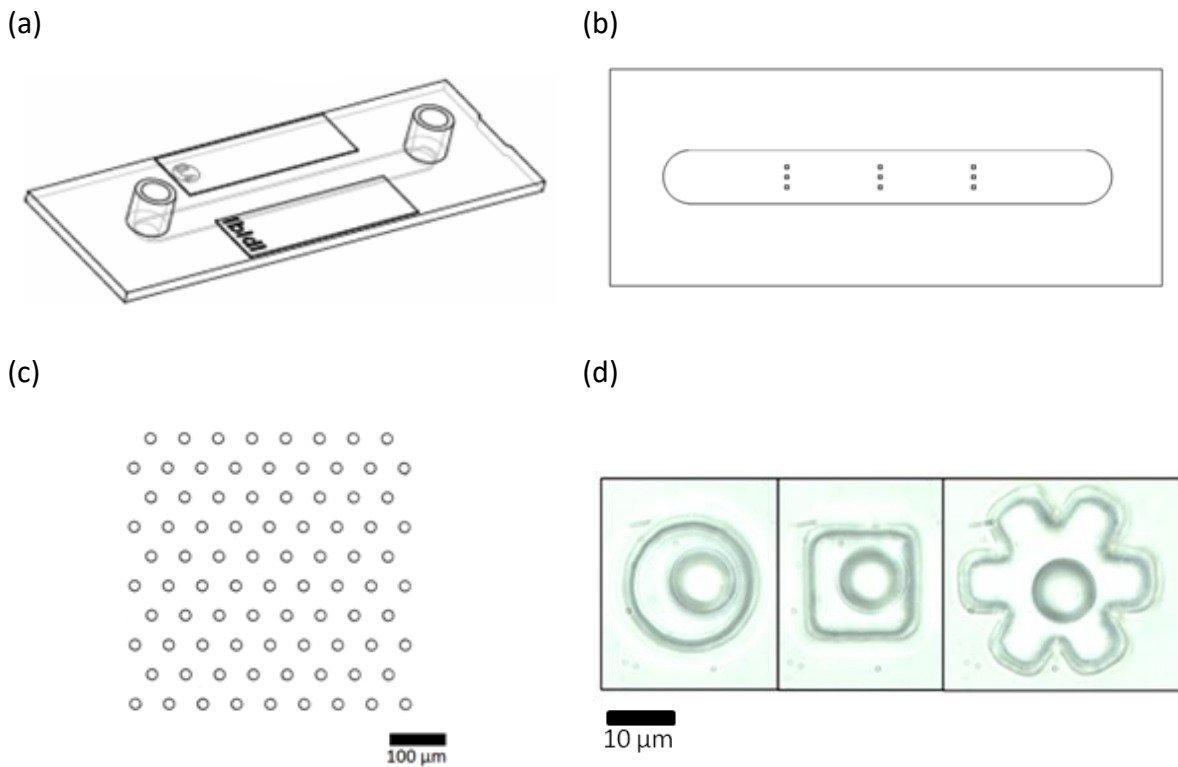
Figure 26. The microfluidic chip developed for the temporary storage of fluorescent WGM sensors. To facilitate connectivity, the mainframe utilizes a Luer lock system (a) and is fixed to a micropatterned glass plate (b). The micropatterns are periodically arranged in square arrays, as shown in (c), each of which contains well features in different geometry (d).

3.5.5.3 Measurement settings and analysis

The WGMs of Low-Q fluorescent particles were obtained by using of WhisperSens 1.0 measurement software (Figure 27a, NanoBioAnalytics GmbH). Particles were measured in a variable exposure time of excitation depending on concentration, distribution, and adsorption coefficient of dye. The nominal acquisition number was set on 3 to reduce the signal noise. By the measurements of adsorption kinetic, the position of WGMs for one particle was collected every 3s. For statistical calculations, a minimum of 10 particles was measured after each step in the measurement. The WGM-shift was calculated by using of WhisperSens analysis software (Figure 27b, NanoBioAnalytics)

(a)
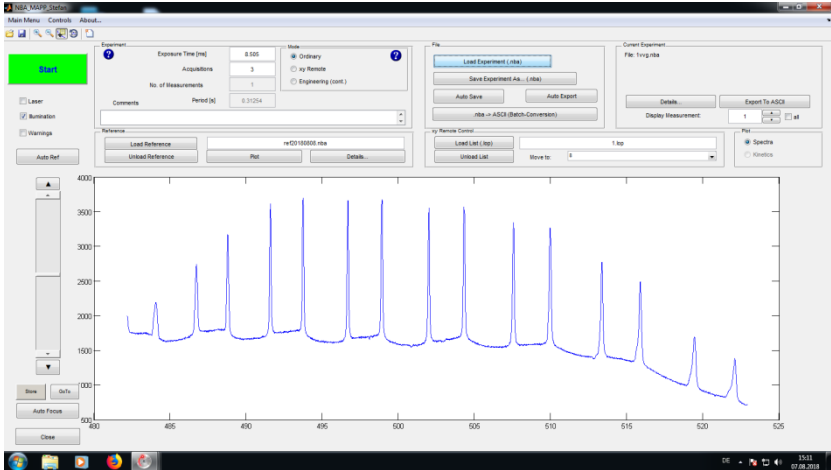
(b)
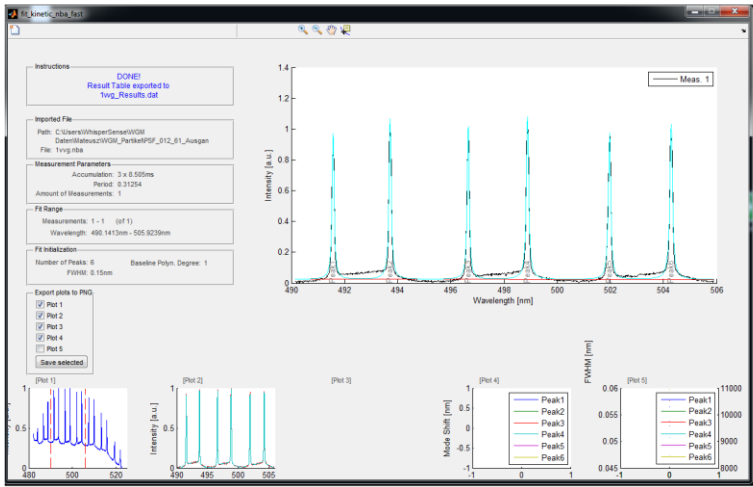
Figure 27. The interface of WhisperSens software packages. The measurement (a) and analysis software (b).

3.5.6 Quartz crystal microbalance (QCM)

The quartz crystal microbalance (QCM) is a high-sensitive technique that utilizes changes in the frequency of acoustic waves in quartz crystal sensors to monitor a mass variation per unit area.[187] The measuring principle of the QCM technique is based on the precise oscillation of the quartz sensors at their resonant frequency when an alternating voltage is applied. In standard configuration, a thin (200-400 μm) circular quartz disc is located between a pair of gold electrodes. When a thin film is deposited or removed from the crystal surface, the frequency is shifted (Figure 28).

The linear relationship between changes of frequency (Δf) and adsorbed/desorbed mass (Δm) is described as the Sauerbrey equation:

$$\Delta f = -\frac{n}{C} \Delta m \qquad (9)$$

Here C is the density of quartz and equals 17.7 Hz ng/cm^2 for a 5 MHz crystal, and n is the harmonic number and equals 1, 3, 5 and 7.
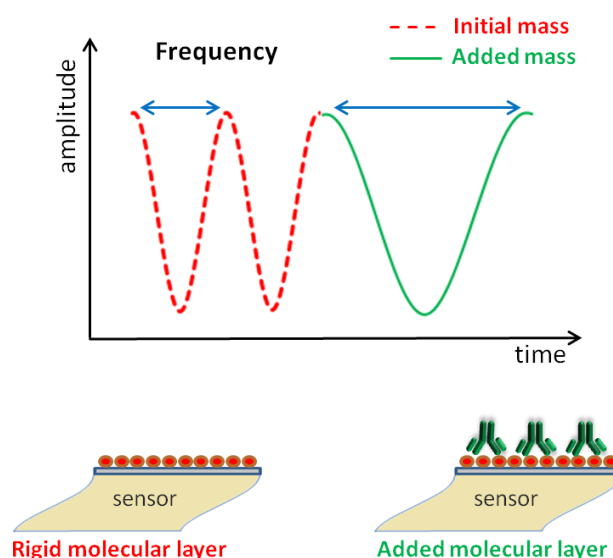
Figure 28. Schematic presentation of QCM technology principle.

In the present work, QCM technology was used to analyze unspecific interactions between lysozyme and LbL-coated WGM particles. QCM measurements were performed using the Q-Sense E4 device from Biolin Scientific (Västra Frölunda, Sweden) at 18°C to minimize the

adverse influence of microbubbles. For calculation of adsorbed mass, results of the frequency changes at the 5th harmonic (25 MHz) were used.

The SiO$_2$ crystals were cleaned in the RCA cleaning solution that consisted of 5:1:1 H$_2$O:NH$_3$: H$_2$O$_2$ at 70°C for 20 min and thoroughly rinsed with deionized water. The measurement cell was cleaned in 2.5% acidic isodecanol solution in an ultrasonic bath at 50°C for 20 min before being rinsed with water and dried with nitrogen. To measure unspecific electrostatic interaction of lysozyme, the QCM crystal was previously coated up to two bilayers of PAH/PSS film. The polymer solution (1mg/mL) was injected into the system with a peristaltic pump for 10 min with a velocity of 40 µL/min and rinsed with a buffer for 10 min before the next polymer solution were added. Lysozyme was dissolved in PBS buffer (pH 7.4) to obtain final concentration of 1000µg/mL (70µM), 100µg/mL (7µM), 10µg/mL (0.7µM), 5µg/mL (0.35µM) and 1µg/mL (0.07µM). In the first experiment lysozyme solutions in the concentration of 1000µg/mL (70µM) (two channels), 100µg/mL (7µM) (one channel) and control sample (PBS buffer, one channel) were injected into the chambers and incubated until the frequency was stabilized. Afterward, the chambers were rinsed with PBS buffer for 20 minutes. In the second experiment, the adsorption of lysozyme in the concentration of 100µg/mL (70 µM) (one channel), 10µg/mL (7 µM) (two channels) and control sample (one channel) were performed. In third experiment the adsorption of lysozyme in concentration of 5 µg/mL (0.35 µM) (two channels), 1µg/mL (0.07 µM) (two channels) were performed. During experiments, the changes in frequency and dissipation were continuously monitored and recorded.

3.5.7 Surface Plasmon Resonance (SPR)

The basic principle of the SPR technique was explained in chapter 2. In order to detect the unspecific binding of lysozyme on an LbL functionalized surface, the Biacore T100 SPR-System (GE-Healthcare) was applied.

The Biacore gold chips were purified for 10 minutes in the Piranha solution (H$_2$SO$_4$/H$_2$O$_2$ in ratio 3:1) and washed six times in deionized ultra-pure water. In the next step, the gold chips were carboxylated using sodium thioglycolate (1mM in ethanol) for 24h gently stirred. Afterward, the gold chips were washed three times in ultra-pure water and placed in a four-channel SPR-chamber. In order to obtain a homogenous, negative charge surface, the gold chips were coated up to two bilayers of PAH/PSS film. The polymer solution (1mg/mL) was

injected into the system with a peristaltic pump for 10 min with a flow rate of 40 µL/min and rinsed with a buffer for 10 min before the next polymer solution were added. The lysozyme adsorption was performed the same as for the QCM experiment.

3.5.8 HABA assay

4'-hydroxyazobenzene-2-carboxylic acid (HABA) was used to quick determination the label-degree of biotinylated PMAA, BSA, casein, and fibrinogen samples. The chemical principle of the HABA assay is shown in Figure 29. In aqueous solution, HABA forms a complex with streptavidin molecules, which has a maximum absorbance at 500 nm. Because biotin has a higher affinity to streptavidin, it displaces the HABA from its complex with streptavidin and the absorbance decreases. The decline of absorbance at 500 nm is proportional to the concentration of biotin.

4,8 mg of HABA was dissolved in 2 mL of 10mM NaOH solution. 0,4 mg of streptavidin was dissolved in 800 µL PBS buffer (pH 7.4) and added to the HABA solution. Biotin-labeled polyelectrolyte/protein samples were prepared in a concentration of 1 mg/mL in ultra-pure water. 5 µL of each biotinylated sample was added to 100 µL of HABA-streptavidin solution, and the absorbance at 500 nm was recorded (PMMA cuvette with 1 cm path length).
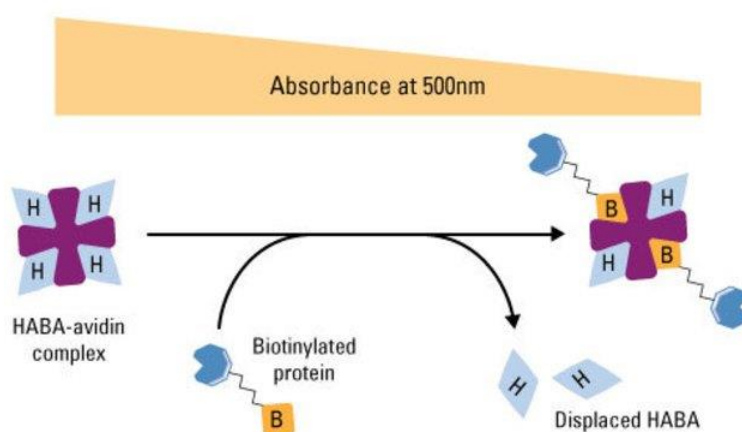
Figure 29. Chemical basis of HABA biotin assay. Adapted from [188].

To calculation the biotinylation-degree of samples, a standard reference curve was prepared. D-Biotin was dissolved in PBS buffer to obtain final concentration of 20 µg/mL, 40 µg/mL, 60

µg/mL, 80 µg/mL and 100 µg/mL. 5 µL of each biotin sample was added to 100 µL of HABA-streptavidin solution, and absorbance at 500 nm was recorded.

3.5.9 Calculations

The diameter and refractive index, for individual particles, were determined by means of the WGM method and using Equation 4b (TM-Mode). The calculations were performed in Matlab software (Matlab Inc. USA). FWHM of TM and TE Modes was provided by WhisperSense analysis software. The surface mass density σ was calculated according to the equation proposed by Himmelhaus:[44]

$$\sigma = \frac{\rho}{3} \frac{(R + \Delta R)^3 - R^3}{R^2} \tag{10}$$

Here, ρ is the mass density of the adsorbate and most proteins can be evaluated to 1.35 g cm^{-1}, and ΔR was calculated from Equation 1. The layer thickness of adsorbate was calculated by using Equation 3.

4 Results and discussion

4.1 Development of fluorescent Low-Q WGM microparticles

As known from fundamentals, many physical properties of optical microresonators such as morphology (including shape, size and surface roughness), density, refractive index or even mechanical strength, affecting their Total Internal Reflection (TIR) conditions and as a consequence the WGM performance. Moreover, the remote coupling mechanism of light based on the excitation of fluorophore molecules incorporated within the resonator matrix, requiring appropriate fluorescent dyes taking into account many dye characteristics such as excitation/emission wavelength, photostability or solubility in solvents. Likewise, dye concentration and distribution can significantly modulate the signal quality and intensity. Finally, one of the most crucial points, but common to all kinds of label-free biosensors, is the surface biofunctionalization. Particles have to be specifically functionalized to detect only the target molecules restricting the non-specific binding of other molecules.

In this part of the thesis, six key aspects in fabrication low-Q WGM microsensors were investigated: a selection of a suitable resonator material type, choice of polymerization method, selection of the resonator size, search for fluorescent dye, determination an optimal dye distribution and choice of surface functionalization methods. Each section was discussed individually with emphasis on their contribution to both the quality of WGMs and sensor performance.

4.1.1 Screening of low-Q WGM microparticle material type

In order to determine the most suitable materials to produce fluorescent Low-Q WGM sensors, five spherical microparticle types were investigated: polystyrene (PS), melamine-formaldehyde (MF), poly(methylmethacrylate (PMMA), borosilicate glass (BG) and silica (SiO_2)

with refractive indices (RI) of 1.55, 1.52, 1.48, 1.52 and 1.42, respectively and diameter range between 8 – 10 µm for all five types. Table 5 shows selected physical and chemical properties of investigated microparticles.

Table 5. Selected physical and chemical properties of different particles used as Low-Q WGM microresonators. Reprinted from [189].

Properties	PS	MF	PMMA	SiO$_2$	BS
Density (g/cm^3)	1,05	1,51	1,19	1,85	2,54
Refractive Index	1,55	1,52	1,48	1,42	1,52
Surface charge	anionic	cationic (anionic >pH 7)	anionic	anionic	anionic
Crosslinking	non-crosslinked/ crosslinked	crosslinked	crosslinked	crosslinked	crosslinked
Temperature stability	100 °C	250 °C	100 °C	1000 °C	900 °C
Stability in solvents	water, low alcohols	water, alcohols, solvents, and oils	water, DMSO, aliphatic hydrocarbons	water, alcohols, solvents, and oils	water, alcohols, solvents, and oils
Hydrophilicity/ Hydrophobicity	hydrophobic	hydrophilic	hydrophobic	hydrophilic	hydrophilic
Mechanical strength	robust	robust	robust	robust	robust

As can be seen, MF, SiO$_2$, and BS microparticles are characterized by strong hydrophilic, charged surfaces, and high stability against different solvents. These properties can facilitate their decoration with complex biological or chemical molecules, including antibodies, DNA/RNA or viruses, while the remaining particle area can stay resistant to non-specific binding. In contrast, PS and PMAA particles exhibit hydrophobic surfaces and stability only in water or low alcohol. That significantly lower their capabilities of biofunctionalization requiring more innovative strategies as well as additional passivation steps in order to reduce non-specific binding. However, choosing the most appropriate material to produce low-Q-WGM microparticles mostly depends on its resonance performance and WGMs quality.

Therefore, in the next step, the WGM spectra of selected microparticle materials were analyzed. In order to immobilize the fluorescent dye onto non-colored microparticles, the Layer-by-Layer (LbL) technique was applied. This novel method for the preparation of fluorescent Low-Q WGM microsensor has been already published[190] and will be in detail described in chapter 4.1.6.

Each type of particle was coated up to 6 bilayers of coumarin-343-labeled poly(allylamine hydrochloride) (PAH) and unlabelled poly(sodium-4-styrenesulfate) (PSS). The WGM spectra were obtained in water by excitation at 405 nm (Figure 30).
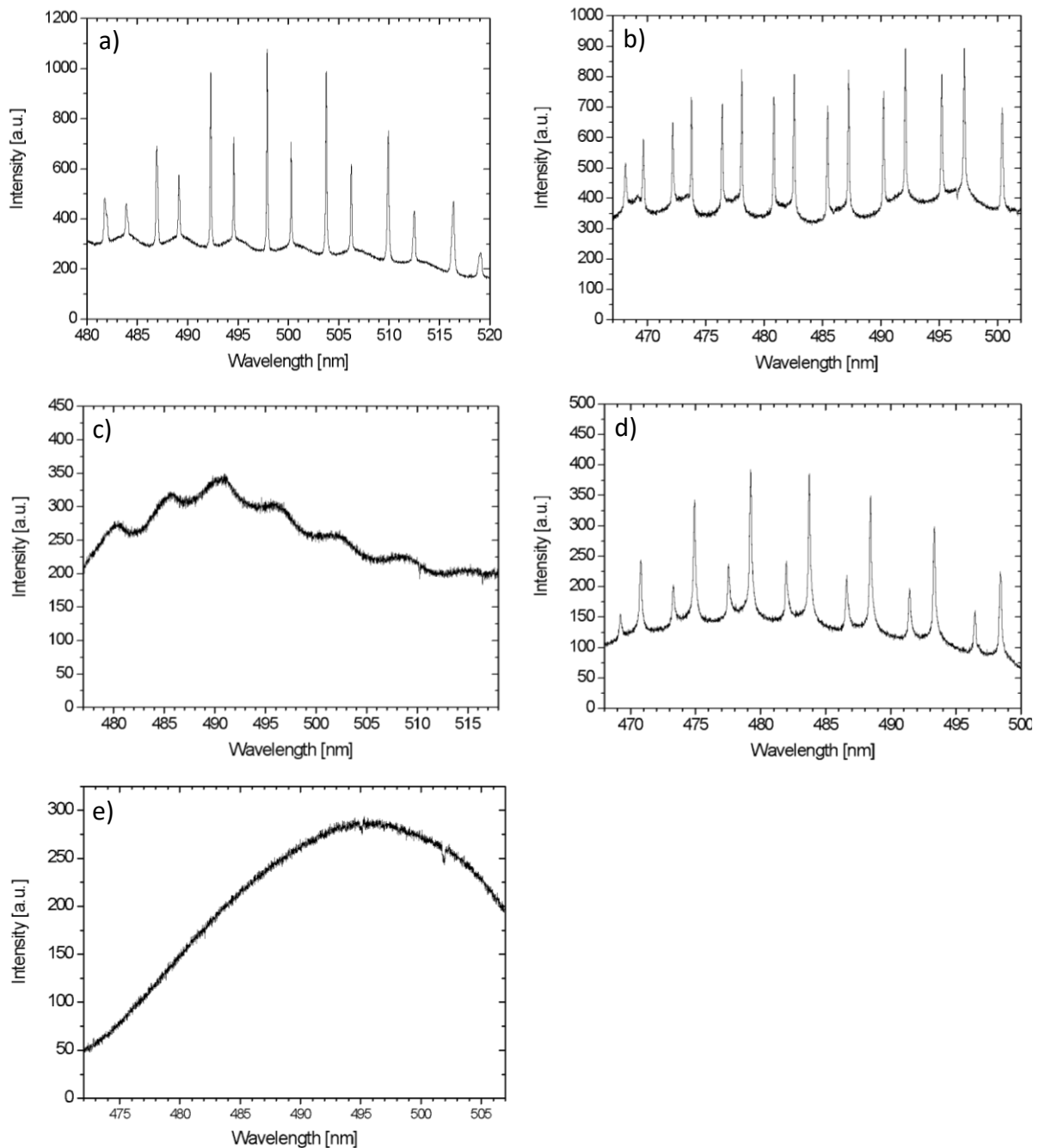
Figure 30. WGM spectra of different microparticle materials coated up to six bilayers of PAH-C343/PSS (a) Polystyrene (PS) beads; diameter 9.3 µm. (b) Melamine formaldehyde (MF) beads; diameter 8.8 µm. (c) Poly (methyl methacrylate) (PMMA) beads; diameter 10.7 µm. (d) Borosilicate glass (BS) beads; diameter 10 µm. (e) Silica beads; diameter 7.6 µm.

The best spectra, characterized by intensity and narrow FWHM of WGMs, were observed for PS particles. MF and BG particles yield already higher FWHM and lower intensity, as well as

more side peaks in the case of MF. At PMMA and SiO$_2$ particles, almost none WGM signals could be detected which corresponds with their lowest RIs. Although in literature and patents MF particles are described as optimal material due to the apparently highest refractive index of the five particle types, they exhibit surprisingly weaker WGM performance than PS particles.[56,57] In order to find the reason for this divergence the real refractive index and surface roughness of microparticles were determined and correlated with their WGM performance.

4.1.1.2 Effect of microresonator's RI on WGM performance

Since the refractive indices of microparticles were taken from bulk material[189], the real RI of the microparticles were precisely determined for transverse magnetic WGM modes (TM modes) using the Airy approximations. The WGM spectra obtained for dye-doped MF and PS particles, as well as fluorescent LbL, coated PS, MF, PMMA, BG, and SiO$_2$ particles were first fitted by means of Voigt profile and then evaluated according to equation 2b implemented into a numerical algorithm.[44,49-51]

Table 6 shows the determined RI value of the different microparticles. The LbL-fluorescent coated colorless PS, and MF particles show a subtly smaller RI than their dyed-doped counterparts. As reported, this difference is caused by the presence of LbL coating, which has a lower refractive index (1.47) than native PS or MF particles and thus contributes to their effective RI.[49]

Table 6. Refractive index of WGM beads

Particle material	RI of bulk material (uncolored)	RI determined by WGM (dye-doped/LbL coated)
Polystyrene (PS)	1,59[a]	1,56/1,55
Melamine formaldehyde (MF)	1,68[a]	1,53/1,52
Poly(methyl methacrylate) PMMA	1,48[a]	data not available
Silica (SiO$_2$)	1,42[a]	data not available
Borosilicate glass (BS)	1,55[b]	/1,52

[a] Data obtained from *Microparticles GmbH*
[b] Data obtained from *Polysciences Inc.*

Moreover, in contrast to PS particles was found that the RI of MF particles is significantly lower than that of bulk MF as discussed above. The reason can be arranged for the fabrication method employed in producing MF particles. Bulk melamine resin as a versatile thermosetting material is fabricated at higher temperatures and under optimized reaction conditions (water-free) resulting in a high crosslinking degree. In contrast, MF beads are prepared via polycondensation of melamine and formaldehyde in the presence of acid as catalyst in aqueous solution. As described in the literature[191] the polycondensation yields in a first step polymer-resin nanoclusters of 7-10 nm in diameter. In a subsequent step, these structures aggregate and crosslink together, forming stiff and interconnected microspheres. This process leads obviously to less dense structures than in bulk and in consequence to a significantly lower refractive index of the microparticles. The lower RI compared to PS explains the weaker WGM signals of MF particles and throw a shadow on assumptions in former studies and patents proposing MF particles as the best WGM sensors based on the RI values of bulk material.[56,57]

Insofar from viewpoint of refractive index, the PS particles are the most suitable material. Attempts to modify the particles with materials of a higher refractive index like polyvinyl carbazole failed up to now due to worse particle quality.

4.1.1.3 Effect of microresonator surface roughness on WGM performance

Besides the real RI of particles, the FWHM of WGMs is also affected by the surface roughness due to higher losses of resonance modes by light scattering. To gain a better understanding of these effects, non-coated WGM sensor beads of PS, MF, PMMA, and BG were investigated by Scanning Electron Microscopy (SEM, Figure 31) and Atomic Force Microscopy (AFM, Figure 32).

The SEM images show that only PS beads have a homogenous and smooth surface (Figure 31a). As recognizable in the magnified inset of Figure 31b, MF particles exhibit small pores, which support the proposed formation process of aggregating melamine-formaldehyde nanoclusters as described above and their remarkably lower RI. The rougher surface of MF beads leads to increasing losses of circulating WGMs due to scattering and lowers the resonator quality. BG and PMMA beads show an inhomogeneous surface with clumps of synthesis rests on it (Figure 31c, d). These physical imperfections lower the resonator quality

of BG and PMMA particles further and explain the weaker WGM performance of BG than MF despite comparable RIs.
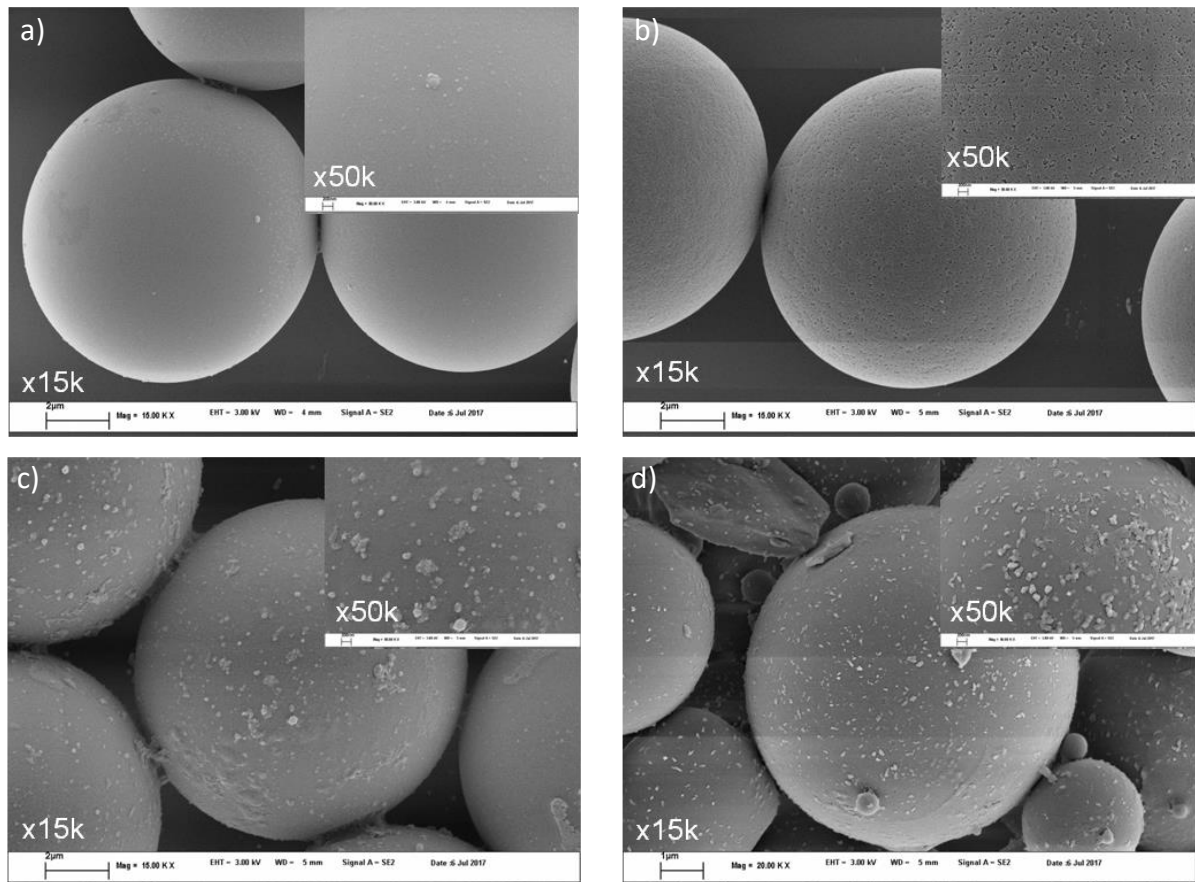
Figure 31. SEM images obtained for different microparticle materials. (a) PS, (b) MF, (c) BS, (d) PMMA. The images were performed by H. Runge from Max Planck Institute for Colloids and Interfaces, Potsdam.
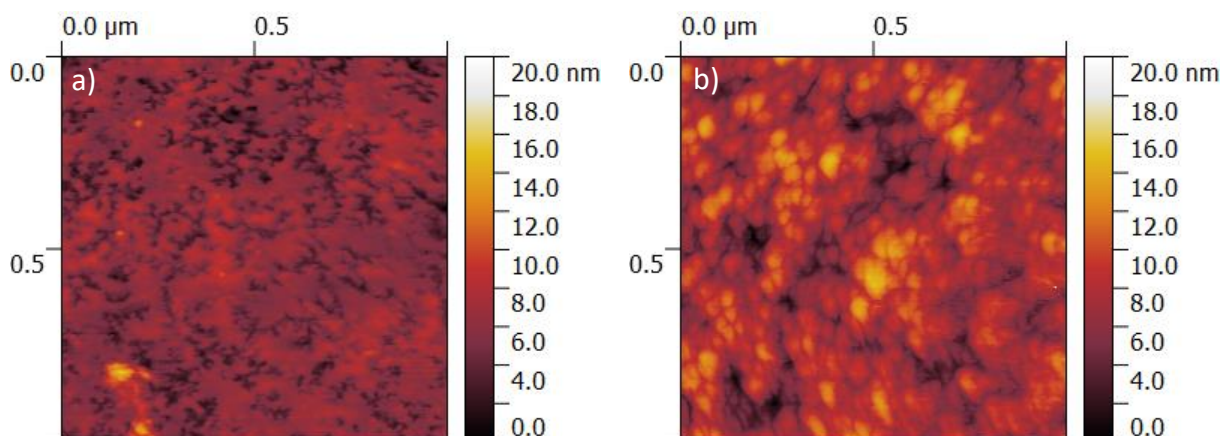
Figure 32. The surface roughness of PS (a) and MF (b) beads measured by Atomic Force Microscopy. The images were performed by Cagri Üzüm from Surflay Nanotec GmbH, Berlin.

The differences in surface roughness of PS and MF particles shown by SEM were confirmed by high-resolution AFM investigations (Figure 32). In accord with the SEM results, MF beads exhibit notably higher roughness than PS beads.

A further problem of WGM beads could arise from deviations of ideal spherical shape. Slight ellipticity would result in Higher Order Modes (HOMs) observable as weak side peaks in the WGM spectra. Such peaks are often observed in WGM spectra of MF particles, as slightly visible in Figure 30b[97], but were also observed at larger PS beads (> 15 µm). The connection between sphericity and side peaks could not be approved, because there is no alternative method known to investigate such small deviations from sphericity.

From the viewpoint of surface roughness and sphericity, the PS particles are also the first choice of material.

4.1.2 Effect of the polymerization method

The polymerization process can influence many physical properties of particles such as morphology, porosity, elasticity, or partially also the surface roughness.[192] These properties are particularly crucial for WGM particles because they can directly affect their resonance and sensing performances. An appropriate polymerization method and polymerization parameters can diminish the particle size dispersity, facilitating their implementation into micropatterned microfluidic chip and standardization of the WGM-shift magnitude.

As described previously, MF particles are usually synthesized via the polycondensation process of melamine and formaldehyde in acidic conditions and high temperatures. PS particles, in contrast, can be prepared using several polymerization methods such as conventional dispersion and emulsion polymerization, suspension polymerization or seeded-growth polymerization. To gain a better overview, and the potential impact on WGMs performance, a brief description of each polymerization method will be presented below.

Dispersion polymerization

Dispersion polymerization is the simplest fabrication method of polymer particles, occurring in the single phase. The reaction begins in a homogenous mixture of monomers, free-radical initiator, and stabilizer dissolved in an organic solvent.[193] The polymer chain grows up in the solution until it reaches a critical size at which precipitates as nano-scale particles. These tiny particles aggregate into larger particles in a few nanometer sizes, and the next step continues

to grow by polymerization of monomers inside the particles or/and by capturing smaller nucleated particles. This approach allows achieving particles in size range of 1-20 μm, however in relatively wide size distribution.

Emulsion polymerization

The second polymerization method is emulsion polymerization. In contrast to dispersion polymerization, this approach is carrying out in two phase's solution. The organic phase contains monomers is emulsified, e.g., by sonication into continuous water phase in the presence of initiator and surfactant. Anionic stabilizers are typically used to prevent aggregation by forming an amphiphilic layer onto organic solvent droplets with entrapped monomers and initiators. After increasing the temperature free-radical oligomers are formed and diffused into the organic droplets to initialize the polymerization process. Generally, the emulsion polymerization method allows obtaining particles in size range of 50-500 nm in narrow size distribution or micrometer size range but rather polydisperse.[194]

Seeded-growth polymerization

The third approach in the preparation of low-Q WGM polystyrene particles is the seeded-growth polymerization. This method is characterized by using micron-sized, seed PS particles (usually prepared by dispersion polymerization) and a swelling agent with low solubility in water, e.g., styrene-monomers solution. Due to the swelling process, the monomers and initiator can diffuse into the seed particle matrix, and polymerize lead to the particle growth. The final diameter of particles can be precise control by the selection of seed particle size and reaction time. Mostly, seeded-growth polymerization allows preparing narrow size distributed particles in the range of few nanometers to thousands of micrometers.[195]

In order to find out an optimal polymerization method, PS particles prepared by dispersion-, emulsion-, and seeded-growth polymerization (Surflay Nanotec GmbH) were investigated. The results were divided into two parts. First, the size distribution and morphology of different PS particle batches were analyzed by confocal laser scanning microscopy (CLSM) and CPS disc centrifuge (Figure 33 and Figure 34, respectively). In the second part, the WGM performance (mode's quality, intensity, and bandwidth) was determined in the WGM instrument (Figure 35).

As expected, PS particles prepared by dispersion and emulsion polymerization show a broad size distribution (Figure 33a, b, and Figure 34a, b). In dispersion polymerization, the growing process of particles is determined by spontaneous diffusion of monomers/oligomers into

newly created nano-scale particles. Because the polymerization starts regardless of nanoparticle size and cannot be precisely controlled, particles grow uneven. In contrast, particles prepared via seeded-growth polymerization rise up simultaneously from seeds in the same size, therefore show uniform size.
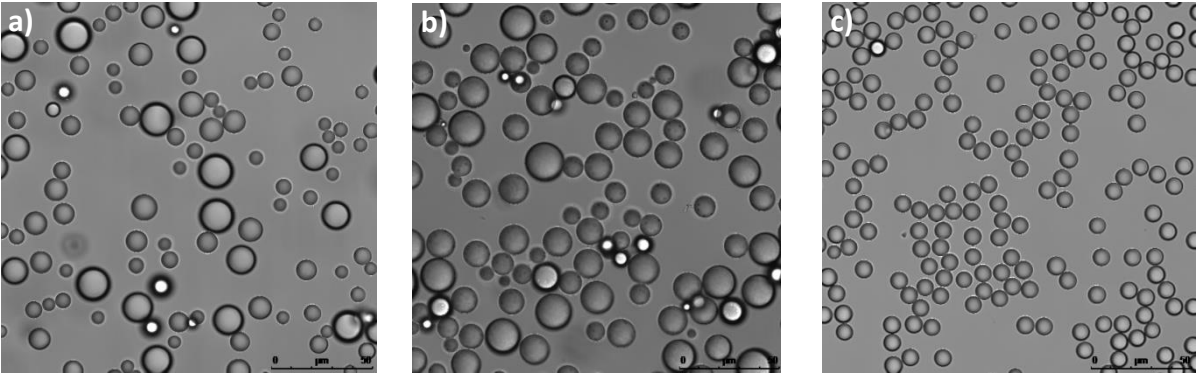
Figure 33. CLSM images of PS particles synthesized by different polymerization methods. (a) Dispersion polymerization, (b) emulsion polymerization, (c) seeded-growth polymerization.
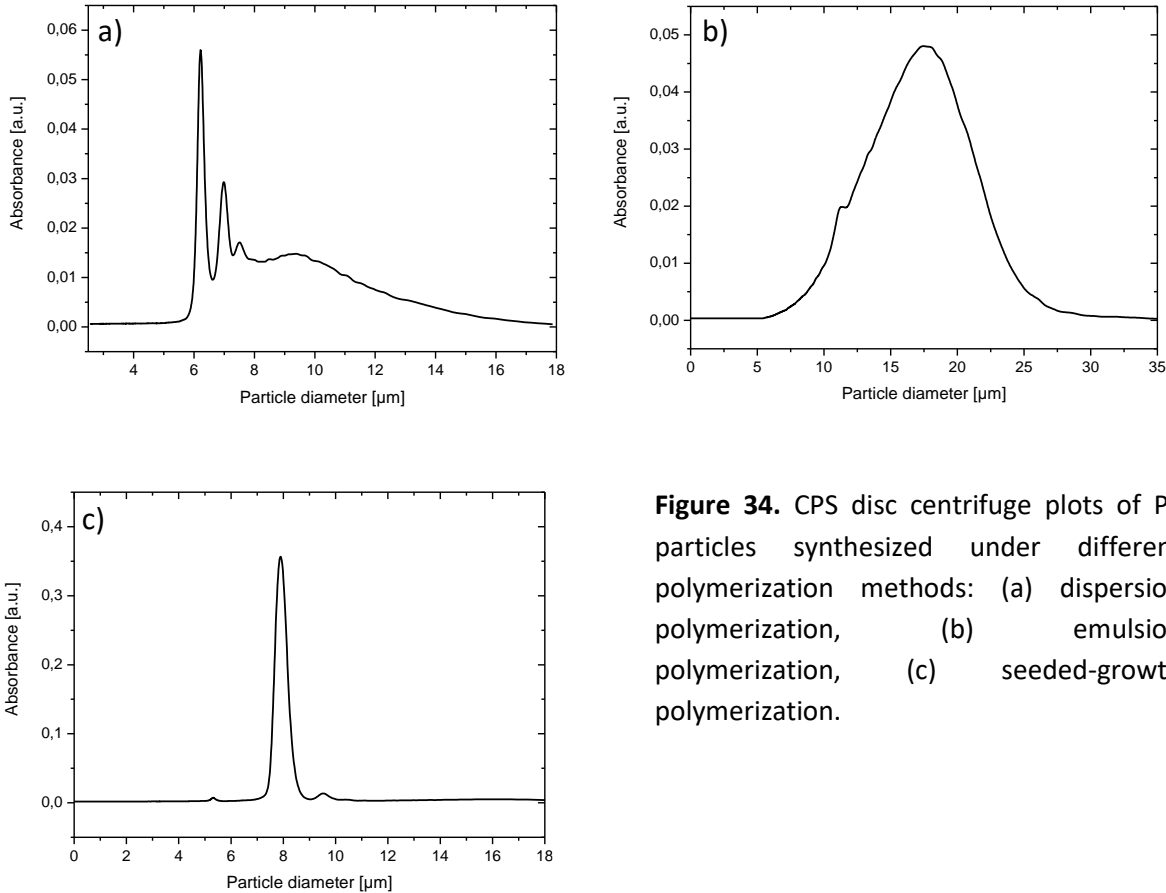
Figure 34. CPS disc centrifuge plots of PS particles synthesized under different polymerization methods: (a) dispersion polymerization, (b) emulsion polymerization, (c) seeded-growth polymerization.

By analyzing the WGM performance, it can be seen that particles prepared via emulsion polymerization exhibit significantly lower WGM intensity and broader bandwidth than particles prepared via dispersion or seeded-growth polymerization (Figure 35a-c). The worse spectra of emulsion beads are probably correlated with required harsh polymerization conditions (for example a high rotation speed to achieve homogeneous emulsion) or high tension in the particles caused by the fast reaction and local production of heat during the exothermic polymerization. Thereby, the particles can form a none-ideal spherical structure, thus contributing to higher losses of circulating light and broader WGM peaks.
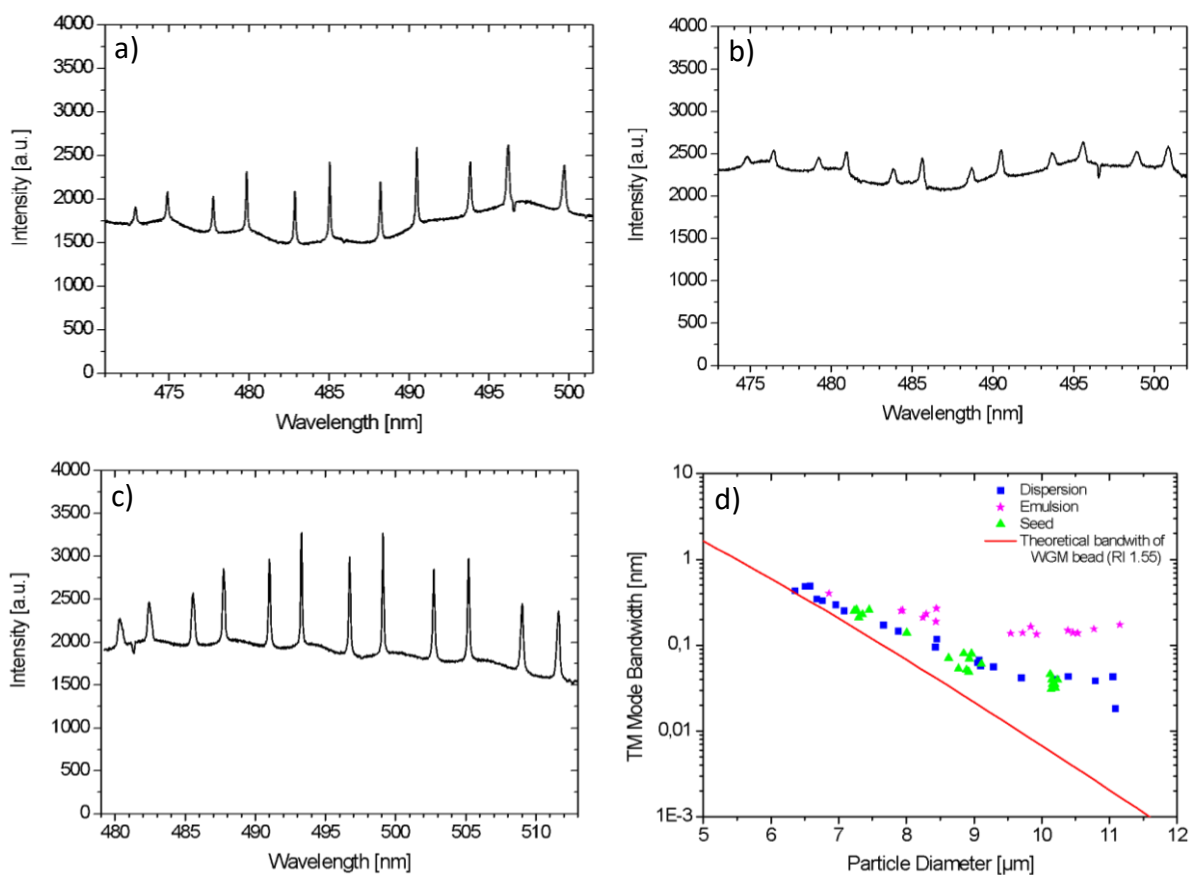
Figure 35 WGM spectra of PS particles synthesized under different polymerization methods: dispersion polymerization (a), emulsion polymerization (b), seeded-growth polymerization (c). TM-Mode bandwidth as a function of particle diameter (d).

A detailed analysis of mode bandwidth (TM-mode) plotted in a function of particle diameter (Figure 35) confirmed the above results. The minimum bandwidth FWHM of particles (size range 10-11 µm) prepared by dispersion and seeded-growth polymerization was 0.04-0.05 nm whereas for particles prepared by emulsion polymerization was 0.2 nm.

4.1.3 Selection of resonator size

Since the WGMs bandwidth (FWHM) and the magnitude of wavelength shift are determined mainly by the resonator diameter, a selection of the most suitable resonator's size is one of the critical points in the fabrication of low-Q WGM sensors.

As discussed already in chapter 2.1.1.1, small particles offer several advantages over large particles due to higher relative mode shift, less molecule consumption for sensor coverage, the possibility of incorporation in cavities down to cell size or even below[97] and larger free spectral range of modes. Especially this last feature is desired since it enables the detection of a group of individual mode position, giving precise information about the resonator dimension.[44] According to mathematical calculations presented by Bichler *et al.,*[50] the smallest resonator's diameter with an acceptable upper limit of modes FWHM = 0.1 nm can be estimated for around 8 μm in case of PS beads (calculated for a mode wavelength of λ_m = 500 nm and aqueous environment). Taking the bulk refractive index of MF particles a size down to around 5 μm should be possible. As presented in this work and already reported,[190] the real RI of MF particle is significantly lower (1.53) than that of the bulk MF. Hence, the smallest resonator's diameter where the WGMs could be detected could be similar for PS and MF particles.

Although for smaller particles larger shifts are expected, they present less-defined (broader) modes which make the exact analysis of mode position more inaccurate. Besides the broadening, the number of modes decreases remarkably and reduces the option to evaluate several modes. Due to higher curvature, more photons hit the particle surface an angle above the critical angle of TIR, contributing to the lower intensity of WGMs and lower signal/noise ratio. Based on these arguments, the choice of the optimal particles is not a simple matter, requires a more in-depth analysis and depends in addition on the particle handling and the mathematics of signal evaluation.

To find out a suitable resonator's diameter for the low-Q WGM sensing system, PS particles in size range from 6.3-13.5 μm and MF particles in size range from 4-11.5 μm were investigated. Figure 36 and Figure 37 show typical WGM spectra of microparticles (MF and PS, respectively) independence on their diameter. As it was supposed, increasing the particle diameter leads to enhancing the WGMs quality (sharper peaks) and reducing the spectrum noise, which facilitates the analysis of mode positions. Most interestingly, however, for both particle types with diameter >11 μm some additional side peaks, called Higher Order Modes (HOMs), in the

WGM spectra are observed. As explained previously, HOMs result from the deviations of an ideal spherical shape of resonators and corresponds to the higher number of field maxima along the radial direction. Besides the HOMs, deterioration of the WGMs quality can also be caused by shortens the free spectral range and increasing the full number of wavelengths that fit into the sphere's circumference. Hence, the WGMs in the higher circumference of the particle can overlap each other, creating less defined peaks finally. On the other side, particles with a diameter below 7 μm, present significantly broader WGMs and higher free spectral range so that the accurate analysis of modes position and particle diameter becomes remarkably impeded.
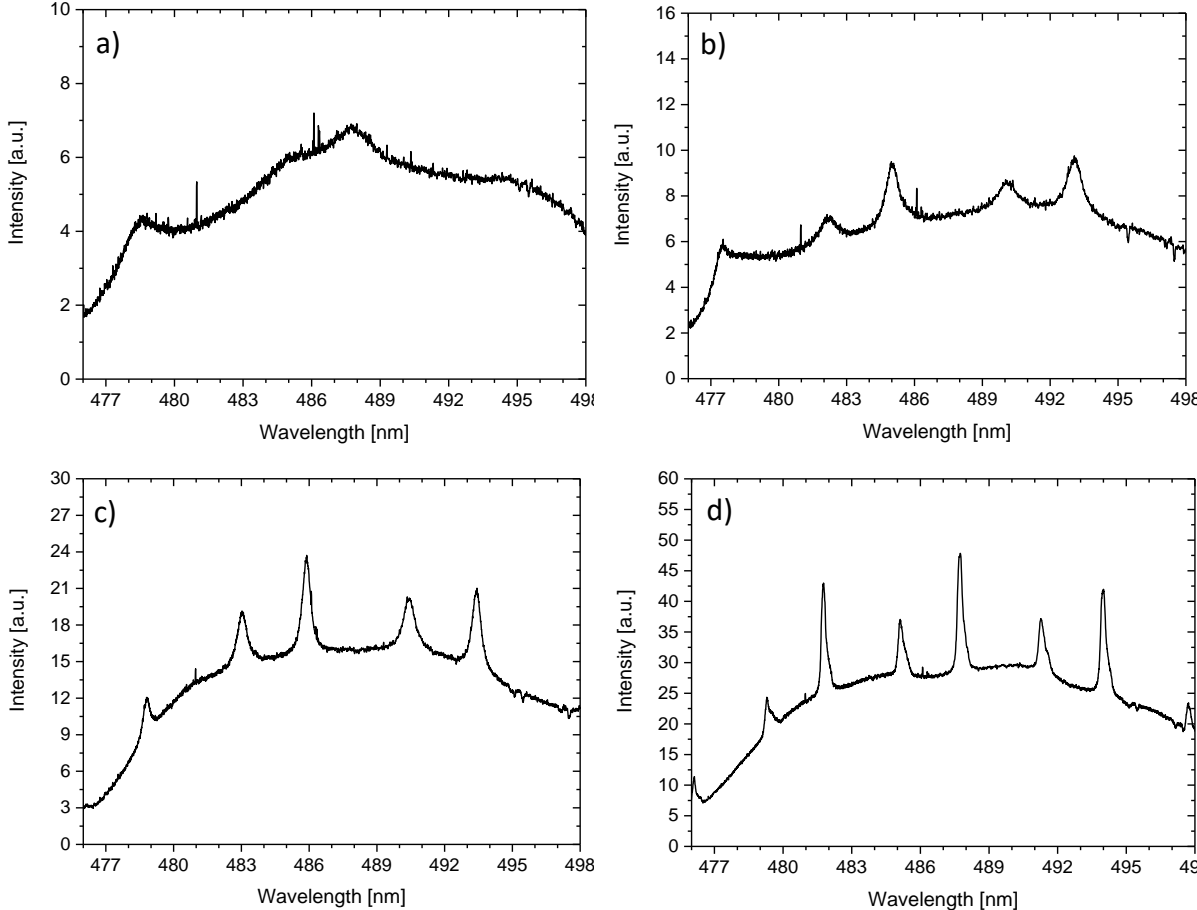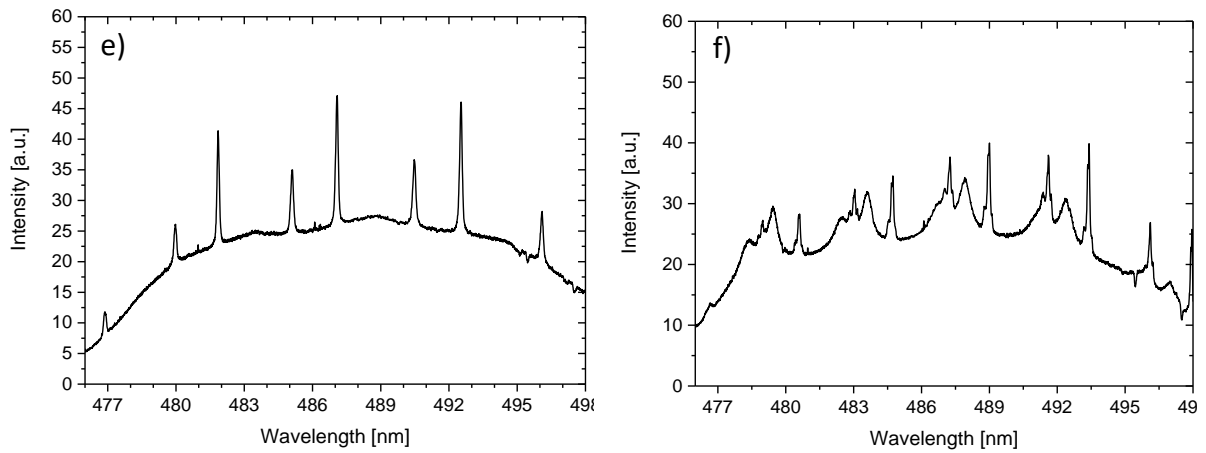
Figure 36. WGM spectra of MF particles in different diameter: 4 µm (a), 5.5 µm (b), 7 µm (c), 8 µm (d), 9.5 µm (e) and 11.5 µm (f).

74
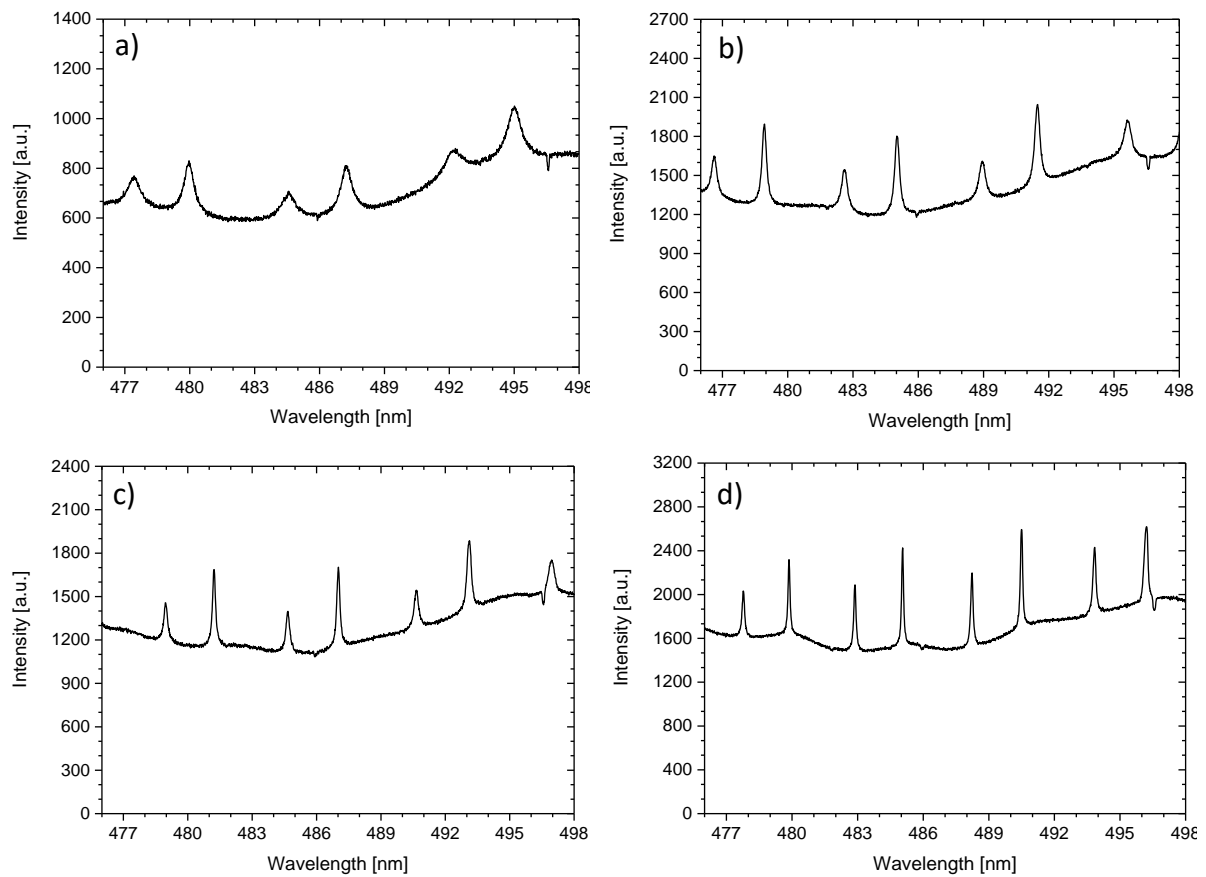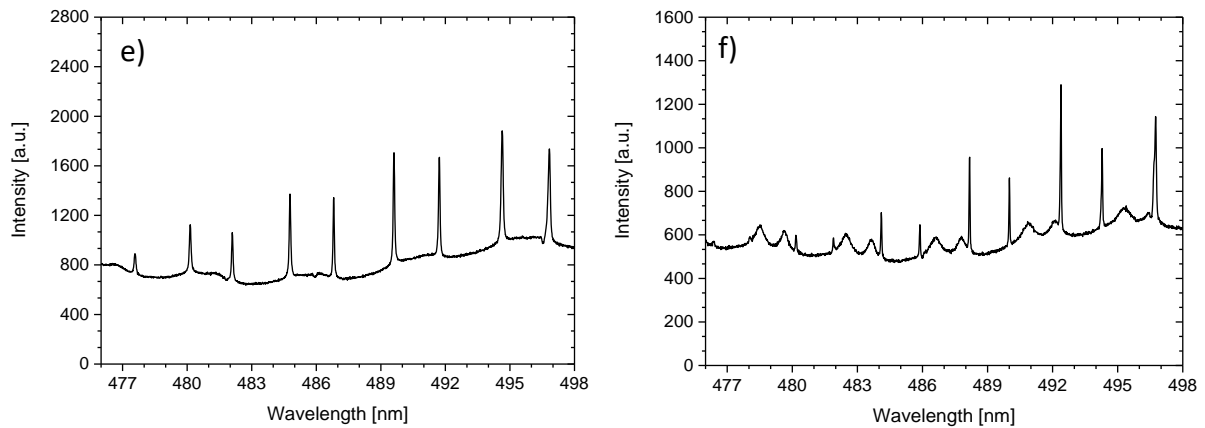
Figure 37. WGM spectra of PS particles in different diameter: 6.3 μm (a), 7.8 μm (b), 8.5 μm (c), 9.5 μm (d), 10.8 μm (e) and 13.5 μm (f).

To provide more precise information about the WGM performance of PS and MF particles, the FWHM of the modes and the free spectral range (distance between subsequent modes) was determined (Figure 38).
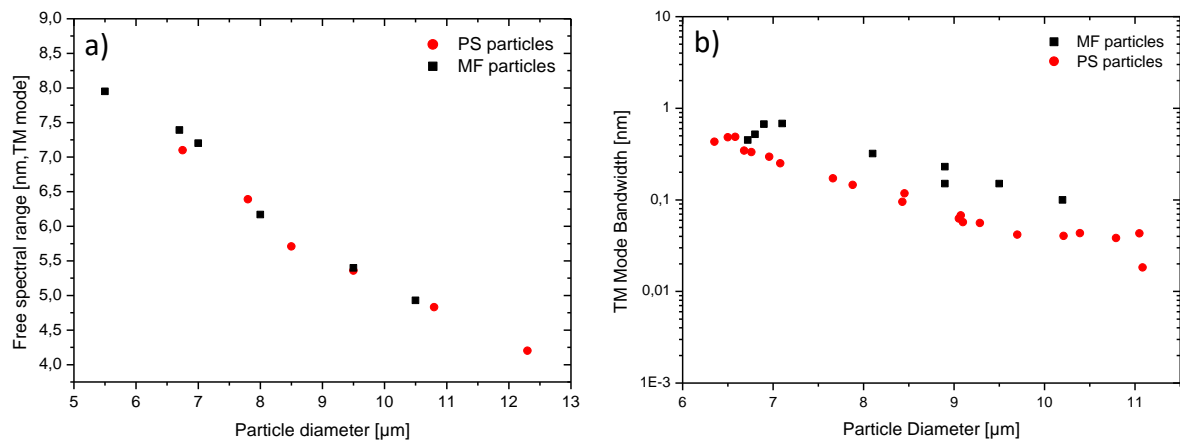
Figure 38. Distance between subsequent TM Modes (a) and WGM bandwidth (b) as a function of particle diameter (for MF and PS particle).

Both particles types present similar and proportional dependence of free spectral range on particle size. From a practical point of view, a nominal distance between successive TM or TE modes above 6 nm is undesirable, since less as three modes number per spectrum can be detected (a typical wavelength range in our low-Q WGM sensing system is around 15 nm). Besides the mode spacing, WGMs bandwidth is also showing an explicit dependency on the particle size. The present investigations confirm that PS particles exhibit narrower FWHM than MF particles in the whole range of size. As reported previously (see §4.1.1.1 and §4.1.1.2), the

75

reason for this is related to their higher real refractive index and lower surface roughness. Nevertheless, if the acceptable upper limit of bandwidth is set for 0.1 nm, a minimal diameter of PS particles should be above 8.5 μm while for MF above 10 μm. Therefore, a suitable particle size range for the Low-Q WGM sensing system should be appointed between 8.5-11 μm for PS and 10-11 μm for MF particles.

4.1.4 Fluorescent dye

One of the undeniable advantages of low-Q WGM microresonators over microresonators operated in high-Q regime is overcome the need for a critical evanescent field coupling usually realized by connection an optical fiber tangentially to the particle surface. Instead of this complicated procedure, the WGM excitation in low-Q WGM sensors is performed via fluorophore excitation inside of the particle by an external light source. This approach exploits as well the advantage to measure the sensor signal without any contact with the measuring unit.

However, it requires an appropriate fluorescent dye taking into account many aspects such excitation/emission wavelength, molar extinction coefficient and fluorescence quantum yield, photoresistance, solubility in water/organic solutions or stability against the radical formation. Therefore, in subsequent sections, an in-depth screening of affordable fluorescent dyes was performed.

Eight types of fluorophores were selected and investigated by means of WGM excitation. Water-insoluble perylene and coumarin 6 were incorporated into PS particles while water-soluble fluorescent dyes: acridine yellow, perylene tetracarboxylic dianhydride (PTCDA), coumarin 343, fluorescein, rhodamine B and rhodamine 110 were incorporated into MF particles. Table 7 presents the main characteristics of the fluorescent dyes used.

Table 7. The main characteristic of fluorescent dyes used for the preparation of low-Q WGM microsensors (obtained in ethanol)

Fluorescent dye	Excitation max. (nm)	Emission max. (nm)	Molar coefficient (cm^{-1}/M)	Quantum Yield	Solubility in water
Coumarin 6	449	479	54,0	0,78	water-insoluble
Perylen*	441	449	38,5	0,94	water-insoluble
Acridin Yellow	449	466	39,4	0,47	water-soluble

Perylenetetracarboxylic acid (PTCDA)**	479	491	37,0	0,92	water-soluble
Coumarin 343	440	474	44,3	0,63	water-soluble
Fluorescein	494	512	70,0	0,97	water-soluble
Rhodamine B	565	579	106,0	0,70	water-soluble
Rhodamine 110	530	540	80,0	0,92	water-soluble

*   measured in cyclohexane; **   measured in xylene

A key point in the selection of fluorescent dye for low-Q WGM sensors is the determination of the wavelength range that will be detected and analyzed during standard measurements. As known, the WGM spectrum depends directly on the maximum emission wavelength of fluorophore incorporated inside the particle. Furthermore, the emission wavelength of fluorophore should be correlated with particle size according to the rule: the smaller particle size is the shorter the maximum emission wavelength of the dye has to be. Therefore, most selected dyes present short maximum excitation and emission wavelength (< 500 nm). It allows using sensors with small diameter (6-11 µm) and affordable light sources (typically: 405 nm laser diode).

Besides the adsorption/emission spectrum, other spectroscopic properties that should be taken into account by the selection of fluorescent dye are molar extinction coefficient and quantum yield. For almost all fluorescent dyes (except Acridin Yellow and Coumarin 343) these parameters present high values. It is especially needed in the case of photobleaching effect because it allows reducing the excitation laser power while maintaining the WGMs intensity still at a high level. Obviously, the WGMs intensity can be enhanced by increasing the fluorophore concentration inside the particle. In practice, however, this method often leads to a self-quenching effect and is sharply limited by their solubility in sensor material.

Last but not least the incorporation of the dyes in a sufficient amount is a further very critical point. A post dying procedure is possible for PS particles but yields some drawbacks as it will be shown in chapter 4.1.5. Hence, the dyes have to be incorporated already during the synthesis. The polycondensation of melamine and formaldehyde forms a dense and stiff structure which cannot be swollen anymore by solvents as in the case of PS particles. Therefore, the diffusion of dye molecules into the formed MF structures is not anymore possible due to the pore size is obviously too small. For this reason, in the case of MF particles, the dyes have to be incorporated already during the synthesis which is performed in an aqueous solution. Hence, the dyes have to be water-soluble while for PS particles they have to be oil soluble.
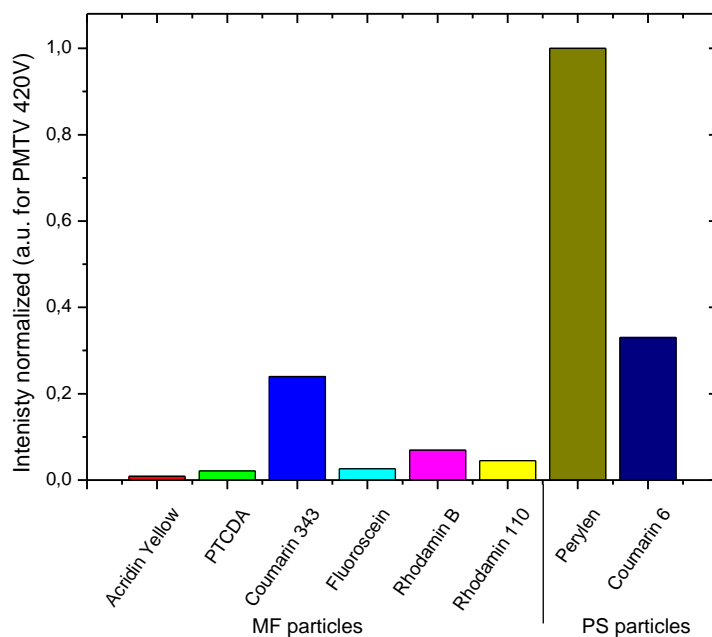
Figure 39. Fluorescence intensity of low-Q WGM microbeads labeled with selected fluorescent dyes (*CLSM, Ex. 405nm and 535 nm; Em. 450-550 nm and 550-650 nm*).

As presented in Figure 39, MF microparticles labeled with water-soluble fluorescent dyes show mostly much lower fluorescence intensity than PS microparticles labeled with water-insoluble fluorescent dyes. On the one hand, it can be explained by the limitations of dye solubility in the aqueous reaction medium and on the other hand on the generally reduced fluorescence quantum yield in water compared to organic solvents. Another cause for the low fluorescence intensity of MF particles could be related to the presence of acid in the second step of preparation. The change of pH from alkaline to acidic is necessary to catalyze the polycondensation of methylolmelamines to form MF structures. However, it decreases the solubility of anionic fluorescent dyes, e.g., PTCDA. It leads to precipitation of dye molecules and finally low concentration in particles. Also from this point of view, MF particles labeled with water-soluble fluorescent dyes seem to be less suitable for low-Q WGM.

In contrast, PS particles are very hydrophobic, therefore, incorporation of fluorophore molecules is usually more stable based on non-polar interactions. Using the right organic solvents, they are also much better soluble than comparable dyes in water.

A major issue by selecting appropriate fluorescent dye for labeling low-Q WGM sensors is their resistance to photobleaching. Irreversible destruction of excited dye molecules is a primary factor limiting the usability of fluorescent low-Q WGM sensors in long term kinetic

measurements. Although the shift is not influenced by the bleaching, the WGM signal intensity becomes lower and the signal/noise ratio is increasing. Hence, a precise determination of photobleaching of dyed PS and MF particles labeled with the selected fluorescent dyes was performed.

For that, fluorescent PS and MF particles were continuously excited with an appropriate laser and constant power (10% of max. power for 405nm laser and 15% of max. power for 535nm laser) for 10 minutes in CLSM. The fluorescence intensities of single particles were continuously measured and saved. The results of particle bleaching are shown in Figure 40.
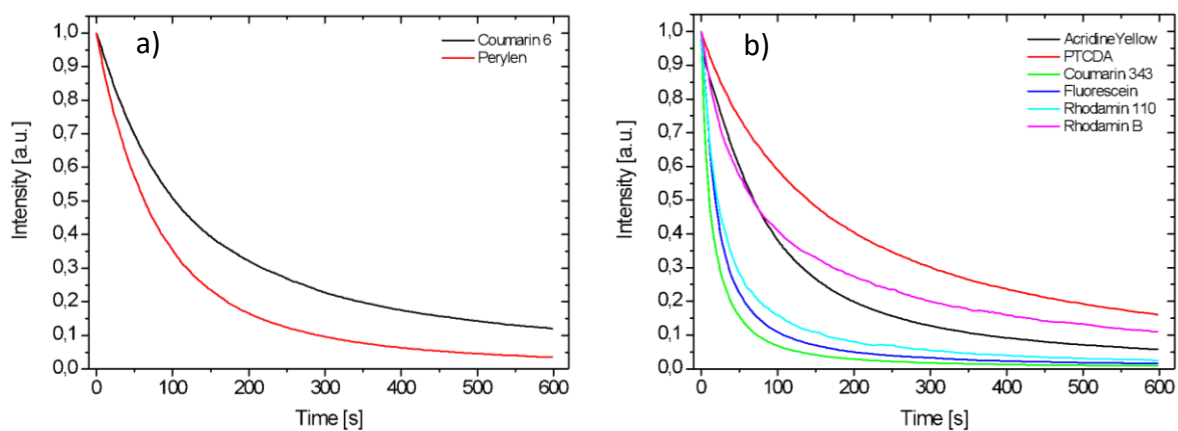
Figure 40. Photobleaching of low-Q WGM particles labeled with different fluorescent dyes. (a) PS particles labeled with water-insoluble fluorophores and (b) MF particles labeled with water-soluble fluorophores.

The best resistance to photobleaching was observed for PTCDA dye (50% decreasing of the fluorescence intensity was achieved after 150s). Acridine Yellow, rhodamine B, coumarin 6 and perylene show already significantly worse photoresistance than PTCDA but still with acceptable value (50% decrease in fluorescence intensity was observed after around 80-100s). Coumarin 343, fluorescein and rhodamine 110 exhibit highest photobleaching effects (50% decrease in fluorescence intensity was observed already after 25s). Summarizing, although MF particles labeled with PTCDA show significantly better photoresistance than PS particles labeled with coumarin 6 or perylene, taking into account also the fluorescence intensity, PS particles seem to be more suitable as fluorescent low-Q WGM sensors.

4.1.5 Dye distribution

Distribution of fluorescent dye inside the particle plays an essential role in WGM resonance performance since the incidence angle of emitted light mainly depends on the location of fluorophore molecules towards the particle/environment boundary. To put it more clear: if the distance of fluorescent dye molecules increases from the particle surface, the incidence angle of emitted light decreases. It leads to worse TIR conditions and finally, broader WGMs. Moreover, as already reported,[190] fluorescent dyes mainly located in the middle point of the sphere contribute to a higher fluorescence background since these photons do not participate in the forming of WGMs.

In order to determine an optimal distribution of fluorescent dye molecules inside low-Q WGM microsensors, three dyeing methods were investigated: standard dye-doping method, gradual solvent evaporation method, and fluorescent LbL coating. Fluorescent dye-doped PS microparticles in size range of 10 μm were obtained from Surflay Nanotec GmbH. In the case of gradual solvent evaporation method,[196] non-colored PS particles were fluorescently labeled with Coumarin 6 dissolved in a swelling agent (a mixture of chloroform/2-propanol in a ratio of 1:3, 1:5 and 1:7, respectively). Fluorescent LbL PS particles were coated up to six bilayers of PAH-C343/PSS by means of LbL technology.[190] Figure 41 and 42 show typical CLSM images and WGM spectra obtained for PS particles dyed by selected methods, respectively.
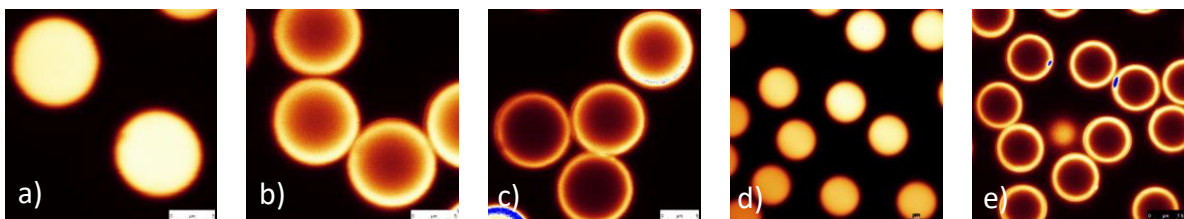
Figure 41. CLSM images of PS microparticles dyed by different methods. (a-c) Gradual solvent evaporation method with the chloroform/2-propanol swelling agent in a ratio of 1:3, 1:5, and 1:7, respectively. (d) Dyed-doped method. (e) Fluorescent LbL coating. (excitation by 405 nm laser, DAPI channel, 63x objective, zoom 6 (a-c) and 4 (d-e)).
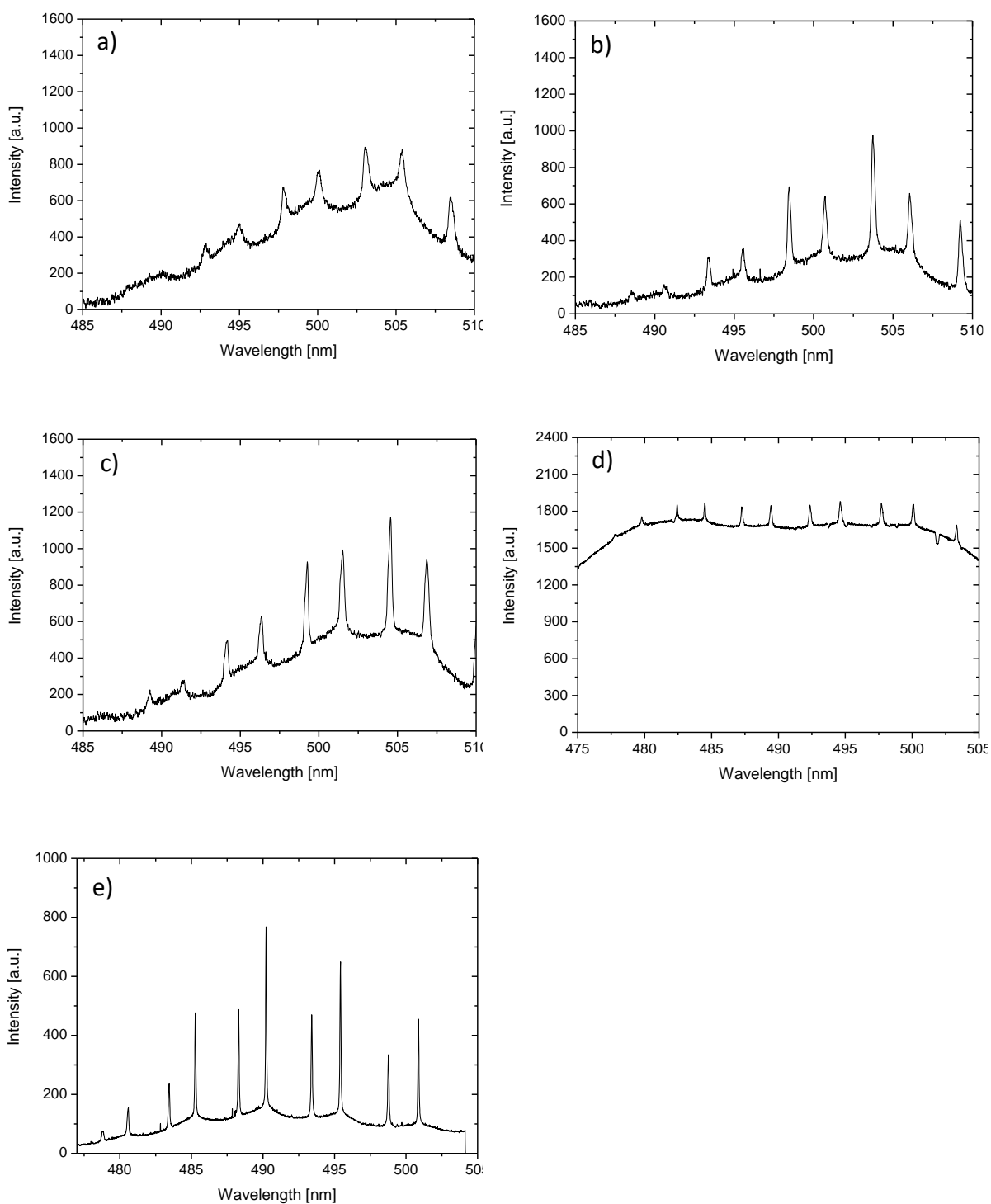
Figure 42. WGM spectra of PS particles dyed by different methods. (a-c) Gradual solvent evaporation method with the chloroform/2-propanol swelling agent in a ratio of 1:3, 1:5, and 1:7, respectively. (d) Dye-doped method. (e) Fluorescent LbL coating.

Particles dyed by gradual solvent evaporation method exhibit diversified dye distribution dependent on the concentration of chloroform in a swelling medium. In the presence of 25%

chloroform, the particles swelled to be much bigger so that the dye molecules can quickly diffuse from medium deeply to the polymer matrix, leading to homogenous fluorophore distribution (Figure 41a). However, because of the lower boiling point and relatively high concentration, the chloroform is easier to be evaporated than isopropanol, resulting in fast and unevenly shrinking of the particles. It is making worse their sphericity and surface homogeneity leading to the higher losses of resonance modes by light scattering and broad WGM spectra (Figure 42a). Since the concentration of chloroform decreases, only a certain outer layer of the particle can be swollen and penetrated by dye molecules (Figure 41b-c). It results in a higher signal/background ratio and sharper peaks (Figure 42b-c).

The standard dye-doped particles with homogenous dye distribution and high fluorescence intensity (Figure 41d) show narrow WGM modes but low signal/background ratio (Figure 42d). The high background signal arises from fluorophores located far away from the surface and deeply embedded inside the particle. Their emitted light hits the interface always at angles above the angle of TIR and does not contribute to the WGM signal, while the spectrograph still observes it as background noise. In contrast, PS particles coated with thin fluorescent LbL film (Figure 41e) show very low background fluorescence, whereas the WGM signal is remaining still at a high level (Figure 42e).

To provide a broader view of the fluorescent LbL-coating method and its promising application in the preparation of Low-Q WGM sensors, a detailed analysis of the coupling mechanism of light, as well as the influence of deposited layer number, salt, temperature, and surface pre-modification was performed.

4.1.6 Fluorescent LbL-coating

As presented above, the immobilization of the dyes molecules onto the particle surface by using the fluorescent LbL-coating resulted in high-quality and intensive WGMs as well as in low fluorescence background. Besides the high performance of the WGMs, the LbL coating offers the possibility of incorporating different target molecules or functional groups as well as other sensing functions.[168,166] Furthermore, since the fluorescent LbL-coating can be applied to different non-coloured beads, it can be very useful for the selection of the sensor material as demonstrated in paragraph 4.1.1.

4.1.6.1 Tunneling effect

From a physical point of view, it is interesting, however, how the photons emitted from the dyes molecules located within the thin LbL-film can enter the particle, circulate and form sharp WGMs since the RI of the PE-coating is significantly lower (~ 1.47)[49] than of the microresonator material PS (RI = 1.56) or MF (RI = 1.53). According to the WGM fundamentals, if the difference between the effective RI of the cavity and RI of the environment is too small, the emitted photons cannot be reflected at the resonator boundary and WGMs will not be formed. This law has been also proven in this work (§ 4.1.1). For microresonator materials with low RI, as for example PMMA (RI = 1.48) or SiO_2 (RI = 1.42) WGMs are not formed for small diameters. So the question remains: how the light emitted from dye molecules located in the LbL film can be propagated along the particle surface? It seems likely that the coupling of light by fluorescent LbL-coated beads is similar to the tangential fiber excitation performed in High-Q resonators. Photons emitted from the fluorescent LbL-film are tunneling through the boundary between LbL-film and cavity and form efficiently the WGM modes circulating inside the particle. Since the LbL coating of only few nanometer thickness is always tangentially oriented and very close around the whole particle surface within the evanescent field the tunneling process is especially effective. The high quality of the modes might also profit from the unperturbed PS matrix since no dye molecules could cause secondary effects like reabsorption or self-quenching of the circulating modes. The possibility to use none-fluorescent particles coated with a fluorescent LbL film allows the investigation and use of other spherical particles for which a dye labeling might be difficult or impossible like silica (see also chapter 4.1.1), silicones, titanium dioxide and further inorganic materials.

4.1.6.2 Dependence of WGM performance on deposited polymer layer number

The LbL process allows subsequent deposition of homogeneous polyelectrolyte layers of a few nanometers of thickness. As reported in the literature, the deposition of polyelectrolyte layers

should have a negligible effect upon the surface roughness.[197,198] However, at higher layer numbers, the quality of WGMs can get worse by decreased effective RI of the sphere. To gain a better understanding of these effects, the bandwidth and intensity of WGMs were studied in dependence on the deposited layer number of PAH-C343/PSS.
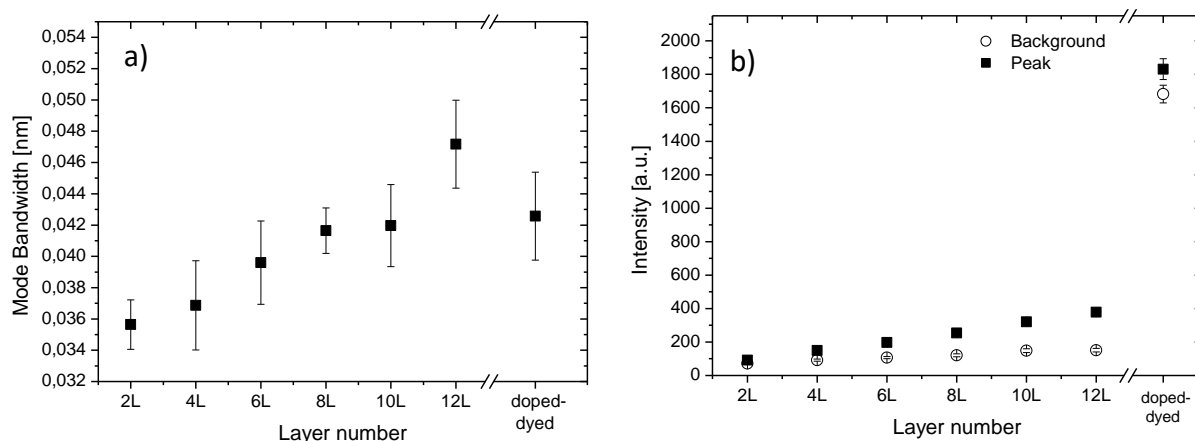
Figure 43. Characterization of non-fluorescent PS particles coated with fluorescent LbL-films (PAH-Coum343/PSS)$_n$ by means of WGMs. (a) Mode bandwidth as a function of layer number and (b) correlation between layer number and fluorescence intensity of background and WGM peaks.

In the case of the small number of deposited layers (<3 double layers), no significant influence on mode bandwidth compared to the standard dye-doped beads was observed. At higher layer numbers, the quality of the WGM signals decreases slightly (Figure 43a) both by increasing surface roughness and by decreasing effective RI as mentioned above. The WGM signal intensity also depends on the number of polyelectrolyte layers (Figure 43b). With each polycation layer, the number of deposited dye molecules at the particle surface increases, which enhances the WGM signal intensity strongly, whereas the background is only weakly enhanced. Summarizing, there is a trade-off between signal intensity and quality: the increasing number of deposited polyelectrolyte-fluorophore layers increases the overall signal intensity (more fluorophores) but decreases the Q-factor (increased surface roughness and decreased total RI). Hence, the optimum layer number was found to be 6 to 10 for the PAH/PSS system.

4.1.6.3 Optimization of the fluorescent LbL coating on polystyrene microparticles

As demonstrated in previous chapters and already published,[190] the immobilization of the dye molecules at the outer particle surface by employing the LbL-assembly technique turned out to be a rapid and versatile method to produce low-Q-WGM sensor. However, the build-up of homogeneous LbL film with controlled layer thickness onto polystyrene particles having a steric stabilization, is not very effective. Therefore, it was tried to improve the affinity of PEs significantly by suitable modifications of the particle surface

Two approaches in the modification of polystyrene particle surface were investigated. In the first approach, the polystyrene beads were modified by the use of physicochemical methods, including Plasma treatment, EDTA, and SDS adsorption as well as sulphonation, and nitration. In the second approach, the particles were pre-coated with different basic layers of polyelectrolytes by means of LbL self-assembly. The LbL-coating-ability was determined by the deposition of a single layer of PAH-Rhodamin and measurement of the obtained fluorescence intensity in CLSM.
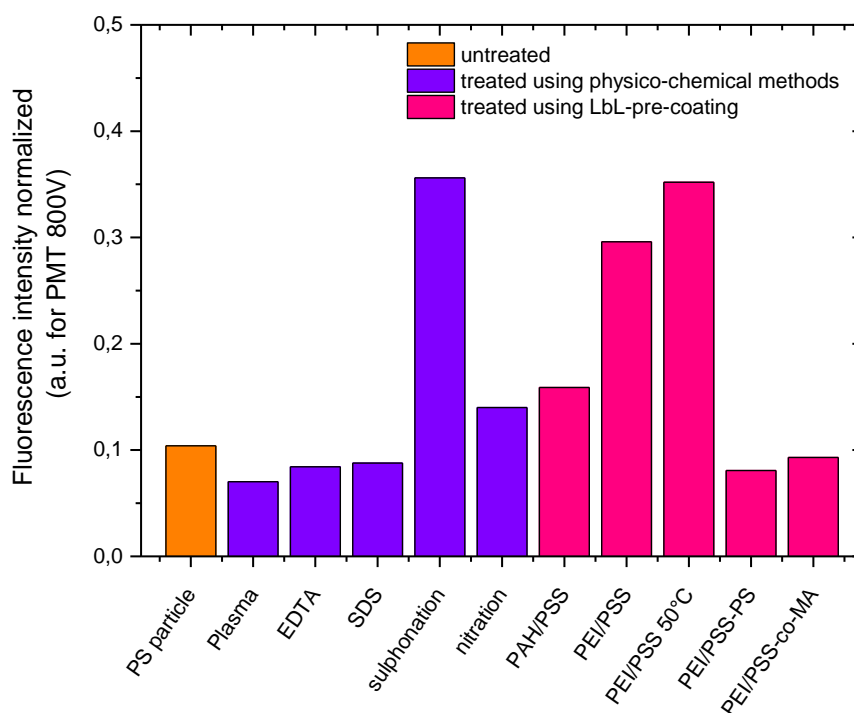
Figure 44. Comparison of different particle treatments to improve the adsorption of PAH-Rho as a measure for the LbL adsorption affinity (*CLSM, Ex 532nm, TRITC channel*)

As shown in Figure 44, the highest affinity of PAH-Rho was achieved to PS particles treated with sulfonic acid or LbL-film using the combination of PEI/PSS. In case of PEI/PSS-coated particles, the number of adsorbed PAH-Rho chains has been further increased by deposition of the film at higher temperatures (50°C). Therefore, for further LbL modification of the particles, a pre-coating with PEI/PSS at elevated temperature was in general performed. Although the sulphonation leads to an effective PAH-coating, the WGM-modes became broader. Probably the sulphonation creates some surface roughness or scattering centers on the surface perturbing the circulation of the modes.

Other types of polyelectrolyte combinations, such as PAH/PSS, PEI/PSS-co-PS (polystyrene) or PEI/PSS-co-MA (maleic acid), resulted in less improving of LbL-coating.

4.1.6.4 Stability of LbL-coated WGM microresonators in solution of high ionic strength

Although the LbL coating of WGM beads is a versatile approach for surface modifications in the absence of organic solvents, the responsiveness of LbL films to the environment,[166] might influence the WGM signal as well. Several studies have shown that PE multilayer films change their thickness and density or even partially disassemble at high ionic strength, high or low pH[199,165] or by addition of ions that form stable complexes with one polyelectrolyte of the film such as cationic amphiphiles with PSS.[200] Although the PAH/PSS is known to be one of the most stable polyelectrolyte combinations, such effects can limit the applicability of LbL-coated WGM sensors. In order to clarify the effects of ionic strength, three different types of WGM particles were created and treated with increasing salt concentration.

Dye-doped PS beads either bare, coated with 12 PAH/PSS polyelectrolyte layers (PSS is the outermost layer) or 13 layers (non-labeled PAH is the outermost layer) in comparison with non-fluorescent PS beads coated with 12 and 13 PAH-Coumarin/PSS polyelectrolyte layers. The ionic strength was varied with NaCl concentrations of 0 mM, 250 mM, 500 mM, and 750 mM (Figure 45).
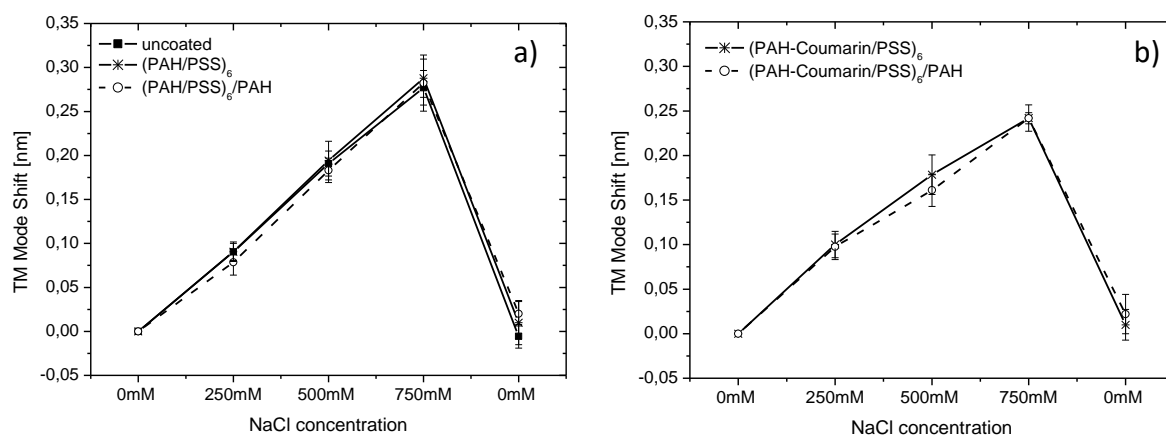
Figure 45. WGM shifts of (a) dye-doped and (b) fluorescently LbL-labeled PS beads as a result of rinsing with NaCl solutions in different concentrations. The PS beads were either native or coated with non-fluorescent polyelectrolytes combination: (PAH/PSS)$_6$ and (PAH/PSS)$_6$/PAH. The error bars indicate the standard deviation of TM-Mode shift from 10 particles.

As already reported in the literature,[50] the WGM position of non-coated and PE-coated dye-doped PS beads depend clearly on the salt concentration, as a result of the change in the RI of the medium. Taking this into account, no discernible difference in the WGM position between both particle types has been observed. The swelling or shrinking of the LbL film does not influence the signal intensity, because the increase of water content (leading to a reduction of the layer RI) is entirely compensated by the increase of layer thickness. Hence the effective refractive index of the film does not change, and the WGM signal is not influenced by shrinking or swelling of the LbL film. Furthermore, the complete recovery of the WGM position after flushing back to salt-free water proves the stability of the film in solutions of at least 0.75 M ionic strength. Extreme conditions like pH values above 11 can disintegrate the PAH/PSS film due to deprotonation of PAH.[201] Surprisingly, the non-fluorescent PS beads coated with PAH-Coumarin/PSS film exhibit subtly smaller WGM-shifts than the other beads at a salt concentration above 250 mM. The reason is not apparent yet and needs further clarification. The independence of the WGM signal on the swelling or shrinking of the PAH/PSS LbL films indicates that LbL coating technology is suitable for the production and functionalization of WGM sensors.

4.1.6.4 The effect of temperature changes on the mode wavelength

Since the sensing principle of many optical label-free methods as SPR, BLI or ellipsometry is based on the changes in the refractive index, the binding to the biosensor is sensitive to fluctuations in temperature. As is known, as the temperature of liquid increases, the refractive index decreases. In water, for example, the RI decreases between 0.0001 to 0.0002 for every 1°C increase in temperature (for a temperature range of 10-70°C and λ = 405nm).[202] Hence, for methods that are very sensitive to changes in RI e.g. SPR (sensitivity approximate to ~1700-8800 nm/RIU depends on the type of SPR spectrometer)[203,204] even small fluctuations in temperature of 0.1°C can induce an evident response in the signal. In contrast, the Low-Q WGM sensors are significantly less sensitive to changes in RI (21nm/RIU),[49] which probably also leads to less sensitivity to temperature changes. To confirm these assumptions, the influence of temperature on the mode wavelength of the Low-Q WGM sensors was studied. The dye-doped PS beads (the nominal diameter of 10 μm) either bare and coated with two and five bilayers of PSS/PAH and PSS/PDADMAC were fixed in the microfluidic chip equipped with a temperature sensor and rinsed with water in the temperature range from 10°C to 70°C. The WGMs were measured after each 2.5°C increase of temperature. The reference point was set at 20°C (normal temperature and pressure). In order to determine the contribution of thermal tension of particle material and Δn_s in the total mode shift as the temperature increasing, the obtained values for bare particles have been compared with the results of the sensitivity of mode shift for Δn_e demonstrated by M. Himmelhaus as well own investigations presented in section § 4.1.5.6.
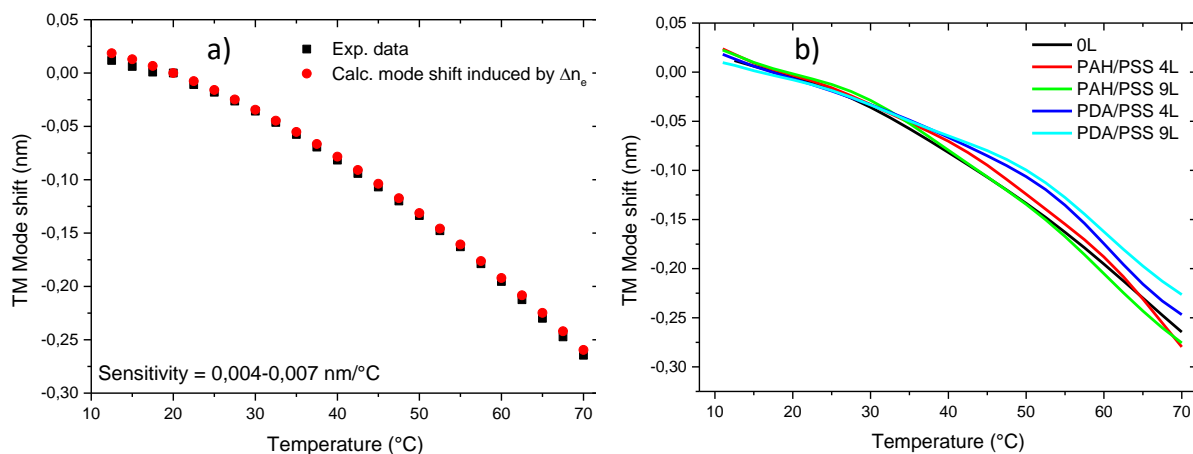
Figure 46. The TM Mode shift of native (a) and LbL-coated (b) Low-Q WGM particles as a result of temperature changes. On the plot (a): The experimental results of native particles (black squares) were compared with the calculated mode shift induced by the changes of RI in the environment (red circles).

As can be seen in Figure 46a, the TM-Mode of the native particles shifts negatively as the temperature increases. It can be supposed that the decrease of the density and refractive index of the resonator material due to thermal expansion is compensated in total by the increase of the particle diameter. In consequence, the WGM shift is only caused by the changes in the refractive index of the environment (n_e, red points). However, despite this, the sensitivity of Low-Q-WGM sensors to temperature changes remains still at a very low level and is around 0.004-0.007 nm/°C, where, for example, by SPR spectrometers is commonly above 1 nm/°C.[203]

The WGM sensors coated with PSS/PAH film showed similar mode shift as native beads whereas the particles coated with the PSS/PDADMAC film demonstrated a smaller shift (Figure 46b). As expected and according to the literature,[205] the negative mode shift induced by decreasing of n_e was partly compensated by increased LbL-film thickness. The effect of swelling of PSS/PDADMAC film at high temperatures can be caused by increased fluidity and flexibility of polyelectrolytes.[205]

4.1.7 Summarizing Discussion

In this part of the thesis, optimal fluorescent low-Q WGM microsensors have been developed by a selection of suitable particle material types, polymerization method, particle size, fluorescent dye, and dye immobilization method.

The investigations of different particle materials show that PS, MF, and BG particles coated with fluorescent-labeled LbL film could be applied as low-Q WGM sensors. Nonetheless, the best WGM spectra were obtained for PS particles, while MF and BG particles show broader and less intense peaks. The reason can be related to their lower RI, higher surface roughness, and non-ideal spherical shape. Furthermore, the precise determination of RIs performed by WGM revealed that the RI of MF microparticles is remarkably lower than the bulk material. This observation challenges the assumptions in previous studies and patents proposing MF particles as the best Low-Q-WGM sensors based on the RI values of bulk material.[56,57]

The best-suited polymerization method to fabrication polystyrene low-Q WGM sensors is seeded-growth polymerization. Compared to dispersion and emulsion polymerization, seeded-growth polymerization allows preparing highly monodisperse PS particles with narrow and intense WGMs. Moreover, in seeded-growth polymerization, the particle diameter can be easily and precisely controlled by the selection of seed particle size and reaction time.

The study of the influence the resonator's diameter on the WGM signal reveals that the optimal size range for PS particles is between 8.5- 11 µm while for MF particles it is between 10-11 µm. Particles with a smaller diameter show remarkably broader WGM bandwidth FWHM than an acceptable limit of 0.1 nm, making the analysis of mode position more difficult and inaccurate. On the other hand, if the particles are larger than 11 µm, additional weak peaks in the WGM spectrum are observed making the automatic evaluation of the shift less accurate. An in-depth analysis of the WGM bandwidth and mode distance confirms that PS particles are more suitable as low-Q WGM resonators than MF particles.

Screening of different fluorescent dyes shows that water-insoluble perylene and coumarin 6 can be successfully applied to immobilization into WGM sensors PS particles. Other types of water-soluble fluorescent dyes immobilized into MF particles show lower fluorescence intensity probably caused by smaller quantum yield in the polar environment and limited incorporation of dye molecules during the particle synthesis. A study of photostability reveals that the best resistance to photobleaching was obtained for coumarin 6 (incorporated in PS particles) and PTCDA (incorporated in MF particles). However, taking into account previous results in fluorescence intensity as well as other fluorophore properties such as maximum excitation/emission wavelength, molar extinction coefficient, quantum yield or stability, coumarin 6 in PS particles was selected as a best suited fluorescent dye for WGM resonators.

The fluorescent LbL coating and standard dye-doping proved to be the best methods for the immobilization of fluorescent dyes on WGM- PS particles. In contrast, particles labeled by gradual solvent evaporation method show significantly less intense and broader peaks caused by non-spherical and less homogeneous particle surface.

The fluorescent LbL coating and standard dye-doping proved to be the best methods for the immobilization of fluorescent dyes on WGM- PS particles. In contrast, particles labeled by gradual solvent evaporation method show significantly less intense and broader peaks caused by non-spherical and less homogeneous particle surface. The fluorescent LbL coating yields WGM sensors exhibiting several advantages over the dye-doped particles such as low

background signal, more versatility of sensors materials and easy (bio)functionalization. The optimal LbL film thickness in view of signal intensity and quality (WGMs bandwidth) is 12-20 nm, which amounts to PAH/PSS to 6-10 layers. However, the signal intensity is below the dye-doped particles due to the small available volume for dye immobilization and continuous measurements lead to stronger photobleaching of the dyes. Hence, the optimal labeling method (dye-doped or LbL-coated) depends on the application and has to be evaluated in advance for the specific analyte.

The study of the sensitivity of the Low-Q WGM sensors to the changes of RI in the environment revealed that the minimal detectable difference of RI is 2×10^{-4}. This value is lower than for the highly optimized SPR instrument BiaCore (RI sensitivity = $1\text{-}6 \times 10^{-6}$).[203] But the developed Low-Q WGM sensors needs much less analyte molecules, are much cheaper, can be efficiently modified outside of the measuring device, can be measured without any contact with the measuring device and can be applied with high spatial resolution in very small cavities, even inside cells.

The investigations of the influence of temperature on the WGM signals showed only a surprisingly small negative shift. This shift is proportional to the change in RI of the aqueous environment. The temperature sensitivity was determined of only 0.004-0.007 nm/°C. Therefore a complicated setup for achieving a constant temperature during the measurements is not necessary as in case of SPR instruments.[203]

4.2 Label-free analytics using fluorescent Low-Q WGM microparticles

In this part of the thesis, the practical applications of fluorescent low-Q WGM microparticles as novel label-free biosensors were demonstrated. The results are divided into three parts. In the first part, the WGM measurements of the unspecific adsorption of polyelectrolytes based on electrostatic and hydrogen interactions were performed. The influence of layer number, ionic strength, and polymer concentration was studied. In a second section, three label-free detection systems: SPR, QCM, and WGM were compared by means of unspecific binding of lysozyme. The final section dealt with studies of specific interactions between biotinylated molecules and streptavidin-modified sensor surface.

4.2.1 WGM-analysis of the Layer-by-Layer coating

LbL ultrathin film fabrication technique is currently a widely used method in the modification and functionalization of different materials and structures. In particular, the coating of colloidal substrates such as nano- or microparticles has been achieved great attention due to the formation of capsules with precisely defined wall properties.[156] To date, however, most studies about the LbL process were performed on planar substrates by means of QCM,[162,206] neutron scattering,[207] ellipsometry[162,208] or SPR[209] while the important LbL assembling on colloidal templates was studied only by indirect methods such as fluorescent labeling of polyelectrolytes.[156] Hence, there were some discussions in the LbL community if the preparation of LbL capsules on colloidal templates performed by several centrifugation or filtrations steps is comparable to the planar LbL films, which are prepared much simpler by dipping. Thus, the label-free WGM detection system is a new option to study the assembling and the stability of the LbL thin films directly on colloidal microparticles.

4.2.1.1 LbL assembling based ion attraction

Typically, the LbL self-assembly process is referred to as the formation of multilayers ultra-thin films based on electrostatic forces between oppositely charged polyelectrolytes. The adsorption kinetics and quantity of the LbL deposition process depend strongly on many parameters such as polyelectrolyte material and concentration, ionic strength, pH value,

temperature, surface charge etc.[156] In particular, the salt concentration and pH value of the polyelectrolyte solution are essential factors in the formation of multilayer films. The pH value determines directly the number of charged groups in weak polyelectrolytes and thus their electrostatic interactions. The ion strength influences directly the structure of the polyelectrolytes and the assembling process due to shielding the polyelectrolyte charges by the ions. For example, at low salt concentration, the strong electrostatic repulsion of ionic groups results in polymer chains that are "stretched," forming a thin and dense LbL film (Figure 47a). In contrast, the high salt concentration of PEs solutions weakens the electrostatic repulsion between ionic groups and lead to coiling of the polyelectrolytes in solution and in assembling of larger polyelectrolyte amounts in the LbL process making the LbL structure less compact and thicker (Figure 47b).
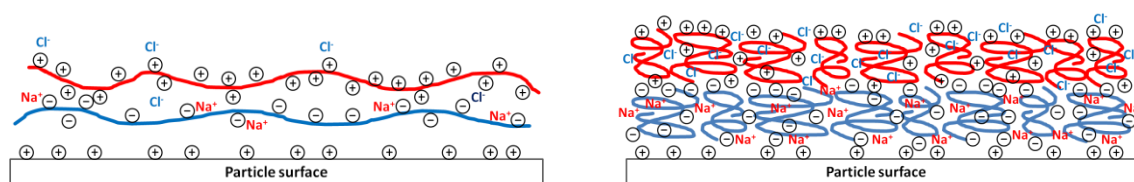
Figure 47. A schematic illustration of the influence of salt concentration on the LbL film structure: low salt concentration (left) and high salt concentration (right).

The film structure also depends on the LbL growth regime. Two basic growth regimes can be distinguished: linear and exponential. In linear growth, the thickness and mass of LbL film grow linearly with the number of deposition steps while in exponential buildup each subsequent bilayer is thicker than the previous one. The LbL growth regime depends mainly on the type and combination of PEs, but it is worth mentioning, that some assembly conditions such as temperature, salt type, layer number or concentration can change the regime, e.g. converting the linearly growing film to exponential growth.[162]

In order to study the influence of polyelectrolyte combination and salt concentration on the LbL growing process and film thickness on spherical substrate, PS particles were coated up to five bilayers of poly(sodium-4-styrenesulfate) (PSS) and poly(allylamine hydrochloride) (PAH) as well as of PSS and poly(diallyl dimethylammonium chloride) (PDADMAC) in the presence of 0.2M and 1.5M NaCl and measured by means of the WGM detection system. The WGM shift was recorded after the deposition of each polymer layer and converted into the adsorbed

mass value and film thickness by using equations 1 and 10, respectively (Figure 48). It should be noticed here, however, that for the strong swollen LbL films the calculated thickness may be different compared to the other label-free methods e.g. QCM since the WGM system cannot determine the mass of water.
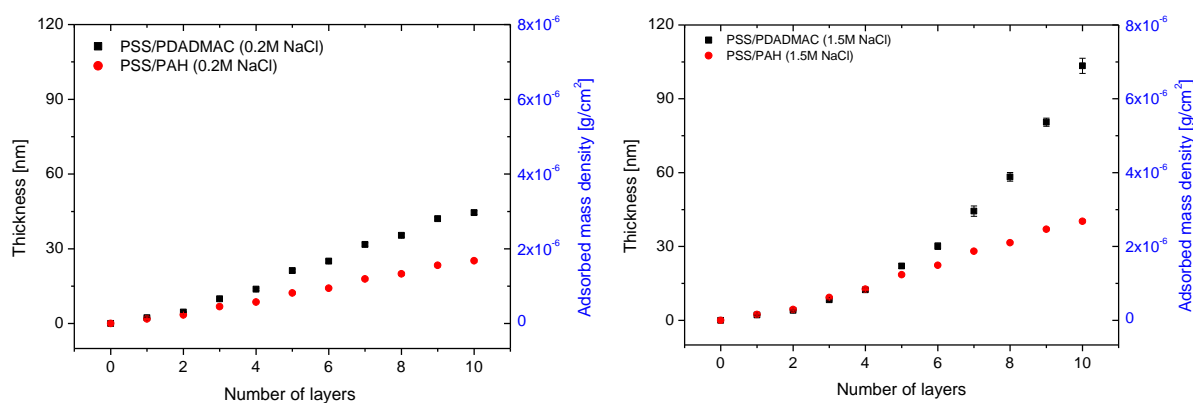
Figure 48. LbL film thickness and adsorbed mass of polyelectrolytes determined in WGM during deposition of PSS/PDADMAC and PSS/PAH in 0.2M (left) and 1.5M (right) salt concentration.

It was found that the deposition of PSS/PAH in both concentrations of salt, i.e., 0.2M and 1.5M leads to linear growth of LbL films while the combination of PSS and PDADMAC leads to linear growth in the presence of 0.2M NaCl but significantly exponential growth in the presence of 1.5M NaCl. The mechanism responsible for the exponential buildup process has not been completely understood yet. According to recent publications, non-linear growth of the LbL film can be caused by excessive adsorption of PEs with a low-density charge through in-and-out diffusion of polymer chains.[210,211] Especially, in case of high salt concentration, the ionic groups on polyelectrolytes will be strongly hydrated, which in turn leads to swelling of LbL film and easily diffusion of weakly bonded free polymer chains into the LbL film.

The WGM values of film thickness and mass density of polyelectrolytes on the colloidal PS templates are surprisingly quite similar to the values obtained by Elzbieciak-Wodka et al. for QCM and ellipsometry measurements on planar films.[162] As it is known, the QCM and ellipsometry technique uses a planar sensor with a significantly larger sensing area and surface coating (typically Au or SiO_2) than the WGM-sensing system. Although the larger sensing area does not contribute directly to layer thickness and the adsorbed mass density of polyelectrolytes, the sensor shape as well as the surface properties (roughness, charge, hydrophobicity, curvature) can remarkably modify the number and arrangement of adsorbed

polymer chains. On the other hand, according to the zone model of polyelectrolyte multilayer films proposed by G. Ladam,[212] only the first 1-3 layers in LbL-assembly are influenced by the template properties. Probably, the curvature at 10 μm particles is too small in order to reveal a large influence on the polyelectrolyte adsorption. The thickness and density of subsequent polymer layers are dependent mostly on environmental conditions as ionic strength, pH, temperature, etc.

4.2.1.2 LbL assembling based on hydrogen bonding

While the typical LbL films are deposited using electrostatic interactions between polyelectrolytes, some other interactions such as hydrogen-bonding, hydrophobic interactions, or covalent coupling can also be employed for multilayer film assembly.[213,214] In particular, LbL films based on hydrogen-bonding seems to be very interesting due to their high pH-dependent stability. As shown in Figure 49, in the case of the combination of Polyvinylpyrrolidone (PVP)/Polymethacrylic acid (PMAA), the hydrogen-bonding is formed only when the carboxylic groups on the PMAA are protonated. As the pH increases above the pKa of PMAA, the carboxylic groups will be deprotonated and the film constituents are decomposed. This can find practical application, for example, in medicine as the controllable release of LbL-integrated biological active components into the environment.
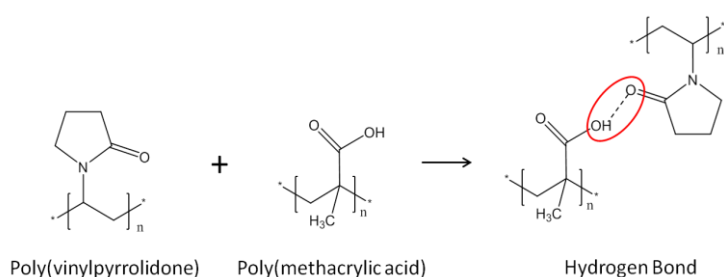
Figure 49. Chemical Illustration of the hydrogen bond between Polyvinylpyrrolidone (PVP) and Polymethacrylic acid (PMAA)

The LbL film based on hydrogen-bonding was studied by means of WGM sensing system under the two aspects:

(i) Determining of degradation kinetics of PVP/PMAA films depending on the pH value

(ii) Determining the influence of polymer concentrations on the layers thickness

For aim (i), the PS particles were equipped with a stable basic coating of PSS/PAH/PSS/PMAA film by means of LbL technology based on electrostatic interactions. Afterward, two bilayers of PVP/PMAA (1000 µg/mL, pH 2.0 set by HCl) were assembled based on hydrogen bonding. Between the subsequent coating solutions, the film was washed with the same buffer in order to have a constant refractive index. Finally, the LbL film was rinsed with an acetate/MES buffer (10mM each) at pH 4.2, 4.8, 5.2, 5.4, 5.6, 5.8, 6.4 to obtain release kinetic curves.

For aim (ii), on PS particles with the same basic coating PSS/PAH/PSS/PMAA, three bilayers of PVP/PMAA were assembled at decreasing polymer concentration. The first PVP/PMAA bilayer was deposited in the concentration of 1000 µg/mL for each particle sample while the second and third bilayer was deposited in the concentration of 1000, 100, 10, and 1 µg/mL, respectively. Finally, the LbL film was removed by washing LbL-coated PS particles in Borate buffer (10mM) at pH 8.0. The film thickness was calculated from the WGM shift (TM-Mode) using equation 10.
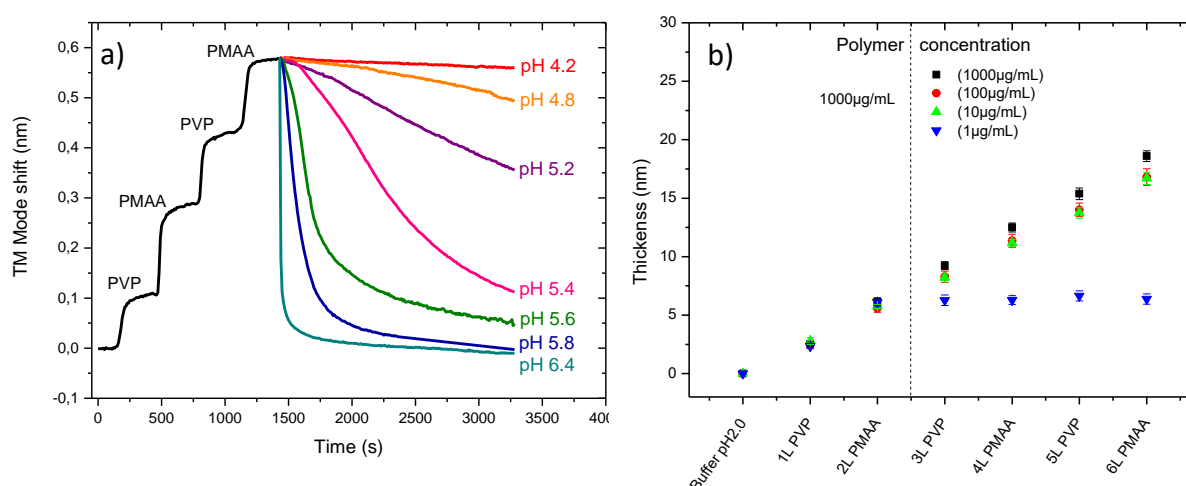
Figure 50. WGM study of LbL film self-assembly based on hydrogen-bonding. (a) Release rates of a (PVP/PMAA)$_2$ film depending on increased pH value after deposition at pH 2. b) The influence of polymer concentration on the deposited film thickness.

The washing of particles with an acetate/MES buffer at different pH values leads to various release kinetics curves of a PVP/PMAA film (Figure 50a). As was observed, as the pH value increases the time it takes to the decomposition of PVP/PMAA film decreases. By washing at pH 6.4, the LbL film was completely degraded in a few seconds.

In Figure 50b the influence of polymer concentration on the layers deposition is presented. For samples coated PEs in the concentration of 1000, 100 and 10µg/mL, the LbL film is growing

linearly in similar layer thickness. However, especially in the last two layers, both particle coated PEs in the concentration of 100, and 10 µg/mL show a slightly lower thickness than particle coated PEs in the concentration of 1000 µg/mL. Interestingly, for particles coated with a polymer concentration of 1 µg/mL, no deposition of polymers was observed. It has to be noticed here that, in the shallow concentration of PEs the dynamic process of adsorption/desorption of polymer chains on the sensor surface is in a continuous equilibrium. Therefore, no polymer chain can form a stable hydrogen bond on the particle surface, and LbL cannot grow up.

4.2.2 Sensitivity of Low-Q WGM sensors to changes of refractive index in the environment

As explained previously and according to the Eq. 2, the shift in WGM wavelength is induced by changes in at least one of three parameters: the RI of the resonator (n_s), the RI of the environment (n_e) or the optical particle diameter. If no molecule will be adsorbed on the surface, the optical diameter and RI of the particle will not be affected and the peak position will be dependent only on the changes in the RI of the environment. This feature of the WGM method can find a practical application in a continuous analysis of RI of different solutions. Moreover, and unlike the other optical label-free methods able to determine the RI of the solution as SPR, BLI or even High-Q WGM bioassays, the fluorescent Low-Q WGM offers small size and complete separation from the measuring device what in turn allows them to monitor the changes in RI in small cavities e.g. tissues/cells or micro-bioreactors.

In order to determine the sensitivity of Low-Q WGM sensors to changes of RI of environment, the dye-doped PS particles in the nominal size of 10 µm were rinsed with glycerol solutions in the concentration of 1, 2.5, 5, 10, 15 and 20%, measuring continuously the mode shift. After reaching a plateau for each concentration, the glycerol was removed by rinsing with deionized water. The subsequent glycerol solution was added the particles were washed with deionized water. The obtained results are presented in Figure 51.
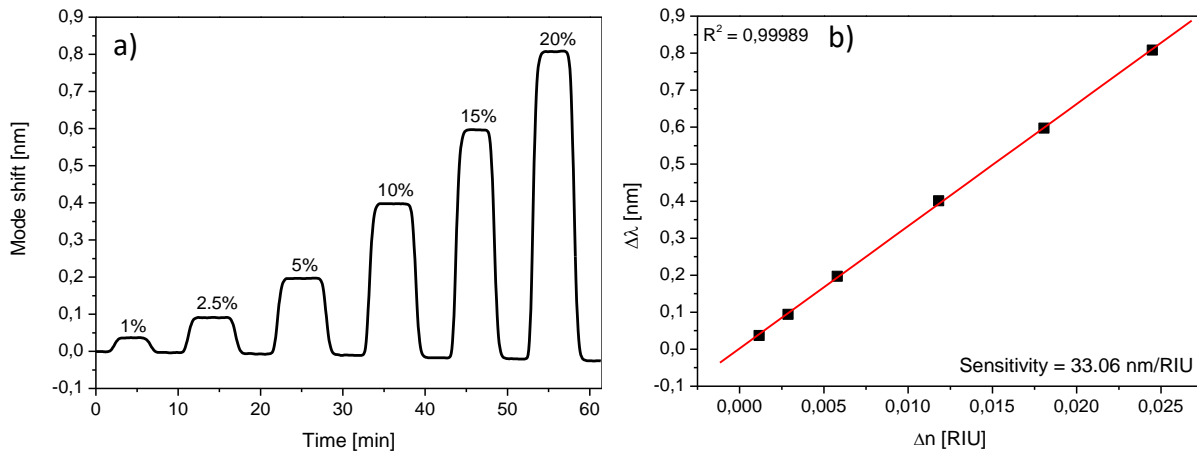
Figure 51. Analysis of the refractive index (RI) by means of WGM detection system: (a) WGM shift as a result of rinsing the sensors with glycerol solutions of different concentrations and (b) WGM shift as a function of changes of RI in the environment.

As shown in Figure 46a, as the concentration of glycerol increases, the WGM shift also increases due to the changes in n_e. Since the glycerol cannot permanently adsorb on the sensor surface, the optical resonator diameter, as well as n_s, will be not affected allowing reverse the WGM wavelength to the initial state by rinsing with water.

Figure 51b presents the WGM shift as a function of changes of RI for glycerol in different concentrations (the RI values of glycerol were taken from L.F. Hoyt[215]). The obtained WGM shift shows a linear relationship to RI values. The sensitivity was determined at 33 nm/RIU (Refractive Index Unit). Therefore, by the spectral resolution of the WGM instrument of 6 pm, the RI changes of 2×10^{-4} can be successfully detected.

4.2.3 WGM-analysis of unspecific adsorption of lysozyme

In order to determine the real sensitivity of developed low-Q WGM microsensors, the WhisperSense instrument was compared with two commonly used and well-established label-free detection systems: QCM (Q-Sense, Biolin Scientific) and SPR (Biacore, GE-Healthcare) by measurement the kinetic adsorption of lysozyme in different concentrations. In this case, three types of sensors were applied: PS particles for WGM, Au-covered glass chips for SPR and Au-covered quartz resonator crystals for QCM. In order to ensure at least similar surfaces they were coated with positively charged polyelectrolyte Polyallylamine (PAH) before the negatively charged lysozyme (PBS buffer, pH 7.4) in different concentrations (1000, 100, 10, 5 and 1 µg/mL) was adsorbed by means of LbL technique. In order to obtain negatively charged

surfaces for the adsorption of the PAH, the gold surface of the Biacore and QCM chips were first modified by using thioglycolic acid (1mM in EtOH) and then coated with PAH. The PS particles were also precoated with PSS and then with PAH. Output data obtained from WGMand QCM (wavelength shift of TM Mode and frequency changes of quartz crystal) were converted to the mass density by using equations 9 and 10, respectively.
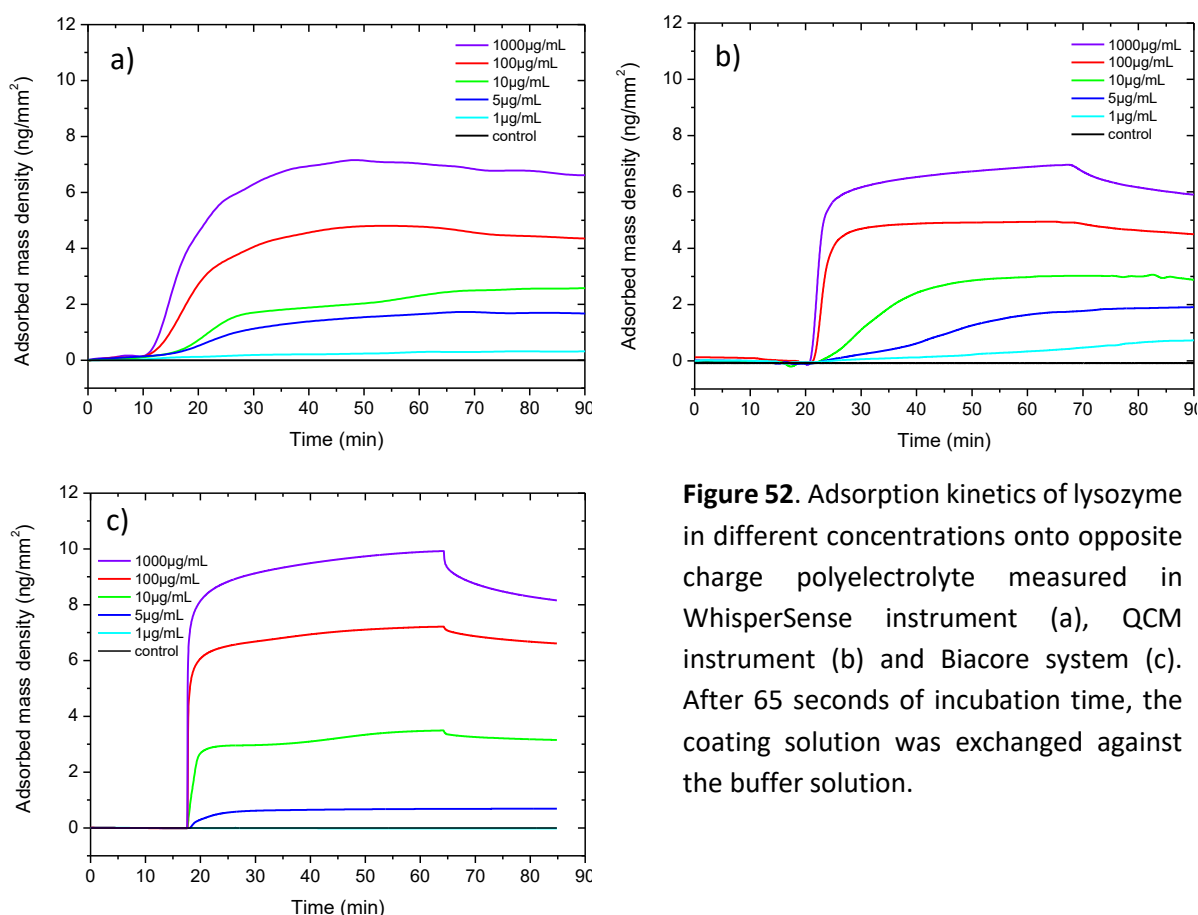
Figure 52. Adsorption kinetics of lysozyme in different concentrations onto opposite charge polyelectrolyte measured in WhisperSense instrument (a), QCM instrument (b) and Biacore system (c). After 65 seconds of incubation time, the coating solution was exchanged against the buffer solution.

It was found, that the minimal detectable concentration of lysozyme adsorption is 1 µg/mL measured in WhisperSense and QCM instrument and 5 µg/mL measured in the Biacore system (Figure 52). However, the adsorption kinetics in Biacore and QCM system is significantly faster than in WhisperSense and shows visible desorption of excess lysozyme during washing with buffer. The reason was the imperfect microfluidic of the WGM experiment, having less real flowrate and mass transport of protein as well as no strong gradient between buffer and coating solutions caused by long transport ways and several traps in dead volumes. The Biacore instrument uses a planar gold chip with tiny microfluidic channels layout ensuring always a high flow rate. An air bubble prevents the intermixing of the coating solution with

the buffer. In contrast, the WGM measurements were performed on micropatterned microfluidic chips with significantly bigger channel dimensions.[50] It leads to slower diffusion of analyte and more flat kinetic adsorption curves.

4.2.4 WGM-analysis of specific biomolecular interactions based on the streptavidin-biotin model

The ultimate test of overall system performance was accomplished by specific detection of a biomolecule. As a straightforward and widely used benchmark model for label-free performance testing, the biotin-streptavidin system was applied here. The low-Q WGM sensors were biotinylated on the surface by using the LbL deposition method with biotin-labeled polyelectrolytes. This simple technique was developed in order to ensure always the same biotinylation degree for each new particle batch. Adding streptavidin to the polyelectrolyte-bound biotin yield a strong coupling and streptavidin-modified beads. On these beads, quite different biotinylated biomolecules like antibodies or oligonucleotide can easily be attached.

In order to achieve the optimal amount of bound streptavidin and reduced non-specific adsorption, the biotinylated LbL film was optimized in view of type, number, sequence, biotinylation degree, and pH of polyelectrolytes. Moreover, the limit of detection of streptavidin for two different sensor sizes was determined. Finally, the studies of kinetic adsorption of the biotinylated antibody onto streptavidin-functionalized WGM particles were performed.

4.2.4.1 Comparison of PAH-biotin and PMAA-biotin

As the first step to study the specific biomolecular interactions in WGM-system based on the streptavidin-biotin model, the influence of biotinylated polyelectrolytes charge on the unspecific binding of streptavidin was investigated. For this purpose, fluorescent PS particles with a nominal diameter of 10 μm were first LbL-coated with two basic bilayers of PSS/PAH. Finally, one layer of biotinylated PMAA was added. One additional PSS layer was coated for assembling the positively charged PAH-biotin.

These preparative steps are followed by the test on the specific binding of streptavidin in the WGM system. Both particle types were introduced into the microfluidic system and left to

sediment into the pre-structured microwells. Afterward, the streptavidin solution was injected into the system (100µg/mL, in PBS buffer), allowing to bind to the LbL-biotinylated sensor particles. The non-specific bound streptavidin molecules were removed by washing the system with acetate buffer (25mM) at pH 4. Subsequently, the free places on the particle surface were passivated with bovine serum albumin (BSA) solution (1mg/mL, in PBS). To prove the success of passivation, BSA injection was repeated once more under the same conditions. The schematic illustration of preparation streptavidin-functionalized WGM particles by using LbL technology with an outer layer of PAH-biotin and of PMAA-biotin is shown in Figure 53. The average response of ten WGM sensors to the biochemical treatment is given in Figure 54.
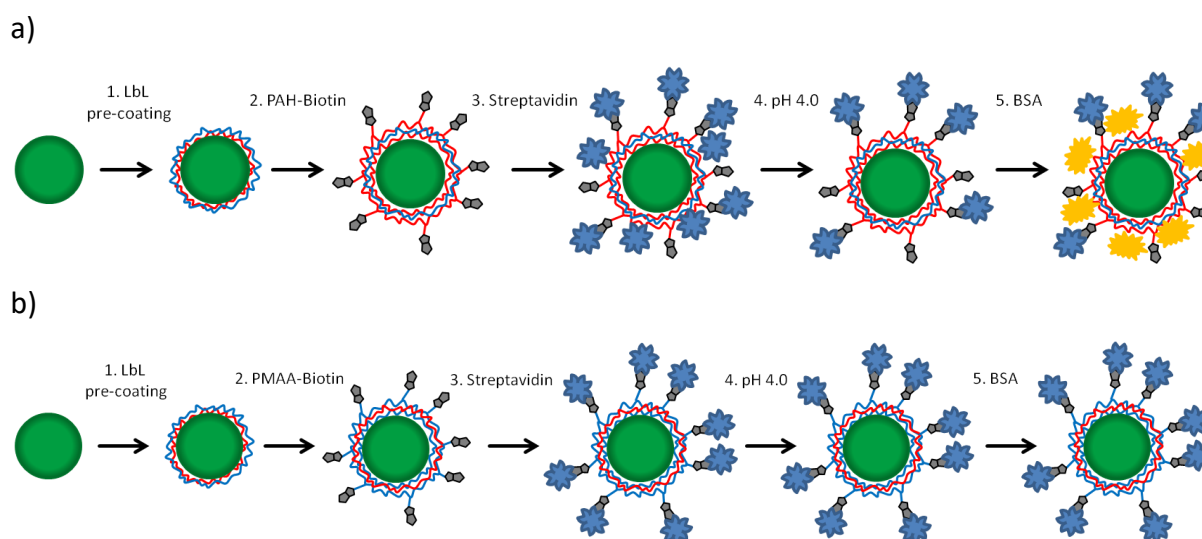
Figure 53. Scheme of the preparation of streptavidin-functionalized WGM particles using two different biotinylated polyelectrolyte types. (a) Particles coated with PAH-biotin as the outermost layer and (b) particles coated with PMAA-biotin as the outermost layer. Noticed that the PAH-biotin approach required additional steps (removing the unspecifically bound streptavidin molecules and blocking with bovine serum albumin (BSA)) to avoid unspecific interactions with further proteins.
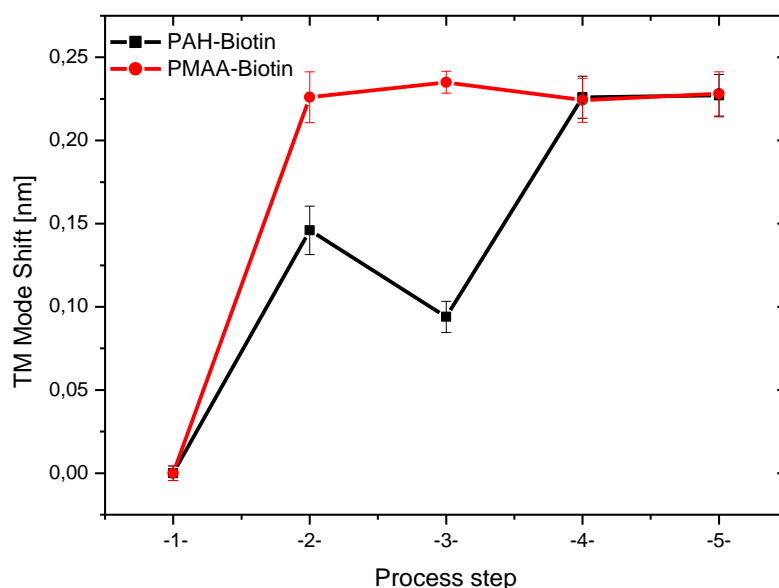
Figure 54 WGM mode shifts as a result of specific and non-specific protein adsorption – comparison of beads coated with PAH-Biotin and PMAA-Biotin. Step #1 – WGM particles in PBS buffer; #2 – same particles in PBS buffer after adsorption of Streptavidin; #3 – after removal of non-specifically bound Streptavidin (in PBS): #4 – after blocking of free adsorption sites with BSA (in PBS); #5 – after second injection of BSA (in PBS).

As can be seen in Figure 54, the injection of streptavidin (step #2) yields different mode shifts depends on the type of biotinylated PE used. Particles coated with PMAA-biotin showed the average mode shift of 225 pm, whereas particles coated with PAH-biotin of 145 pm. The reason can be related to the biotinylation degree of PAH and PMAA. As detailed described in chapter 3.3.3 and 3.3.1, the biotinylation of PAH was performed by direct coupling of NHS-biotin to PAH chains while the biotinylation of PMAA was realized in a two-step reaction. First, the carboxy groups on the PMAA chain were activated with CDI, and then the active intermediate was directly coupled with biotin-hydrazide molecules. As it is known, hydrazides react fast and very efficient with CDI-activated carboxyl groups, forming a stable hydrazone bond.[216] In contrast, the reaction of NHS ester to amine groups is slower and less effective, leading to a lower biotinylation degree of PAH.

As expected, the washing with acetate buffer at pH 4 (step #3) also yields a different signal response. The negative mode shift has been seen only for particles coated with PAH-biotin, while for PMAA-biotin coated particles, no discernable shift was observed. By the passivation of the free binding sites on the sensor's surface (step #4), the PAH-biotin coated particles showed the mode shift of 150 pm while for PMAA-biotin coated particles no significant signal response was detected. The reason for these differences lies in the different charge of

biotinylated PE. In PBS buffer at pH 7.4, the PAH chains are positively charged (pKa of 8.8[217]) whereas the PMAA chains remain mostly negatively charged (pKa of ~6.2[218]). Thus, the negatively charged streptavidin or BSA molecules can unspecifically adsorb only on PAH-coated particles, while on PMAA-coated surface they will be electrostatically repulsed. Therefore, the washing at pH 4 removes the electrostatically bound Streptavidine due to turning its charge to positive. This results in repulsion from the cationic PAH surface and to the release of electrostatically bound streptavidin.

4.2.4.2 Alternative strategies of biotinylation of PMAA

Besides CDI, there are alternative crosslinking routes used to coupling amine-containing molecules to carboxyl-groups such as N,N'-dicyclohexylcarbodiimide (DCC), N,N'-diisopropylcarbodiimide (DIC) or 1-Ethyl-3-(3-dimethylaminopropyl)carbodiimide (EDC). DCC and DIC and CDI are non-aqueous crosslinkers and require a water-free environment to avoid hydrolysis. Therefore, the PMAA sodium salt was transformed into the free acid in order to achieve sufficient solubility in the organic solvents. In contrast, EDC is well-soluble in water and successfully used in a wide range of biochemical coupling reactions.

To find out the influence of the activation mechanism of PMAA on the coupling efficiency of biotin, the activation of PMAA via CDI and EDC were performed. The binding efficiency of both obtained PMAA-biotin samples to fluorescence-labeled streptavidin was investigated PS particles (nominal diameter 10 µm) were LbL-coated with two bilayers of PSS/PAH and with an outermost layer of the PMAA-biotin samples (§ 3.3.1 and §3.3.2), respectively. The labeling efficiency of biotin was determined in CLSM by adsorbing of rhodamin-labeled streptavidin to it. The results are shown in Figure 55. The remarkable higher fluorescence intensity for the EDC activated biotin coupling points to a higher biotin label degree in the sample.
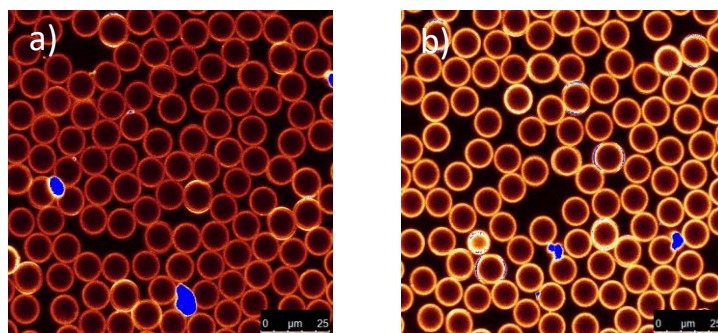
Figure 55 Coupling of streptavidin-sulpho-rhodamin to PMAA-biotin coated PS particles. (a) PMAA-biotin prepared by using CDI and (b) by using the EDC-activation mechanism. The stoichiometric ratio of PMAA to biotin was 1:50 for both types of PMAA-biotin. The fluorescence intensity was measured in CLSM (Laser: 532 nm; PMT: 750V; Zoom: 1.5).

The present study reveals that the PMAA-biotin prepared by EDC-activation can bind a higher amount of streptavidin than PMAA-biotin prepared by CDI-activation. The reason for this difference could be the presence of water traces during the CDI-activation. Hence the subsequent synthesis of PMAA-biotin samples was performed via the EDC activation.

4.2.4.3 Minimization of non-specific binding of streptavidin

As mentioned above, the biggest challenge to produce all kinds of biosensors is obtaining on the surface a high density of specific biomolecules while maintaining a low level of non-specific binding. As demonstrated in section 4.2.3.1, by coating the WGM particles with the outer layer of negatively charged PMAA-biotin instead of positively charged PAH-biotin, the electrostatic adsorption of streptavidin can be significantly reduced. However, there are other types of intermolecular interactions on the multilayer film, such as hydrophobic-hydrophobic interactions, hydrogen-bonds, or van der Waals forces, which can also contribute to the non-specific binding of biomolecules. Nevertheless, an appropriate modification of the LbL-coating with a view of the type, number, sequence, and pH of polyelectrolytes can remarkably diminish those effects.

On this account, PS particles in the nominal diameter of 10 µm were LbL-coated with up to two bilayers of PAH/PSS or PAH/PMAA. Subsequently, all samples were coated with a bilayer of PAH and biotinylated PMAA, whereas control samples were coated with a bilayer of PAH and non-biotinylated PMAA. The fluorescence intensity of bound rhodamine-labeled streptavidin molecules was measured in CLSM and presented in Table 8.

Table 8 Influence of a type, number, and combination of PE on the non-specific and specific binding of rhodamine-streptavidin (λ_{ex} = 535 nm, calculated for PMV settings of 900V)

No.	Pre-coating	Layer						Fluorescence intensity (a.u.)	
		1.	2.	3.	4.	5.	6.	non-specific	specific
1	PSS	PAH	PMAA/ PMAA-Biotin					112	431
2	PSS	PAH	PMAA	PAH	PMAA/ PMAA-Biotin			117	476
3	PSS	PAH	PSS	PAH	PMAA/ PMAA-Biotin			103	360
4	PSS	PAH	PMAA	PAH	PMAA	PAH	PMAA/ PMAA-Biotin	**62**	**472**
5	-	PAH	PMAA	PAH	PMAA/ PMAA-Biotin			168	284
6	-	PAH	PSS	PAH	PMAA/ PMAA-Biotin			168	308
7	-	PAH	PSS	PAH	PSS	PAH	PMAA/ PMAA-Biotin	161	388

Particles coated with the first layer of PSS (samples 1-4) show much lower non-specific binding of streptavidin than particles coated with the first layer of PAH (samples 5-7). It has to be noted here that the PSS chains, besides the negative charge, also has a strong hydrophobic character because of the presence of phenyl rings. This remarkable facility their adsorption on the hydrophobic surface of polystyrene forms a stable basis for subsequent layers.

The non-specific binding of streptavidin can also be reduced by increasing the number of PE layers. Particles coated with up to three bilayers of PMAA/PAH (sample 4) show almost 50% less non-specific binding than particles coated with one bilayer (sample 2). Moreover, it was observed that the LbL film consists of PAH, and PMAA exhibits a better ratio of non-specific/specific binding (sample 2) than LbL film consist of PAH and PSS.

Besides the type, number, and sequence, also the pH value of polyelectrolytes can affect the non-specific binding of biomolecules. As it is known, variations of the pH conditions during assembling of a multilayer structure composed of weak polyelectrolytes have a significant impact on the arrangement, thickness, stability, and charge density of the PE layers.[156]

To find out the optimal pH value of PEs for low non-specific binding of streptavidin, PS particles, in the nominal diameter of 10 µm, were first LbL-coated with one layer of PSS and then with two bilayers of PAH/PMAA at pH of 4.6, 5.1, and 5.6 in different combinations. The

non-specific binding of rhodamine-labeled streptavidin was determined by measuring the fluorescence intensity in CLSM. The results are presented in Table 9.

Table 9 Influence of pH value of polyelectrolytes on the non-specific binding of Streptavidin-Rhodamin measured in CLSM (λ_{ex} = 535 nm, calculated for PMV settings of 900V)

| No. | pH value of PE solutions | | | | Fluorescence intensity of non-specific binding of streptavidin-rhodamine (a.u.) |
	1. PAH	2. PMAA	3. PAH	4. PMAA	
1	5.6	5.6	5.6	5.6	53
2	5.1	5.1	5.1	5.1	114
3	4.6	4.6	4.6	4.6	431
4	5.6	5.6	5.6	5.1	53
5	5.6	5.6	5.6	4.6	46
6	5.6	5.1	5.6	5.1	38
7	5.6	4.6	5.6	4.6	**23**
8	5.6	4.6	5.6	5.6	38

The lowest non-specific binding of streptavidin was obtained for particles coated with PAH at pH 5.6 and PMAA at pH 4.6 (sample 7). Since the carboxyl groups on the PMAA under the pH 4.6 conditions are only half-ionized, the intermolecular repulsions become smaller, caused a significant increase in the film thickness. As a result, the streptavidin molecules can be more effectively separated from the hydrophobic particle surface as well as positively charged PAH layers, which decrease remarkably the number of non-specific interactions.

4.2.4.4 Influence of label degree

Besides suppressing the non-specific binding, a second crucial point in the successful functionalization of the biosensor is obtaining on the surface a high load of target molecules. Generally speaking, the sensor signal is proportional to surface coverage which typically is directly dependent on the size of the bioactive area and the efficiency of the binding event. Therefore, in designing of sensor surface the major effort should be placed on increasing the density of analyte receptors and immobilize them in the right orientation.

The use of biofunctionalized LbL in surface modification allows precisely controlling the number of bioreceptors easily by varying the label degree of PEs. Further, because of the self-mobility of PE chains within the 3D-multilayer film during film deposition[219] and post-assembly,[199] the availability, and orientation of labeled biomolecules can be improved.

To study the influence of the label degree of biotin-PMAA on the adsorbed mass of streptavidin, PS particles in the nominal size of 10 μm, were first LbL-coated with a single layer of PSS and then with a double layer of PAH/PMAA. Finally, the particles were coated with a

bilayer of PAH and PMAA labeled with biotin in a stoichiometric ratio of 1:1; 1:2; 1:5; 1:10; 1:25; 1:50; 1:100; 1:350; 1:500 (defined as the number of biotin molecules to monomers in a polymer chain). To determine the real label degrees of biotinylated PMAA samples the HABA assay was applied.
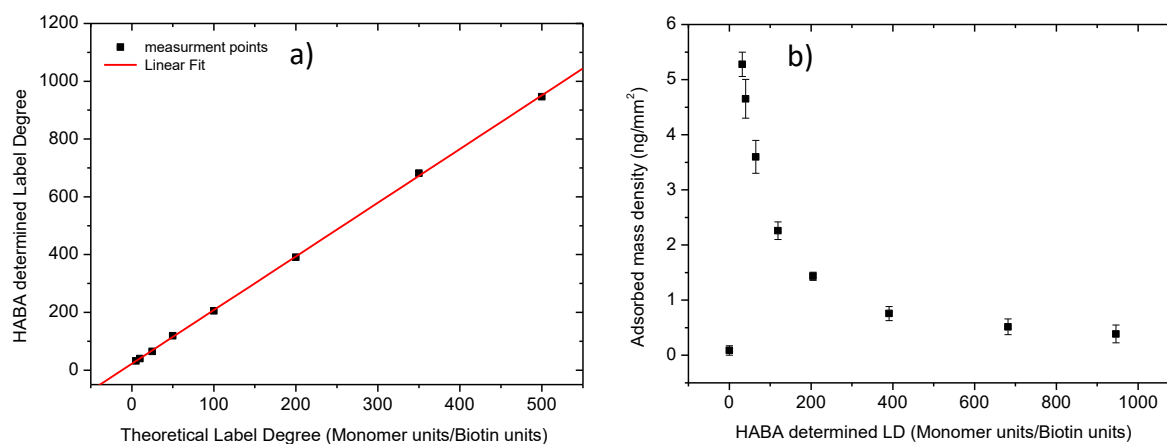
Figure 56. Dependence of theoretical label degree (molar ratio) of Biotin-PMAA and real label degree determined by HABA test (a). WGM shift depends on the label degree of Biotin-PMAA as a result of streptavidin adsorption (b).

As shown in Figure 56, as the number of biotinylated PMAA monomers increases, the mass of adsorbed streptavidin molecules also increases. The maximum saturation of the streptavidin was observed for particles coated with biotin-PMAA in a label degree of 1:5 (real 1:32). For the biotin-PMAA samples in label degrees of 1:1 and 1:2, no experimental data have been obtained because of poor solubility in water.

4.2.4.5 Determination of the limit of detection (LOD)

The most reliable indicator determining the performance of the sensors and the sensing method is the limit of detection (LOD). Following by IUPAC definition, the LOD is referred to as the smallest amount of analyte in the test sample that can be distinguished from the blank value.[220] LOD should not be confused with the term "sensitivity", described the smallest concentration change that the method is capable of detecting or put simple, described the assay's resolution. As shown in paragraph 4.2.2, the sensitivity of the Low-Q WGM system to the changes in n_e was evaluated to 33 nm/RIU, giving the minimal resolution of 2 x 10^{-4} RI.

However, in the case of specific biomolecular interactions, the LOD is affected by changes in n at particle/environment boundary ($n_{effective}$) as well as particle diameter.

The LOD of specific streptavidin-biotin system was determined for the low-Q WGM sensors in the nominal size of 7 µm and 10 µm. Dye-doped PS particles were first LbL-coated with two bilayers of PSS/PAH film and then with a single layer of biotinylated PMAA (real LD 1:32). The control sample was coated with non-biotinylated PMAA. The average TM mode shift for ten particles of each size was measured in response to incubation with streptavidin in concentration of 1000, 100, 10, 1, 0.7, 0.3, 0.1, 0.05, 0.01 and 0.001 µg/mL in PBS buffer at pH 7.4 (18900, 1890, 189, 18.9, 12.96, 5.66, 1.89, 0.943, 0.189, 0.0189 nM, respectively). The results are shown in Figure 57.

As expected and according to the fundamentals, the total mode shift of WGM sensors in the size of 7 µm is bigger than for the sensors in the size of 10 µm. However, as the concentration of streptavidin decreases, the difference in the mode shift between the different sensor sizes also decreases. This effect can be related to the dissociation equilibrium constant (K_D) described as the ratio of on-rate constant (k_{off}) and off-rate constant (k_{on}) of ligand:

$$K_D = \frac{k_{off}}{k_{on}} = \frac{[R][L]}{[RL]} \tag{11}$$

Here, [R] is the concentration of unbound receptor, [L] is the concentration of the unbound ligand, and [RL] the concentration of receptor-ligand complexes.

To put it more illustrated, when the ligand concentration equals the K_d, the response is in a half-maximum. As can be seen, the K_d is similar for both sensor sizes. This is because both association and dissociation rate constants are independent of the analyte concentration and the number of ligand binding sites. Therefore, when the saturation decreases the higher mode shift of small sensors is no longer an advantage.
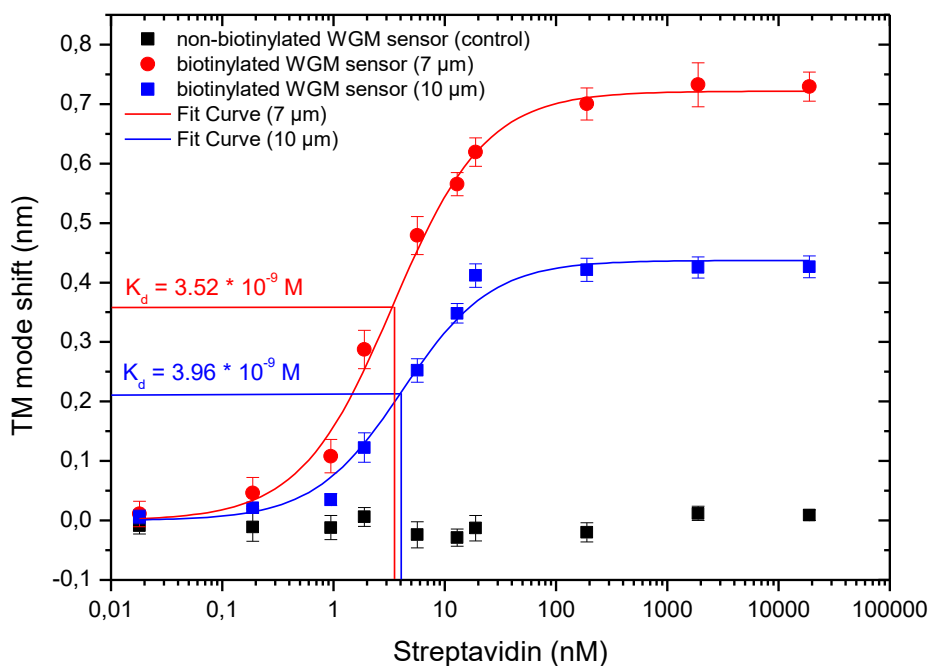
Figure 57. Determination the Limit of Detection (LoD) of low-Q WGM detection system for streptavidin

The minimal detectable concentration of streptavidin was found at 0.2 nM. This is a good result and can be compared to the other optical label-free biosensing method as SPR,[222] microring resonators (MRR)[222] or RifS.[223]

4.2.4.6 Specific binding of biotinylated antibody on streptavidin-modified low-Q WGM microbeads

Streptavidin-coated biosensors can be used to capture biotin-labeled conjugates including antibodies, antigens, PCR products or DNA/RNA strands. In this work, the binding capacity of streptavidin-functionalized WGM particles was studied by measuring the adsorption kinetic and adsorbed mass density of biotinylated antibody.

Dye-doped PS beads were first coated with a single layer of PSS and then with two bilayers of PAH/PMAA. Finally, the beads were coated with a single bilayer of PAH/biotin-PMAA (real LD: 1:32). A control sample was assembled with a single bilayer of PAH/PMAA. The WGM shift was measured in response to injection of streptavidin (100 µg/mL in PBS buffer pH7.4) and biotinylated rabbit-IgG (10 µg/mL in PBS buffer pH7.4). The kinetic adsorption obtained in the WhisperSense instrument was presented in Figure 58.
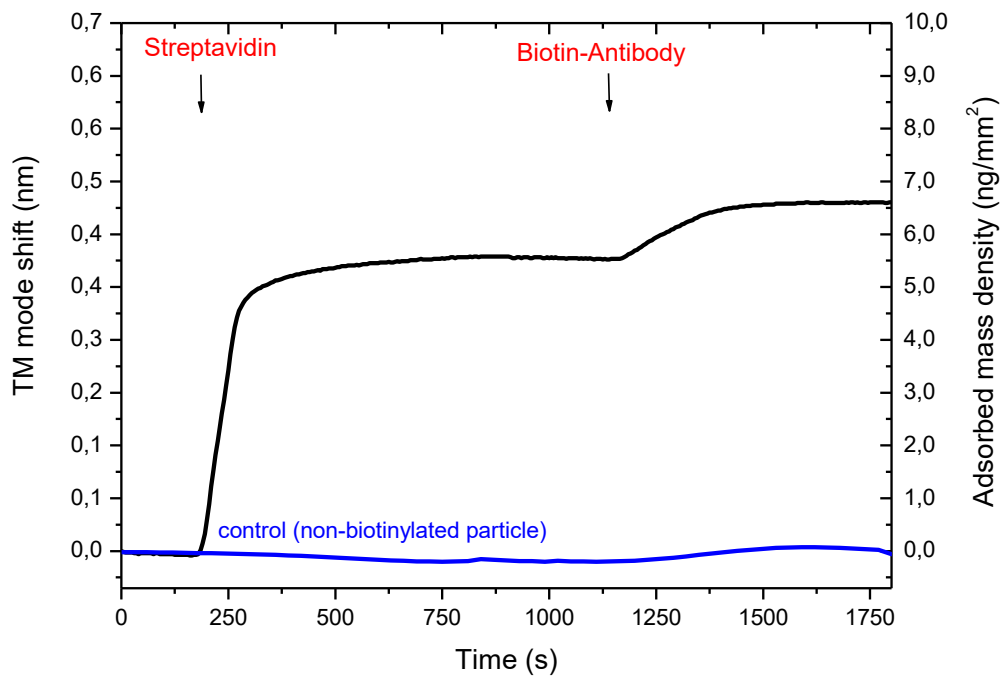
Figure 58. TM mode shift and calculated adsorbed mass density as a result of specific adsorption of streptavidin and biotin-labeled rabbit-IgG on biotinylated WGM sensor. Particle coated with PMAA in the outer layer has been used as a reference (blue line).

The biotinylated low-Q WGM particle shows a considerable WGM shift by attachment of streptavidin. The full saturation at the adsorbed mass density of 5.5 ng/mm^2, was obtained after a rinsing time of 3 min by a flow rate of 40 μL/min. In contrast, the adsorption kinetics of biotinylated rabbit-IgG was significantly slower (the full saturation was reached after 6 min) and the adsorbed mass density was lower (1.5 ng/mm^2). The reason lies probably in the accessibility of the binding sites of streptavidin. As is well-known, streptavidin is a tetramer with four binding sites of biotin, each with an equal affinity. As the biotinylation degree of PMAA on the sensor increasing, most of the available binding sides of adsorbed streptavidin can be occupied limiting the further binding of the biotinylated ligands. Reduction of the density of biotin on the particle surface can lead to unlocking more binding sites of streptavidin, finally increasing the number of captured biotin-molecules. As expected and according to the previous results, for the control sample no discernible shift in response to rinsing with streptavidin and biotinylated antibody was detected.

4.2.5 WGM-detection of solvents

Besides the analysis of the specific interaction between various biomolecules, the WGM sensors have been also used to detect a variety of chemical species including organic solvents, alcohols, gases, ions, and even explosives.[106] Thanks to the ability of continuous and sensitive detection of different chemical compounds in real-time, the WGM sensors can be applied in many areas related to environmental protection, food safety or human health as for example the analysis of the quality of drinking water or monitoring the air pollutions.

In general, the chemical specificity of the WGM sensor is achieved by coating the particle surface with a chemoselective polymer which can swell as the specific chemicals adsorb.[106] The changes in the particle diameter/RI could be then measured by tracking the WGM shift. However, in unspecific detection of the organic solvents or alcohols, the swelling effect of the sensor can be also reached by using the polymeric particles as for example polystyrene, polymethylmethacrylate or polydimethylsiloxane beads.[224]

In order to demonstrate the ability of the developed Low-Q WGM beads to detect the water pollution by the organic solvents, two aqueous solutions of polar solvents: tetrahydrofuran (THF) and acetone in the concentration of 0.1% and an aqueous solution of non-polar toluene in the concentration of 0.05 and 0.005 % were investigated. For that, the native, dye-doped PS particles in the nominal size of 10 µm were fixed in the microfluidic wells-array and rinsed with the different solvents at continuously monitoring of the WGM position. Finally, the particles treated with THF and acetone were rinsed with deionized water in order to check the level of reversibility of the process. The results were shown in Figure 59 and Figure 60.
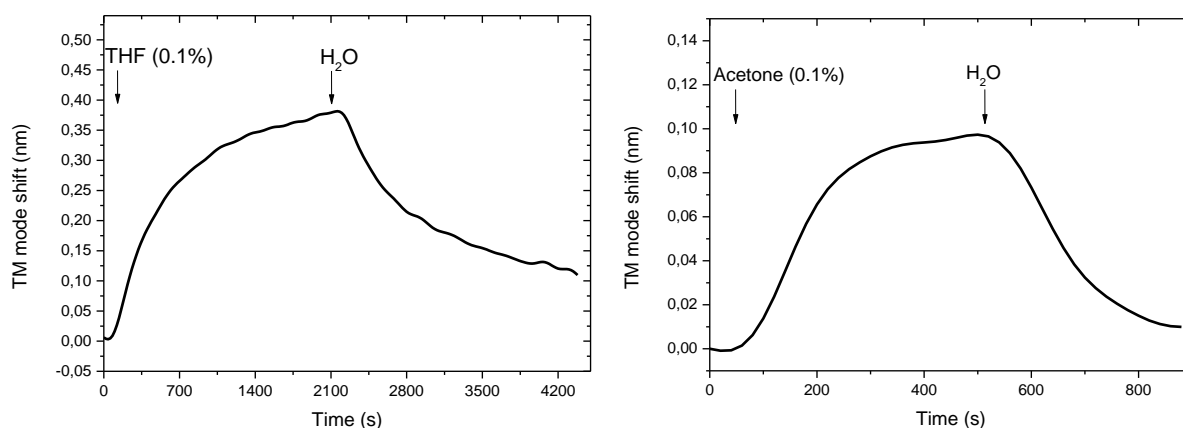
Figure 59. Real-time WGM shift responses to washing the sensors with the polar solvents: (a) tetrahydrofuran (THF, 0.1% aqueous solution) and (b) acetone (0.1% aqueous solution).

By washing the PS particles with THF and acetone in the concentration of 0.1 % a significant shift of TM mode was observed. However, in the case of THF, the total mode shift was around four times bigger (370 pm) than in the case of acetone (100 pm). The reason for this difference is related to the partition coefficient of the solvents. Since THF is more hydrophobic than acetone ($log_{POW \ of \ THF}$ = 0.46 and $log_{POW \ of \ acetone}$ = -0.24,)[225] it can easier diffuse from water solution into the polystyrene, what leads in turn to a greater swelling and as consequence diameter of WGM sensors. However, when an equilibrium of solvent distribution between polystyrene and water is reached, particles stop swelling and no change in the WGM wavelength can be further observed. Rinsing the particles back with pure water allows removing the polar solvents and reversed the WGM shift.
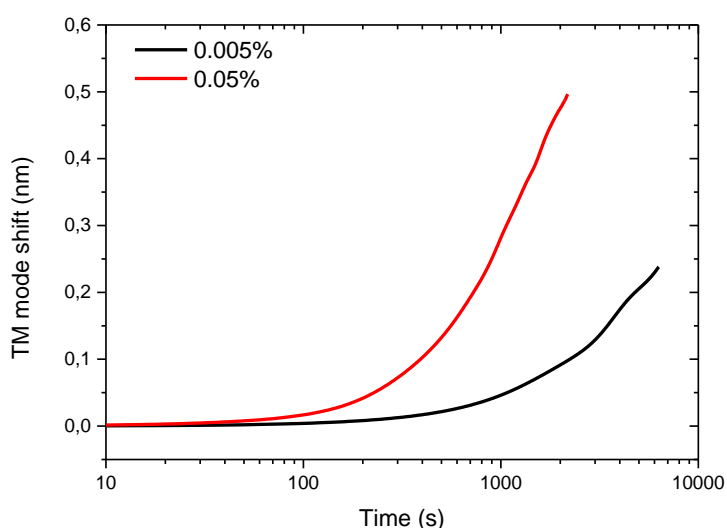
Figure 60. WGM shift responses to washing the sensors particles with aqueous solutions of toluene in different concentrations (0.005 and 0.05%).

In contrast to the experiments with THF and acetone, by washing the PS particles with toluene solutions in both concentrations, a continuous increase of mode shift was detected. Since the partition coefficient of toluene is very high (log_{POW} = 2.73) its affinity to hydrophobic polystyrene is significantly greater than to water. This leads to a continuous swelling of the particle and change in the WGM wavelength so long until the toluene molecules are present in the environment. As mentioned, this special feature of the Low-Q WGM microsensors can be very useful for the continuous analysis of contaminations of organic solvents in drinking water systems.

4.2.6 Summarizing discussion

In this part of the thesis, the sensing performance of the developed low-Q WGM sensors was studied by means of:

1) measuring the unspecific adsorption of polyelectrolytes driven by electrostatic and hydrogen bond formation,

2) measuring the unspecific binding of lysozyme,

3) analyzing the specific interactions between biotin and streptavidin,

4) detection of water contaminations by organic solvents

In the case of unspecific adsorption of PEs based on electrostatic attraction, the effect of salt concentration on the growth regime of PAH/PSS and PDADMAC/PSS multilayer films was studied. The WGM results showed that independently on the salt concentration, the LbL film consisted of PAH/PSS layers grows linear whereas the PDADMAC/PSS film grows linear in the presence of 0.2M NaCl but exponential 1.5M NaCl. As reported in the literature, [162,211] the exponential growth regime of LbL film in the presence of high salt concentration can be related to the strong hydration and "in-and-out" diffusion of at least one of PEs during assembling of each bilayer. Therefore, the exponential growth film can be rather considered as the gel of polyanions/polycations complexes than precisely structured LbL film.[162] The values obtained by the WGM method for the LbL film thickness and adsorbed mass density of polyelectrolytes confirmed the previous results of Elzbieciak-Wodka et al. performed by QCM and ellipsometry.[162]

The hydrogen-bonded PVP/PMAA films were investigated taking into account the effect of high pH value on the film stability as well as the effect of polymer concentration on the layers thickness. As expected, rinsing the PVP/PMAA film with borate buffer at pH 8 leads to the complete degradation of the film and decomposition in its constituents. This is because the carboxy groups of PMAA ionizing negatively, losing at the same time the ability to accept an electron pair from a lactam group of PVP. The study of the effect of PVP/PMAA concentration on the layers thickness revealed that by the polymer concentration in the range of 1000-10 µg/mL the film grows linear and no significant difference in the layer thickness can be observed. However, as the concentration of the polymer decreased to 1 µg/mL, the film stops growing causing no shift of WGMs. The reason can be mainly related to the high desorption

constants of PVP/PMAA but also to the large dimensions of the microfluidic channel. The large cell capacity decreases the flow rate and makes mass transport of polymer more difficult.

The comparison of the WGM analytical tool with two well-established label-free detection platforms: QCM and SPR, was performed by measuring the unspecific adsorption kinetics of lysozyme in different concentrations. The obtained results showed a similar limit of detection for all three techniques. However, due to larger capacity and lower local flow rate of WGM microfluidic cell, the adsorption kinetics of lysozyme is significantly slower than in the case of QCM and SPR method.

The analysis of the specific biomolecular interactions between streptavidin and biotin was conducted for increasing the amount of bound streptavidin and reduce the non-specific adsorption. For this purpose, the LbL coating used to biotinylation of the sensor's surface was optimized in case of the type, number, sequence, biotinylation degree, and pH of polyelectrolytes. The lowest non-specific binding of streptavidin was found by the deposition of two bilayers of PAH/PMAA film at pH 5.6 and 4.6, respectively. Pre-coating the polystyrene beads with hydrophobic PSS-layer allowed improving the adsorption of subsequent layers and reducing the non-specific binding. The biotinylation of the sensor surface was performed by coating as the outermost layer with PAH-biotin and PMAA-biotin. PAH was found to be less suitable polyelectrolyte for biotinylation of PS particles than PMAA because it requires additional steps e.g. blocking the free places, to avoid the non-specific binding of molecules. The maximum occupancy rate of streptavidin was achieved for particles coated with PMAA-biotin with the label degree of 32:1 (number of polyelectrolyte monomers: biotin). Further increasing of the label degree of PMAA-biotin led to solubility problems due to the nonpolar character of biotin. The studies of the detection limit of streptavidin for WGM beads in different sizes revealed that independently of sensor diameter the minimal detectable concentration is constant and equal ~ 0.2nM. This result can be compared to the other optical label-free biosensing method as SPR, microring resonators (MRR) or RifS. Specific binding of the biotinylated antibody to the streptavidin-modified low-Q WGM beads showed a considerable WGM shift. However, the adsorption kinetics was significantly slower and the adsorbed mass density lower than for streptavidin. The reduction of the biotinylation degree of PMAA can allow increasing the distance between streptavidin molecules and unlock occupied binding sites.

The Low-Q WGM microsensors were also used to detect the low water pollutions by organic solvents. For the water samples contaminated by tetrahydrofuran and acetone, the WGM shift was observed until the equilibrium of solvent distribution between polystyrene and water was reached. Since both organic solvents have a polar character the swelling process of the particles could be reversed by rinsing with water. In contrast, the water samples contaminated by toluene in the concentration of 0.05 and 0.005%, a continuous WGM shift was detected. The reason lies in the strong hydrophobic character and high partition coefficient of toluene. As long as toluene will be present in the environment, the polystyrene sensors will swell results in the shift of WGM. This feature of polymer WGM microsensors can find a practical application for continuous monitoring of water quality in the water installations.

5 Conclusions

The main objective of this work was to develop and characterize the low-Q WGM microsensors that can be successfully used in label-free detection of specific biomolecules. Hereafter, more important conclusions are listed.

1. The best-suited particle material type to produce low-Q WGM microsensors is polystyrene because of high signal intensity and narrow bandwidth. The studies using atomic force microscopy, scanning electron microscopy and whispering gallery modes biosensing confirmed their smooth surface and high refractive index.

2. WGM particles synthesized by seeded-growth polymerization showed high WGM performances, monodispersity and controllable particle size.

3. The optimal sensor size range was found between 8.5-11 μm due to higher signal intensity, narrower bandwidth, and accessible data processing.

4. Coumarin 6 demonstrated best properties by means of WGM excitation in PS particles, including high resistance to photobleaching, short adsorption/emission wavelength, hydrophobicity and high values of molar extinction coefficient and quantum yield.

5. Immobilization of fluorescent dyes by the LbL technique onto non-fluorescent PS particles yields highly qualitative WGM sensors with narrow bandwidth, low background signal, and easy post-modification possibility.

6. Compared to the other label-free optical system such SPR or ellipsometry, Low-Q WGM system show very low sensitivity for changes in temperature – 0.004 -0.007 nm/°C.

7. The studies of formation the LbL films performed in the WGM sensing system showed the dependence between salt concentrations and layer thickness and confirmed the previous results from quartz crystal microbalance and ellipsometry.

8. The studies of unspecific adsorption of lysozyme in different concentrations performed in surface plasmon resonance and whispering gallery modes sensing system showed slightly better sensitivity of WGM but significantly slower adsorption kinetics than SPR and QCM.

9. The low-Q WGM microsensors can be successfully bio-functionalized by using of streptavidin-biotin interactions. The limit of detection of streptavidin was measured by the concentration of 0.2 nM.

10. Low-Q WGM polymer microsensors can be also applied in continuously analysis of water pollutions by organic solvents.

Based on the obtained results, it can be concluded that developed low-Q WGM microparticles are promising, new-generation biosensors to be used in label-free detection of any types of biomolecules such as proteins (including antibodies), DNA/RNA, viruses, bacteria or even drugs.

6 References

1. C. Kuepper et al. *Scientific Reports* **2018**, 8.

2. S. Lee, H. Chon, J. Lee, et al*. Biosens. Bioelectron.* **2014**, 51.

3. M. Miyara et al. *PLoS ONE* **2018,** 13(8).

4. C. Markwalter, I. Jang, R. Burton, G. Domingo, D. Wright, *Anal. Biochem.* **2017**, 534.

5. G. Anderson, J. Liu, D. Zabetakis, P. Legler, E. Goldman, *J. Immunol. Methods* **2017**, 442.

6. A. Washburn, M. Luchansky, A. Bowman, R. Bailey *Anal. Chem.* **2010**, 82.

7. R. Rich, D. Myszka, *Curr. Opin. Biotechnol.* **2000**, 11, 54–61.

8. Y. Bunimovich et al., *J. Am. Chem. Soc.* **2006**, 128, 16323–16331.

9. N. Backmann et al., *Proc. Natl Acad. Sci. USA* **2005**, 102, 14587–14952.

10. N. Kim, D-K Kim, Y-J Cho, *Sensor. Actuat. B-Chem.* **2009**, 143, 444–448.

11. J. N. Anker et al, *Nat. Mater.* **2008**, *7*, 442.

12. V. Kravets, A. Kabashin, W. Barnes, A. Grigorenko, Chem Rev. 2018, 118, 5912-5951

13. J. Conception et al., *Comb. Chem. High Throughput Screen* **2009**, 12, 791.

14. J. Piehler, A. Brecht, K. E. Geckeler, G. Gauglitz, *Biosen. and Bioelectro.* **1996**, 11, 579.

15. P. Anton Van Der Merwe, *Protein-ligand interact.: hydrodyn. and calorim.* **2001**, 1, 137-170.

16. M. J. Linman, A. Abbas, Q. Cheng, *Analyst* **2010**, 135, 2759–2767.

17. A. Otto, *Z. Physik* **1968**, 216, 398-410.

18. E. Kretschmann, H. Raether, *Z. Naturforsch*. **1968**, 23A, 2135-2136.

19. K. Tiefenthaler, W. Lukosz, *Opt. Lett.* **1984**, 9(4), 137-139.

20. R. P.H. Kooyman, "Physics of Surface Plasmon Resonance," 2008, ISBN 978-0-85404-267-8

21. R. C. Jorgenson, S. S. Yee, *Sens. and Acruofors* **1993**, 12, 213-220.

22. J. H. Ahn, *Opt. Express* **2012**, 20 (19), 21729.

23. A. Rothen, *Rev. of Scient. Instrum.* **1945**, 16, 26.

24. C. Cobet, *"Ellipsometry: A Survey of Concept"* **2014**, 52, Springer.

25. M. Losurdo, K. Hingerl, *"Ellipsometry at the nanoscale"* **2013**, Springer.

26. *www.jawoollam.com*

27. B. Garipcan, M. Oğuzhan Çağlayan, D. Gökhan, in "*New Perspectives in Biosensors Technology and Applications*," (Ed. P.A. Serra), Intech **2011**, Ch. 9

28. H-M Schmidt, A. Brecht, J. Piehler, G. Gauglitz, *Biosens. Bioelectron.* **1997**, 12(8), 809-816.

29. C. Hänel, G. Gauglitz, *Anal. Bioanal. Chem.* **2002**, 372, 91–100.

30. B. P. Möhrle et al., *Anal. Bioanal. Chem.* **2006**, 384, 407–413

31. J. Piehler, A. Brecht, K. E. Geckeler, and G. Gauglitz, *Biosens. and Bioelect.* **1996**, 6-7, 579-590

32. X. Lu et al., *Engineer. Med. and Biol Soc.* **2001**, Proceedings of the 23rd Annual International Conference of the IEEE, 3.

33. K. Kröger, A. Jung, S. Reder, G. Gauglitz, *Anal. Chim. Acta* **2002**, 469, 37.

34. Y.Kurihara, T. Sawazumib and T. Takeuchi, *Analyst* **2014**, 139, 6016

35. V. Shabardina et al., *Biophys. J.* **2016**, 110, 2710–2719.

36. https://www.fortebio.com/octet-platform.html

37. J. Conception et al., *Comb. Chem. High Throughput Screen.* **2009**, 12(8), 791-800.

38. A. Sultana, J.E. Lee, *Curr. Protoc. Protein Sci.* **2015**, 79, 1-19.

39. F. Ylera et al., *Analy. Biochem.* **2013**, 441, 2.

40. X. Xiong et al., *Nature* **2013**, 499, 496–499.

41. C. A. Wartchow, *J. Comput. Aided Mol. Des.* **2011**, 25, 669–676.

42. G. Righini et al., *Rivista del Nuovo Cimento* **2011**, 34, 435-488.

43. F. Vollmer, S. Arnold, *Nature Meth.* **2008**, 5(7).

44. M. Himmelhaus, S. Krishnamoorthy, A. François, *Sensors* **2010**, 10, 6257-6274.

45. A. Oraevsky, *Quantum Electronics* **2002**, 32, 377-400.

46. M. Michihata, T. Hayashi, A. Adachi, and Y. Takaya, *CIRP Annals* **2014**, 63(1), 469-472.

47. F. Vollmer and L. Yang, *Nanophotonics* **2012**, 1, 267-291.

48. J. Topolancik, F. Vollmer, *Biophys. J.* 2007, 92, 2223–2229.

49. A. François, M. Himmelhaus, *Sensors* **2009**, 9, 6836-6852.

50. R. Bischler, M. Olszyna, M. Himmelhaus, and L. Dähne, *Eur. Phys. J. Spec. Top.* **2014**, 223, 2041–2055.

51. S. Pang, R. E. Beckham, and K. E. Meissner, *Appl. Phys. Lett.* **2008**, 92, 2–4.

52. A. Bozzola, S. Perotto, and F. De Angelis, *Analyst, Royal Society of Chemistry* **2017**, 142, 883-898.

53. M. Kuwata-Gonokami, K. Takeda, *Opt. Mate.* **1998**, 9, 12-17.

54. M. L. Gorodetsky, A. A. Savchenkov, and V. S. Ilchenko, *Opt. Lett.* **1996**, 21, 453-455.

55. S. Arnold, F. Vollmer, *Nat Methods,* **2008**, 5(7)

56. K. Poetter, E. Nuhiji, P. Mulvaney, US Patent **2011**.

57. D. Melnikau et al. *Opt. Express.* **2011**, 19 (22), 22280-22291.

58. R. Madugani et al., *Opt. Lett.* **2012**, 37, 4762–4764.

59. R. Zeltner, F. Sedlmeir, G. Leuchs, and H. G. L. Schwefel, *Eur. Phys. J. Spec. Top.* **2014**, 223, 1989–1994.

60. L. Yu and V. Fernicola, *Rev. Sci. Instrum.* **2012**, 83, 094903.

61. D. L. Credon et al., *Appl. Phys. Lett.* **2011**, 98, 222903.

62. A. A. Savchenkov et al., *Phys. Rev.* **2004**, 70, 051804(R).

63. V. S. Ilchenko et al., *Phys. Rev. Lett.* **2004**, 92, 043903.

64. P.Y. Bourgeois, et al., Frequency Control Symposium **2007.**

65. J. Park et al., *Adv. Opt. Mater* **2014**, 2, 711-717.

66. M. A. Foster et al., *Opt. Express* **2011**, 19, 14233-14239.

67. X. Lu, J. Y. Lee and P. X.-L. Feng, *Appl. Phys. Lett.* **2014**, 104, 181103.

68. T. Beck et al., *Proc. SPIE* **2011**, 7888, 78880A.

69. L. Rayleigh, *Philos. Mag. 1910*, 20**,** 1001.

70. L. Rayleigh, *Scientific Papers 1912*, 5**,** 617.

71. G. Mie, *Ann. Phys. 1908*, 330, 377-445.

72. P. Debye, *Ann. Phys. 1909*, 30, 57–136.

73. R.D. Richtmyer, *J. Appl. Phys.* **1939**, 10, 391.

74. C. G. B. Garrett, W. Kaiser, and W. L. Bond, *Phys. Rev.* **1961**, 124, 1807–1809.

75. H.M. Tzeng, K.F. Wall, M.B. Long and R.K. Chang, *Opt Lett.* **1984**, 9(11), 499-501.

76. A. Biswas, H. Latifi, R.L. Armstrong, R.G. Pinnick, *Opt Lett.* **1989**, 14(4), 214-6.

77. V.B. Braginsky, M.L. Gorodetsky, V.S. Ilchenko, *Phys. Lett. A* **1989**, 137, 393–397.

78. J.D. Eversole, H.B. Lin, C.D. Merritt and A.J. Campillo, *Appl. Spectrosc.* **1994**, 48, 373–381.

79. A. Serpengüzel, S. Arnold and G. Griffel, *Opt. Lett.* **1995**, 20, 654-656.

80. S. Arnold et al., *Opt. Lett.* **2003**, 28, 272–274.

81. H. Ghali et al., *Biosensors* **2016**, 6, 20.

82. J.T. Gohring, X. Fan, *Sensors* **2010**, 10(6), 5798–5808.

83. F. Vollmer, S. Arnold, D. Keng, *Proc. Natl. Acad. Sci. USA* **2008**, 105, 20701–20704.

84. T. Lu, *Proc. Natl. Acad. Sci. USA* **2011**, 108, 5976–5979.

85. M.D. Baaske, M.R. Foreman, F. Vollmer, *Nat. Nanotechnol.* **2014**, 9, 933–939.

86. J. Su, A.F.G. Goldberg, B.M. Stoltz, *Light Sci. Appl.* **2016**, 5, e16001.

87. J. Su, *ACS Photonics* **2015**, 2, 1241–1245.

88. J. Su, *J. Vis. Exp.* **2015**, 106, e53180.

89. V.R. Dantham et al., *S. Nano Lett.* **2013**, 13, 3347–3351.

90. Y. Wu, D. Zhang, P. Yin, and F. Vollmer, *Small* **2014**, 10, 2067-2076.

91. A. Ashkin, J. M. Dziedzic, *Appl. Opt.* **1981**, 20, 1803–1814.

92. P. Chyek, V. Ramaswamy, A. Ashkin, and J. M. Dziedzic, *Appl. Opt.* **1983**, 22, 2302–2307.

93. C.-H. Dong et al., *Appl. Phys. Lett.* **2011**, 94, 231119.

94. B.-B. Li et al., *Appl. Phys. Lett.* **2010**, 96, 251109.

95. T. Ioppolo, M. V. Ötügen, *J. Opt. Soc. Am. B* **2007**, 24, 2721–2726.

96. T. Ioppolo et al., *Appl. Opt.* **2008**, 47, 3009–3014.

97. M. Himmelhaus, A. Francois, *Biosens. Bioelectron.* **2009**, 25, 418–427.

98. T. Ioppolo, U. Ayaz, M. V. Otügen, *Opt. Express* **2009**, 17, 16465–16479.

99. T. Ioppolo, J. Stubblefield, M. V. Ötügen, *J. Appl. Phys.* **2012**, 112, 044906.

100. M.L. Gorodetsky, V.S. Ilchenko, *J. Opt. Soc. Am. B Opt. Phys.* **1999**, 16, 147–154.

101. A. Matsko et al., *IPN Progress Report, Citeseer* **2005**, 42, 1-51.

102. S. M. Spillane, T. J. Kippenberg, O. J. Painter and K. J. Vahala, *Phys. Rev. Lett.* **2003**, 91, 043902.

103. N. Acharyya, G. Kozyreff, *Phys. Rev. Applied* **2017**, 8, 034029.

104. B.E. Little, J.P. Laine, H.A. Haus, *J. Lightwave Technol.* **1999**, 17, 704–715.

105. V.S. Ilchenko, X.S. Yao, L. Maleki, *Opt. Lett.* **1999**, 24, 723–725.

106. J. Su, *Sensors* **2017**, 17, 540.

107. Y. Lan, V. Kerry, *Opt. Lett.* **2003**, 28, 592–594.

108. S. Arnold et al., *Opt. Express* **2009**, 17, 6230-6238.

109. A. Weller, F.C. Liu, R. Dahint, and M. Himmelhaus, *Appl. Phys. B-Lasers Opt.* **2008**, 90, 561–567.

110. A. Francois, M. Himmelhaus, *Appl. Phys. Lett.* **2009**, 94, 031101.

111. H.K. Hunt, C. Soteropulos, A.M. Armani, *Sensors* **2010,** 10, 9317–9336.

112. L. He et al., *Nat. Nano.* **2011**, 6, 428–432.

113. T. Lu et al., *Proc. Natl. Acad. Sci. USA* **2011**, 108, 5976–5979.

114. M. Ghulinyan et al., *Opt. Express* **2008**, 16, 13218-13224.

115. R.W. Boyd, J.E. Heebner, *Appl Optics* **2001**, 40, 5742–5747.

116. A. Schweinsberg et al., *Sens. Actuator B-Chem.* **2007**, 123, 727–732.

117. T. Wienhold et al., *Lab Chip* **2015**, 15, 3800-3806.

118. M. Iqbal et al., *IEEE J. Sel. Top Quantum Electron* **2010**, 16, 654–661.

119. C. Delezoide et al., *IEEE Photonics Technol. Lett.* **2012**, 24, 270–272.

120. A. Ksendzov, Y. Lin, *Opt. Lett.* **2005**, 30, 3344–3346.

121. A. Yalcin et al., *IEEE J. Sel .Top Quantum Electron* **2006**, 12, 148–155.

122. I.M. White, H. Oveys, X. Fan, *Opt. Lett.* **2006**, 31, 1319–1321.

123. M. Pollinger, D. O'Shea, F. Warken, and A. Rauschenbeutel, *Phys. Rev. Lett.* **2009**, 103, 053901-1–4.

124. R. Henze, T. Seifert, J. Ward and O. Benson, *Opt. Lett.* **2011**, 36, 4536–4538.

125. M. Sumetsky, Y. Dulashko, R.S. Windeler, *Opt. Lett.* **2010**, 35, 898–900.

126. A. Watkins, J. Ward, Y.Q. Wu and S.N. Chormaic, *Opt. Lett.* **2011**, 36, 2113–2115.

127. J. Scheuer, M. Sumetsky, *Laser Photon Rev*. **2011**, 5, 465–478.

128. M. Sumetsky M., *Opt Express* **2004**, 12, 2303–2316.

129. F. Xu, P. Horak, G. Brambilla, *Opt Express* **2007**, 15, 7888–7893.

130. L. Collot et al., *Europhys. Lett*. **1993**, 23, 327–334.

131. F. Vollmer et al., *Appl. Phys. Lett.* **2002**, 80, 4057–4059.

132. Y. Wu, D. Zhang, P. Yin, and F. Vollmer, *Small* **2014**, 10, 2067-2076.

133. M. Iqbal, *IEEE J. Sel. Top Quantum Electron* **2010**, 16, 654–661.

134. K. De Vos et al., *Opt. Express* **2007**, 15, 7610–7615.

135. K. De Vos et al., *Opt. Express* **2007**, 15, 7610–7615.

136. M. Mancuso, J.M. Goddard, D. Erickson, *Opt. Express* **2012**, 20, 245–255.

137. S.Y. Cho, N.M. Jokerst, *IEEE Photonics Technol. Lett.* **2006**, 18, 2096–2098.

138. www.genalyte.com

139. H.Y. Zhu HY et al., *Opt. Express* **2007**, 15, 9139–46.

140. P. Zijlstra, K.L. van der Molen, A.P. Mosk, *Appl. Phys. Lett.* **2007**, *90*, 161101/1-3.

141. E. Nuhiji, P. Mulvaney, *Small* **2007**, 3(8), 1408 – 1414.

142. M. Schubert et al., Nano Lett. 2015, 15(8), 5647-5652.

143. G. Decher, J. Hong, *Makromol. Chem. Macromol. Symp.* **1991**, 46.

144. G. Decher, J. Hong, *Berich. Bunsen. Gesell.* **1991**, 95.

145. G. Decher, J. Hong, J. Schmitt, *Thin Solid Films* **1992**, 210-211.

146. G. Decher, *Science* **1997**, 277.

147. Y. Liu, Y. Wang, R. O. Claus, *Chem. Phys. Lett.* **1998**, 298.

148. Y. Lvov, K. Ariga, I. Ichinose, T. Kunitake, *J. Am. Chem. Soc.* **1995**, 117.

149. G. B. Sukhorukov, H. Möhwald, G. Decher, Y. M. Lvov, *Thin Solid Films* **1996**, 285.

150. R. Georgieva, S. Moya, S. Leporatti, B. Neu, H. Bäumler, C. Reichle, E. Donath, H. Möhwald, *Langmuir* **2000**, 16.

151. Y. Lvov, H. Haas, G. Decher, H. Möhwald, A. Mikhailov, B. Mtchedlishvily, E. Morgunova, B. Vainshtein, *Langmuir* **1994**, 10.

152. A. A. Mamedov, N. A. Kotov, M. Prato, D. M. Guldi, J. P. Wicksted, A. Hirsch, Nat. Mater. 2002, 1.

153. O. Guillame-Gentil et al., *Adv. Mater.* **2010**, 22.

154. R. K. Iler, *J. Colloid Interface Sci.* **1971**, 21, 569-594.

155. S. W. Keller, S.A. Brigham, E.S. Johnson, E.H. Yonemoto, T.E. Mallouk, *J. Am. Chem. Soc.* **1995**, 117.

156. C. S. Peyratout, L. Dähne, *Angew. Chem., Int. Ed.* **2004**, 43.

157. P. T. Hammond, *Materials Today* **2012**, 15.

158. G. Malucelli, *Coatings* **2016**, 6, 33.

159. Z. Zheng, J. McDonald, R. Khillan, Y. Su, T. Shutava, G. Grozdits, Y.M. Lvov, *J. Nanosci. Nanotechnol.* **2006**, 6.

160. H. Arnona, R. Granita, R. Porata, E. Poverenova, *Food Chem. 2016*, 166.

161. H. Lee, R. Mensire, R.E. Cohen, M.F. Rubner, *Macromolecules* **2012**, 45, 1.

162. M. Elzbieciak-Wodka, M. Kolasinska-Sojka, P. Nowak, P. Warszynski, *J. Electroanalyt. Chem.* **2015**, 738.

163. N.A. Kotov, *Nanostructured Mater.* **1999**, 12, 5-8.

164. Q. An, T. Huang, F. Shi, *Chem. Soc. Rev.* **2018**, 13.

165. Z. Feldötö, I. Varga, E. Bloomberg, *Langmuir* **2010**, 26, 17048.

166. J. Kang, M. Loew, A. Arbuzova, I. Andreou, L. Dähne, *Adv. Mater.* **2010**, 22, 3548.

167. H. Huang, E. Ruckenstein, *Langmuir* **2006**, 22, 10.

168. G. Decher, J. B. Schlenoff, *Multilayer Thin Films* Wiley-VCH Verlag, Weinheim **2012.**

169. W. Knoll, R. C. Advincula, *Functional Polymer Films* Wiley-VCH Verlag, Weinheim **2011**.

170. S. Borhani, S. Hassanajili, S. Tafti, S. Rabbani, *Prog. in Biomater.* **2018**, 7, 3.

171. A. W. Martinez, E. L. Chaikof, *Wiley Interdiscip Rev Nanomed Nanobiotechnol.* **2011**, 3, 3.

172. D. Silva, H.C. Sousa, M.H. Gil, L.F. Santos, G.M. Moutinho, A.P. Serro, B. Saramago, *Int J Pharm.* **2018**, 553, 1-2.

173. X. H. Hu, H. P. Tan, D. Li & M. Y. Gu, *Mat. Tech.* **2014**, 29, 1.

174. Y. Lvov, A. A. Antipov, A. Mamedov, H. Mohwald, G.B. Sukhorukov, *Nano Lett.* **2001**, 1, 3.

175. G.F. Schneider, V. Subr, K. Ulbrich, G. Decher, *Nano Lett.* **2009**, 9, 2.

176. C.R. Wittmer, J.A. Phelps, W.M. Saltzman, P.R. Van Tassel, *Biomater.* **2006**, 28, 5.

177. J. Zhan, L. Wang, S. Liu, J. Chen, L. Ren, and Y. Wang, *ACS Appl. Mater. Interfaces* **2015**, 7, 13876–13881.

178. K. J. Loh, J. Kim, J. P. Lynch, N. Wong Shi Kam, N. A. Kotov, *Smart Mater. Struct.* **2007**, 16, 429–438.

179. K. J. Loh , J. P. Lynch, N. A. Kotov, *Inter. J. App. Electromag. And Mech.* **2008**, 28, 1-2.

180. A. Riul, R.R. Malmegrim, F.J. Fonseca, L.H.C. Mattoso, *Biosens. and Bioelectron.* **2003,** 18, 1365-1369.

181. A. Riul, A.M. Gallardo Soto, S.V. Mello, S. Bone, D. M. Taylor, L. H. C. Mattoso, *Synthetic Metals* **2003**, 132, 2.

182. C. E. Borato, A. Riul, M. Ferreira , O. N. Oliveira, L. H. C. Mattoso, *Instrum.Scie. And Tech.* **2004**, 32, 1.

183. P.W: Atkins, Physical Chemistry Oxford University Press, **2002**.

184. J.R. Lakowicz, *Principles of fluorescence spectroscopy*, 3rd ed., Springer, New York, **2006.**

185. www.zeiss.com

186. www.cpsinstruments.com

187. I. Reviakine, D. Johannsmann, R. P. Richter, *Anal. Chem.* **2011**, 83, 8838.

188. www.thermofisher.com

189. www.microparticles.com

190. M. Olszyna, A. Debrassi, C. Üzüm, L. Dähne, *Adv. Func. Mater.* **2018**, 29.

191. Y. Wu, Y. Li, L. Qin, F. Yang, D. Wu, *J. Mater. Chem. B* **2013**, 1, 204.

192. D. Holmes, *Inquiry J.* **2005**, 4.

193. N.K. Varde, D.W. Pack, *Expert Opin. Biol. Ther.* **2004**, 4, 35-51.

194. C.S. Chern, *Prog. Polym. Sci.* **2006**, 31.

195. J-W. Kim, K-D. Suh, *Polym.* **2000**, 41.

196. Q. Zhang, Y. Han, W-C. Wang, L. Zhang, J. Chang, *Europ. Polym. J* **2009**, 45, 2.

197. R. A. Ghostine, R. M. Jisr, A. Lehaf, J. B. Schlenoff, *Langmuir* **2013**, 29, 11742.

198. S. Dodoo, B. N. Balzer, T. Hugel, A. Laschewsky, R. Klitzing, *Soft Mater.* **2013**, 11, 157.

199. S. T. Dubas, J. B. Schlenoff, *Macromolecules* **2001**, 34, 3736.

200. J. Kang, L. Dähne, *Langmuir* **2011**, 27, 4627.

201. T. Mauser, C. Dejugnat, H. Möhwald, G. B. Sukhorukov, *Langmuir* **2006**, 22, 5888.

202. A.N. Baschkatov, E. A. Genina, *Opti. Techn Biophys and Med.* **2003**, 5068.

203. S. Liu et al. *Sensors* **2019**, 19, 4063.

204. D. K. Roper, *Chem. Eng. Sci.* **2007**, 62(7).

205. H. L. Tan, M. J. McMurdo, G. Pan, G. Van Patten, Langmuir 2003, 19, 9311-9314.

206. J. J. Iturri-Ramos, S. Stahl, R. P. Richter, S. E. Moya, *Macromolecules* **2010**, 43.

207. J. Schmitt, T. Gruenewald, G. Decher, P. S. Pershan, K. Kjaer, M. Loesche, *Macromolecules* **1993**, 26.

208. J. J. Harris, M. L. Bruening, *Langmuir* **2000**, 16.

209. N. Granqvist, H. Liang, T. Laurila, J. Sadowski, M. Yliperttula, T. Viitala, *Langmuir* **2013**, 29.

210. I. Choi, R. Suntivich, F. A. Plamper, C. V. Synatschke, A. H. E. Muller, V. V. Tsukruk, *J. Am. Chem. Soc.* **2011**, 133.

211. C. Picart, P. Lavalle, P. Hubert, F. J. G. Guisinier, G. Decher, P. Schaaf, J-C Voegel, *Langmuir* **2001**, 17.

212. G. Ladam, P. Schaad, J. C. Vögel, P. Schaff, G. Decher, F. Cuisinier, *Langmuir* **2000**, *16*, 1249-1255.

213. J. F. Quinn, A. P. R. Johnston, G. K. Such, A. N. Zelikina, F. Caruso, *Chem. Soc. Rev.* **2007**, 36, 707-718.

214. S. Sukhishvili, S. Granick, *Macromolecules* **2002,** 35*, 301-310.

215. L. F. Hoyt, *Oil and Soap* **1933**, 10(43).

216. H. Paulsen, D. Stoye, in *"The chemistry of amides,"* (Ed. J. Zabicky), Wiley & Sons **1970**, Ch. 10.

217. J. Choi, M. F. Rubner, *Macromolecules* **2005**, 38, 1.

218. X.Wang, X. Ye, G. Zhangb, Soft Matter. **2015**, 11, 538.

219. C. Picart, J. Mutterer, L. Richert, Y. Luo, G.D. Prestwich, P. Schaaf, J.C. Voegel, P. Lavalle, *Proc. Natl. Acad. Sci. USA.* **2002**, 99, 20.

220. IUPAC, *Compendium of Chemical Terminology*, 2nd ed. **1997**, (the "Gold Book"), Online corrected version: (2006–).

221. D. L. Purich, R. D. Allison, *"Handbook of Biochemical Kinetics,"* Academic Press **2000.**

222. J. L. Arlett, E. B. Myers, M.L. Roukes, *Nature Nanotech.* **2011**, 6.

223. S. Rau, G. Gauglitz, *Anal. Bioanal. Chem.* **2012**, 402, 529–536.

224. A. R. Ali, C. M. Elias, *Chemosens.* **2017**, 5, 19.

225. Hansch, C., Leo, A., D. Hoekman*, DC: American Chemical Society,* **1995**, 9.

Curriculum vitae

Mateusz Olszyna was born in Kalisz, Poland on 30th October 1986. After finishing the financial accounting at the Technical College of Economy in Kalisz in 2006, he started his study in Biotechnology at the University of Life Science in Poznan, Poland. In 2009 he completed his student internship at Max Planck Institute in Berlin, Germany, characterized the role of gene NOA1 in mouse development. In 2010 he started his master studies in medical and industrial biotechnology at the same university under the supervision of Dr. Anna Olejnik and Prof. Wlodzimierz Grajek. There he determined the antibacterial and anticancer properties of potato juice using the cancer cell lines. In 2011 he completed his internship at Dermatology Cancer Clinic of the University of Tuebingen, Germany under the supervision of Prof. Birgit Schittek and Prof. Claus Garbe. There he analyzed the expression of factors involved in PI3K – signaling pathway in melanoma cancer cells. In 2012 he joined the company Surflay Nanotech GmbH in Berlin, Germany to work on project LbL-brane applying the LbL-technology in the fabrication of regenerable nanofiltration membranes. In 2013 he started his PhD work under the project BactoSens and Immunoplex aimed at the development of novel fluorescent, label-free biosensors based on the Whispering Gallery Modes phenomenon. The most important findings in this research are described in this thesis.

List of publications

D. Nikoniuk, K. Bednarska, M. Sienkiewicz, G. Krzesinski, M. Olszyna, L. Dähne, T.R. Wolinski, P. Lesiak, Polymer fibers covered by soft multilayer films for sensing applications in composite materials, **2019**, Sensors, *19*(18), 4052.

M. Olszyna, A. Debrassi, C. Üzüm, L. Dähne, *Label-free bioanalysis based on Low-Q Whispering Gallery Modes: Rapid preparation of microsensors by means of Layer-by-Layer technology*, Adv. Func. Mater. **2018**, 29.

D. Gregurec, M. Olszyna, N. Politakos, L. Yate, L. Dähne, S. E. Moya, *Stability of polyelectrolyte multilayers in oxidizing media: a critical issue for the development of multilayer based membranes for nanofiltration*, Colloid Polym. Sci. **2015**, 293, 381-388.

R. Bischler, M. Olszyna, M. Himmelhaus, L. Dähne, *Development of a fully automated in-vitro diagnostics system based on Low-Q Whispering Gallery Modes in fluorescent microparticles*, Eur. Phys. J. Spec. Top. **2014**, 223, 2041–2055.

Participations in scientific conferences and poster sessions

Lab-on-a-chip and Microfluidics Europe Conference and Exhibition 2019, Rotterdam, M. Olszyna, L. Dähne.

Workshop of 3. Call for cooperation projects between Poland and Berlin-Brandenburg, Berlin 2017. *Whispering Gallery Mode excitation in fluorescent microbeads as a platform for label-free biosensing.* M. Olszyna, C. Üzüm, M. Himmelhaus, L. Dähne.

Nanotech Poland, Poznan 2016. *Whispering Gallery Mode excitation in fluorescent microbeads as a platform for label-free biosensing,* M. Olszyna, C. Üzüm, G. Dähne, M. Himmelhaus, L. Dähne.

Potsdam Days on Bioanalysis, Potsdam 2015, *Development of a Fully Automated In-Vitro Diagnostic System Based on Low-Q Whispering Gallery Modes,* S. Müller, M. Himmelhaus, M. Olszyna, L. Dähne.

Taking Detection to the Limit: Biosensing with Optical Microcavities, WE-Heraeus-Seminar, Bad Honnef, 2014. *Label-free diagnostic tool based on Whispering Gallery Modes*, M. Olszyna, R. Bischler, M. Himmelhaus, L. Dähne.

TH-BIO-Connect Symposium, Wildau, 2014. *Label-free diagnostic tool based on Whispering Gallery Modes*, M. Olszyna, R. Bischler, M. Himmelhaus, L. Dähne.

Potsdam Days on Bioanalysis, Potsdam, 2013. *Label-free diagnostic tool based on Whispering Gallery Modes.* M. Olszyna, R. Bischler, M. Himmelhaus, L. Dähne.

Nano and Advanced Materials Workshop and Fair. Warsaw, 2013. *Label-free diagnostic tool based on Whispering Gallery Modes.* M. Olszyna, R. Bischler, M. Himmelhaus, L. Dähne.